Growth and characterization of ZnO nanoparticles by sol-gel process

A Thesis Submitted in Fulfillment of the
Requirements for the Degree of

MAGISTER SCIENTIAE (M.Sc.)

By Jatani Ungula

(B.Sc Hons)

Student Number: 2012033243

Supervisor: Prof. F.B Dejene

Department of Physics, University of the Free State

(QwaQwa campus), South Africa, ZA 9866

January 2015

Dedication

This thesis is dedicated to my lovely family and my dear parents.

Acknowledgements

- Praise is to God forever for His everlasting love and compassion and for granting me the strength and passion to pursue this course for the service of mankind and glory of His name.

- My most gratitude goes to my supervisor **Prof. F.B Dejene** who accepted me as a student in his research fellowship and continuously guided and mentored me during the course of my research. I recall his constructive criticisms, valuable comments and suggestions which were indispensable for the completion of my project. I, also, do acknowledge the encouragements and administrative support of **Prof Henrik Swart** (chair research- UFS).

- I also wish to convey my sincere thanks to **Dr. L.F Koao, Mr A.H Wako** for their support, patience and encouragement during my research work. My thanks to my lecturers and Qwa Qwa Physics teaching fraternity **Mr K.G Tshabalala, Mr. R.O Ocaya, S.V Motloung** and the late **Dr J.J Dolo** for their constant advice on various academic matters relevant to my thesis.

- I am grateful to **Mr. A.G Ali** and **S.J Motloung** for their enormous support and help in various aspects. I am thankful to all my research colleagues **Mr T.D Malevu, Mr V Molefe, Mr.T Lotha, Ms A. Seitathi, Mr T.Sithole, Ms K. Foka, Ms M.A Lephoto, Ms L. Meiki** and **Ms S. Kiprotich** at the UFS QwaQwa Laboratory for their continuous help and comments during my research. My appreciation **to Ms M.A, Ms Mofokeng** and **Ms De Clerk** of Qwa Qwa Chemistry Department for allowing me to use their SEM, FTIR and DTA/DSC systems.

- It is my pleasure to remember members of the UFS Bloemfontein Laboratory and staff. **Mr. R. Nyenje , Mr Sammy, Ms M. Duvenhage, Mr. Cronje Shaun, Ms Tshabalala, Ms Mbule, Ms Mokoena** and most importantly **Dr Ted Kroon** for their support and the help rendered in acquiring PL, SEM, UV-Vis and XRD measurements.

- I gratefully acknowledge the financial support for my project from South African National Research Foundation (NRF) and the University of the Free State.

- Finally, I would like to express my indebtedness to my family-beloved PuritySharon, parents, brothers and sisters for their encouragement and moral support.

Abstract

Solid state lighting technology is of particular interest in application of semiconductors. To this end, ZnO nanostructures have gained great attention in the research community, in part because of its requisite large direct band gap. The stability of the exciton (binding energy 60 meV) in this material, can lead to lasing action based on exciton recombination and possibly exciton interaction, even above room temperature. Therefore, it is very important to realize an optimized growth of ZnO nanostructures and investigate their properties. The main motivation for this thesis is not only to successfully realize the controllable growth of ZnO nanoparticles by sol-gel method, but also to investigate the structure, optical and electrical properties in detail by means of scanning electron microscopy (SEM), photoluminescence (PL) spectroscopy), UV-Vis spectroscopy, X-ray diffraction (XRD) and other techniques.

The influence of various growth parameters on the morphology, optical and electrical properties of the nanoparticles were also systematically studied. These include the growth temperature, volume ratios of water to ethanol solvent and different dopants effects. By controlling these parameters different shapes of nanoparticles, like spherical particles, nanorods and nanoflowers are demonstrated.

XRD indicated that all the as-grown and annealed nanoparticles produced at temperatures between room temperature and 75 °C crystallize in the wurtzite structure and post growth annealing enhanced the crystalline quality of the materials while the band gap energy reduces. The crystallite size, obtained from XRD analysis, of as prepared ZnO nanostructures was found to decrease from 24 to 12 nm with the increase in volume ratio of ethanol in the solvent as peak intensities and sharpness increase with volume ratio of water. Thus in order to have smaller particles more volume ratios of ethanol solvent is favourable at growth temperature of 35 °C. The dopants were also observed to have slight effect on the grain sizes .No traces of zinc hydroxide were observed even in materials grown at lower temperature as reported by some authors.

The optical quality of the nanostructures was investigated using PL. Both UV and defect related emissions have been observed for all as-grown and annealed samples of nanostructures. Photoluminescence spectra showed a strong ultra-violet emission, for annealed ZnO nanoparticles, which was centred on 385 nm and weak green emission at 550 nm confirming that the samples possess good optical properties with less structural defects and impurities. The effect of post-growth annealing on the optical quality of the nanostructures was carefully examined. Annealing at a temperature of 600 °C enhances the UV emission and suppresses defect related deep level emission for all samples. The PL spectra showed strong, broad and intense emission in visible region for Ce-doped ZnO samples while other dopants suppressed this green emission.

The reflectance spectra of the annealed products show that the percentage absorption in visible range increases with annealing temperature. UV measurements depict a shift in absorption edge confirming the changes in particle sizes with varying ratios of solvents (water and ethanol). The band gap decreased from 3.31 to 3.17 eV with an increase in the ethanol composition in the solvent, implying that the optical properties of these materials are clearly affected by the precursor compositions.

The SEM micrograph of ZnO revealed that the surface aspect depends on both the dopant used and annealing temperature. The characterization of the nanoparticles with Scanning Electron Microscopy (SEM) showed that at low temperatures (35 °C and 45ºC) clearly defined spherical particles are formed while at higher temperatures agglomerated irregular and diminished nanoparticles were observed.

Key words

ZnO, ethanol, water, nanoparticles, semiconductors, controllable growth, optical properties, post annealing.

Acronyms

- **1D** - One dimensional
- **CBD** - Chemical bath deposition
- **CBM** - Conduction band minimum
- **DI water** - De-ionized water
- **DLE** - Deep level emission
- **EDS** - Energy dispersive x-ray spectroscopy
- **EL** – Electroluminescence
- **FWHM** - Full width at half maximum Electroluminescence
- **HCP** - Hexagonal close packed
- **NBE** - Near band edge emission
- **PL** – Photoluminescence
- **UV** – Ultraviolet
- **VBM** - Valance band maximum
- **XRD** - X-ray diffraction
- **ZnO** - Zinc oxide
- **EtOH**-Ethanol

Table of Contents

Chapter 1

Introduction

1.1. Motivation and Background

Development of new solid state materials has taken centre stage in recent discoveries in Physics and engineering globally. The discovery of semiconducting materials has revolutionized the safety and lifestyle of mankind. Semiconductors are widely used in communication, military, medicine, security, and entertainment industries. Semiconducting nanomaterials are receiving much attention owing to their novel optical, electronic and magnetic properties for applications in the field of solar cells (photovoltaic cells), optical planer wave guides, electronics, catalysis, optical communication, energy storage, sensing, data storage, transmission, environmental protection, cosmetics, and Light emitting devices (LEDs). Flat display technologies include LCD, PDP, FED, Projection TV, LED, and OLED microelectronics.

Semiconducting nanoparticles lend us the opportunity to understand the physical properties in low dimensions and to explore their vast possible applications; their diversity and flexibility open possibilities for fabrication of more powerful, faster and smaller semiconducting devices while at the same time increasing manufacturing volumes at lower cost.

Nanostructure materials are a single phase or multiple polycrystalline solids with a typical average size of a few nanometers (1 nm $=10^{-9}$m). Basically the range from (1-100) nm is taken as nano-range for convention as per National Nanotechnology Initiative in the US. The size of hydrogen is considered as the lower limit of nano whereas the upper limit is arbitrary. The size range that holds so much interest in nanomaterials is typically from 100 nm to the atomic level (0.2 nm). As the particle size decreases to some extent, a large number of constituting atoms can be found around the surface of the particles, which makes the particles highly reactive with prominent physical properties, hence, manipulation and control of the material properties via mechanistic means is needed. Small nanoparticles allow the study of relevant surface properties due to the high surface to bulk ratio; as a result of small particle size the materials have very large surface area to volume ratio (Figure 1.1), bringing out new and enhanced physical and chemical properties which are different with large scale counterpart.

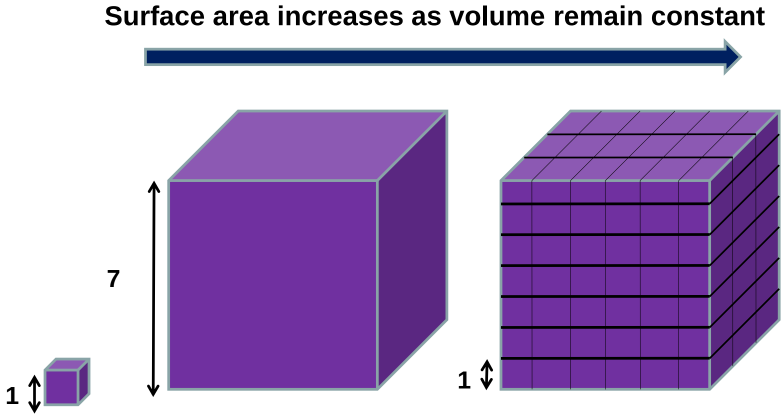

Figure 1.1 Surface area-to-volume ratio.

An increase on the relative surface area and dominance of quantum confinement effects of charge carriers (electrons and holes) in the restricted volume of nanoparticles are the two main reasons for this change in behavior. By decreasing the particle size of the band structure of semiconductor, the band gap increases and the edges of the bands split into discrete energy levels. This process is called quantum confinement regime [1]. Nanostructure material is thus characterized by a large number of interfaces in which the atomic arrangements are different from those of crystal lattice [2- 6]**.** The basic classification of nanomaterial is done based on the confinement. Bulk structures show no confinement whereas nanowells and nanowires can be obtained by 2-D and 1-D confinement respectively. The quantum realm comes to the picture when there is a 3-D confinement and leads to zero dimension quantum structures that is quantum dot. One-dimensional (1D) nanostructures represent a group of nanomaterial with highly anisotropic morphologies.

The invention of the germanium (Ge) based point-contract transistor by Bardeen and Brattain [7] in 1947 and its further modification by William Shockley [8] was a major breakthrough. Despite the first transistor being manufactured from Ge its lower melting point and poor oxide properties have imposed major limitations for its application for device fabrication. As a result, silicon (Si) has become the dominant material in the global semiconductor industry and has been used in various fields such as communications, data storage and integrated circuits for computing devices [9]. However, Si also has its own limitations. It is a relatively narrow (1.12 eV) and indirect band gap material. Materials with indirect band gaps generate phonons (or heat) during optical emission. Thus Si-based materials are unsuitable for optoelectronic devices, where a direct band gap is needed for efficient optical emission. In addition, its smaller band gap hinders its use in applications requiring higher operating temperatures. These limitations have led to the invention of a second generation of semiconductors, namely the III-V compounds. These materials are more suitable than Si for high-speed devices and optoelectronic applications such as light emitting diodes (LED) and laser diodes. Among these semiconductor materials, gallium arsenide (GaAs), a direct band gap semiconductor with superior electronic transport properties and many other suitable optical properties, is the most studied [10]. GaAs has a higher carrier mobility and effective carrier velocity than Si, which translates into faster devices [11]. These properties make GaAs (and related materials such as InGaAs and AlGaAs) very suitable for high speed integrated circuits and optoelectronic applications. For example, III-V nitride-based LEDs with high quantum efficiency (35% for InGaN-based LEDs [12]) compared to 2 % for Si LEDs [13], and stable *p*-type III-V nitride compounds with low resistivity [14] have been produced. As a result these materials dominate Si in LED applications. However, the physical properties required for high power, high temperature electronics and UV/blue light emitter applications are beyond the limits of Si or traditional III-VI semiconductors. These limitations enforced the birth of a third generation of semiconductors, the wide band gap II-VI compounds, with direct, larger band gaps that can withstand higher breakdown field strengths. These unique properties, which are absent in most III-V semiconductors, have shifted the interest of many researchers to wide band gap materials.

Among the II-VI materials, zinc oxide nanostructures have gained substantial interest in the research community because ZnO has several advantages over its competitors. It has a direct wide band gap of 3.37 eV at room temperature and an excitonic binding energy of 60 meV [15] (compared to 28 meV for GaN [16]) and room temperature thermal excited energy (25 mev). It also has high electron mobility with undoped state, high thermal conductivity, and good transparency. Its high band gap ensures a large breakdown field, and the thermal stability of the material allows high temperature operation. Thus ZnO is an ideal compound for high power and high temperature electronic devices, and blue/ultraviolet (UV) LED applications so leads to a lasing action based on exciton recombination and possibly exciton interaction even above the room temperature [17, 18]. ZnO is an inorganic and an n-type semiconductor with unique properties and as such, it can absorb infra-red light and infrared electromagnetic wave. Interest in ZnO also derives from its use as a transparent conductive oxide, diverse nanostructure architectures, strong piezoelectricity, stable physical and chemical properties and its biocompatibility [19-21].

ZnO has availability/possibility of soft chemical synthesis besides tremendous application potential, it is inexpensive, relatively abundant, chemically stable, easy to prepare and non-toxic. Due to the availability of cheap and versatile routes of fabrication of zinc oxide nanostructures, it may be treated as cheap replacement of silicon and gallium nitride based costly devices. Recently, ZnO nanoparticles have been explored as alternative to TiO_2 as an electron conductor. Bulk ZnO has unique combination of electrical and optical properties, including relatively high electron mobility (more than 1 order of magnitude larger than anatase TiO_2) [22, 23]. In addition ZnO has richest family of nanostructures [24-27] with diverse applications in optoelectonics and photovoltaics. Nowadays, ZnO is emerging as an efficient electron transport material in technologies, such as DSSCs and inverted polymer solar cells, [28], and [29], QDSSCs, [30] biomedical applications, [31] and light emitting diodes. [32-34] .

Different kinds of ZnO nanostructures in many crystal morphologies are of great significance in the development of novel materials for their use in nanoscale electronics, optoelectronics, in sensing and several other applications. Based on these remarkable physical properties and the motivation of applications of device miniaturization, large effort has been focused on the synthesis, characterization and device applications of ZnO nanomaterials.

Due to the advanced technological applications, high quality of zinc oxide nanostructures are greatly demanded, which induces worldwide research and development on the synthesis and application of zinc oxide nanostructures. The synthesis of nanomaterial can be well accomplished by two approaches. Firstly, by ‘Bottom up’ method where small building blocks are produced and assembled into larger structures. Where the main controlling parameters are morphology, crystallinity, particle size, and chemical composition. Secondly, by ‘Top Down’ method where large objects are modified to give small features. The main reason of alteration in different mechanical, thermal and other property is due to increase in surface to volume ratio. An assortment of ZnO nanostructures such as nanowires, nanotubes, nanorings, and nanotetrapods have been successfully grown via liquid (chemical method), solid and gaseous media [35-47]**.** They include; chemical vapor deposition, thermal evaporation, and electrodeposition, etc. [48-57] sol-gel [58], co-precipitation [59], hydrothermal [60] electrodeposition [61], and chemical bath deposition [62]**.** In comparison, an aqueous solution-based method like chemical bath deposition (CBD), hydrothermal growth and sol-gel methods, is simple, requires no catalyst and is economical.

This research involves investigation and analysis of a process and various properties of ZnO nanostructures by using simple sol-gel process. The sol-gel process allows materials to be made at low temperature. At this temperature, biological and organic impurities can be incorporated into materials for various applications. Dopants, which normally come in the form of inorganic salts and organic materials, can be incorporated easily as solutions. Semiconductors made by the sol-gel method have the potential to hold higher dopant concentrations than melt or thin film forms, which are critical if they were to be used as materials for laser applications and it produces higher quality phosphors.

Several growth parameters that have influence on morphology, optical and electrical properties of nanostructures can be controlled to demonstrate diverse nanostructure architectures. Depending on experimental conditions different designs of ZnO nanostructures such as particles, wires, rods, spiral, helical, flower, tetrapod etc. are observed in both physical as well as chemical routes. These growth conditions/parameters include:- the pH of growth solution, concentrations of reactants, growth temperature and time, different hydroxide precursors, addition of surface passivating agents to the growth solution and doping and co-doping the precursors.

The main motivation of this research is that; the influence of various growth parameters on the synthesis of ZnO nanostructures is used to achieve control over their nanoparicles size and size distribution which is essential for tailoring their electrical, chemical, optical and magnetic properties for desired applications of the nanomaterials devices. The target is to achieve an enhanced physical and optical properties and utilize the possibility and flexibility of controlling various growth conditions and parameters for fabrication of more efficient, faster, smaller and yet cheaper semiconducting devices while at the same time seeking ways of increasing manufacturing volumes at low cost. The properties are investigated using various characterization techniques.

1.2. Statement of the Problem

ZnO semiconductor nanostructures are attractive components to be used for nanometric scale electronic and photonic device applications because of their unique chemical and physical properties. However, there are still significant challenges that have to be overcome in order to produce efficient ZnO devices. The first challenge is in understanding the residual n-type conductivity in unintentionally doped ZnO. Another main obstacle for the commercialization of ZnO based homojunction devices is the absence of stable and reproducible p-type doping with high hole concentrations and large carrier mobility. As a consequence, p-doping of ZnO is still an unsolved problem. It is widely acknowledged that the morphology of ZnO nanostructures is highly sensitive to the growth environment (i.e. temperature, pressure, substrates, precursors and their concentrations, the VI/II ratio or pH, etc). This sensitivity makes it very difficult to control the growth process for the reproducible formation of a desired morphology over large areas. The understanding of native defects in ZnO is still far from complete and has been largely driven by first principal calculations using different approaches. Therefore, controlling native defects and possible compensation processes remain another challenge. Again, some of the basic properties of ZnO are not well understood [63,64] *and* are still debatable owing to the different intrinsic defects such as oxygen interstitials (O_i), zinc interstials (Zn_i), oxygen vacancies (V_o), zinc vacancies (V_{zn}). The origin of white light emission in ZnO is not clear. So, an attempt was made to produce white light from ZnO and to correlate its emission with its intrinsic defects. Kohan et al. [65] reported that more V_o are observed with an excess Zn in ZnO during the growth process. This indicates that the defects in ZnO are depending on the growth techniques and that the coexistence of electrical conductivity and optical transparency in ZnO materials depends on the nature, number and atomic arrangements of metal cations in crystalline or amorphous ZnO structures, on the resident morphology and on the presence of intrinsic or intentionally introduced defects

Therefore, the major problem this thesis seeks to address is how to explore and control the growth process of ZnO nanoparticles for the reproducible formation of a desired morphology amid highly sensitive growth environment and how to control native defects and advance possible compensation process. With the view, to achieving control over the ZnO nanoparticle size and size distribution, this is essential for tailoring optical, electrical, chemical, and magnetic properties of nanoparticles for specific applications.

1.3. Objectives of the Study

The objectives of this study are:-

1. To synthesize ZnO nanoparticles by sol-gel method.
2. To optimize growth conditions for ZnO nanostructures prepared using Sol-gel method.
3. Determining the morphology of the samples with Scanning Electron Microscopy (SEM).
4. To determine the chemical composition of the samples by Energy Dispersive X-Ray spectroscopy (EDS).
5. Determining the crystal structure and particle size with X-Ray Diffraction (XRD).
6. Measuring the absorption and emission intensity of the samples and determining the band gap and particle sizes from the spectral data.
7. To find out the effects of various growth parameters like temperature, solvent, and dopants on the morphological, structural, optical properties and PL intensity of the ZnO nanoparticles.
8. To study the effect of post growth treatment on the structural, optical and electrical quality using SEM, EDS, XRD, PL, UV-Vis, FTIR, DTA/DSC and other characterization techniques.

1.4. Thesis Layout

The thesis consists of eight chapters.

The ***1st Chapter*** begins with the overview of research background, aims of study and statement of problem.

Chapter 2 provides literature review; the introduction of the ZnO and the underlying theories and fundamental properties of ZnO. The different applications of ZnO are also briefly discussed in this chapter.

Chapter 3 gives a brief description of the experimental equipment, environmental and/or atmospheric requirements, techniques used to design, synthesize and characterize ZnO. The sol-gel method used to synthesize the nanoparticles is discussed in detail. A summary of the different characterization techniques are also given. This includes a description of the operation of each of the techniques such as SEM, EDX-S, XRD, FTIR and Uv-Vis.

Chapter 4 reports the study on the effect of growth temperature on structural and luminescence properties of ZnO nanoparticles.

In ***Chapter 5,*** the Comparison of optical and luminescence properties of as prepared and annealed ZnO nanoparticles prepared using sol-gel method is discussed.

In ***chapter 6,*** the effect of solvent medium on the ZnO nanoparticles properties is presented.

Comparison of ZnO nanoparticles properties synthesized at room temperature and 35 ℃ using water and ethanol as solvents is reported.

In ***chapter 7,*** effects of annealing on undoped and Ce, Dy, Eu, Ni-doped ZnO Nanoparticles are also investigated.

Finally, ***chapter 8*** gives summary of the result of this work and suggestions for future work.

References

[1] Chen C.W., K.H. Chen, Chen C.H, Ganguly A, Chen I.C, Wu J.J, Wen H.I, Pong W.F 2006 Appl. *Phys. Lett.* 88 241905-1.

[2] Vogel D, Krüger P , Pollmann 1995 *J Phys. Rev.*, 5214316-1431.

[3] Tammy P. Chou, Qifeng Zhang, Glen E. Fryxell, Guozhong Cao 2007 *Adv. Mater.*,19 2588–2592.

[4] Seema Rani,Poonam Suri, Shishodia P.K, Mehra R.M 2008 921639–1645.

[5] http://www.microscopemaster.com/nanotechnology.html (Accessed on 12th Dec. 2014).

[6] http://www.scientificamerican.com/article.cfm?id=nanotechnologysfuture (Accessed on 12th Dec. 2014).

[7] Jagadish C, Pearton S.J 2006 Zinc Oxide Bulk, Thin Films and Nanostructures: Processing, Properties and Applications. *Austeralia: Elsevier Limited*.

[8] Shockley W 1977 The Path to the Conception of the Junction Transistor - offprint with inscription and sketch *IEEE Electron Devices Society* 597-620.

[9] Pavesi L 2008 "Silicon-Based Light Sources for Silicon Integrated Circuits," *Advances in Optical Technologies,* vol. 2008, pp. 1-12.

[10] Dangbegnon J.K "Photoluminescence study of ZnO doped with nitrogen and arsenic," Nelson Mandela Metropolitan University, PhD thesis 2010.

[11] Shur M. S 1987 GaAs Devices and Circuits (Microdevices). New York: Plenum Press.

[12] Yamada M, Mitani T, Narukawa Y, Shioji S, Niki I, Sonobe S, Deguchi K, Sano M, Mukai T 2002 "InGaN-Based Near-Ultraviolet and Blue-Light-Emitting Diodes with High External Quantum Efficiency Using a Patterned Sapphire Substrate and a Mesh

Electrode," *Jpn. J. Appl. Phys, vol. 41*, pp. L1431-L1433.

[13] Lindros J, Lalic N 1995"High quantum efficiency for a porous silicon light emitting diode under pulsed operation," *Appl. Phys. Lett.,* vol. 66, p. 3048.

[14] Eiting C. J, Grudowski P. A, Dupuis R. D 1997 "Growth of low resistivity p-type GaN by metal organic chemical vapour deposition," *Electronics Letters, vol. 33*, pp. 1987, 1989.

[15] Hummer K 1973 " Interband Magnetoreflection of ZnO," *Phys. Stat. Sol. B, vol. 56*, p.249.

[16] Monema B 1974 "Fundamental energy gap of GaN from photoluminescence excitation spectra," *Phys. Rev. B, vol. 10*, p. 676.

[17] Bagnall D. M, Chen Y. F, Zhu Z, Yao T, Koyama S, Shen M. Y, Goto T 1997 "Optically pumped lasing of ZnO at room temperature," *Appl. Phys. Lett., vol. 70,* p. 2230.

[18] Tang Z.K, Wong G. K. L, P. Kawasaki Yu, M, Ohtomo A, Koinuma H, Segawa Y 1998 "Roomtemperature ultraviolet laser emission from self-assembled ZnO microcrystallite thin films, Appl.Phys.Lett" vol. 72, p. 3270.

[19] Look D.C 2001 "Recent advances in ZnO materials and devices," Mater. Sci. Eng., vol. B80, pp. 383–387.

[20] Teke A, Ozgur U, Dogen S, Gu X, Morkoc H 2004 "Excitonic fine structure and recombination dynamics in single-crystalline ZnO," *Phys. Rev. B, vol. 195207,* pp. 195207-1-10.

[21] Aoki T, Hatanaka Y, Look D.C 2000"ZnO diode fabricated by excimer-laser doping," Appl. Phys. Lett., vol. 76, p. 3257.

[22] Look D. C, Reynolds D. C, Sizelove J. R, Jones R. L, Litton C. W, Cantwell G and

Harsch W. C 1998 *Solid State Commun.* 105, 399.

[23] Forro L, Chauvet O, Emin D, Zuppiroli L, Berger H , Levy F 1994 J. Appl. Phys. 75, 633.

[24] Jin X, Gotz M, Wille S, Mishra Y. K, Adelung R , Zollfrank 2013 C *Adv. Mater*. 25, 1342 .

[25] Klingshirn C 2007 *Chem. Phys. Chem*. 8, 782.

[26] Guerin V.M. , Pauport T 2011 *Energy Environ. Sci.* 4, 2971.

[27] Mishr Y. K, Mohapatra S, Singhal R, Avasthi D. K, Agarwal D. C , Ogale S. B 2008 *Appl. Phys. Lett. 92*, 043107.

[28] Lupan O, Pauporte T , Viana B 2010 Adv. Mater. 22, 3298.

[29] Lupan O, Pauporte T, Bahers T. L, Viana B , Ciofini I 2011 *Adv. Funct. Mater.* 21, 3564

[30] Reynolds D. C, Look D. C, Jogai B, Hoelscher J. E, Sheriff R. E, Harris , M. T *Adv. Mater*. 25, 1344.

[31] Lim J. H, Kong C. K, Kim K. K, Park I. K, Hwang D. K , Park S.2006 *J Adv. Mater.* 18, 2720.

[32] Mohammad M. T, Hashim A. A , Al-Maamory M. H Mater.2006 *Chem. Phys*. 99, 382

[33] Lansdown A. B. G , Taylor A 1997 *Int. J. Cosmet. Sci.* 19, 167.

[34] Kim J. H, Hong Y. C , Uhm H. S 2007 *Surf. Coat. Technol*. 201, 5114.

[35] Tokumoto M. S, Briois V , Santilli C. V 2003 *J. Sol–Gel Sci. Technol*. 26, 547

[36] Zhang J, Sun L. D, Yin J. L, Su H. L, Liao C. S , Yan C. H 2002Chem. Mater. 14, 4172

[37] Demir M. M, Munoz-Espi R, Lieberwirth I , Wegner G 2006 *J. Mater. Chem.* 16, 2940

[38] Tributsch H , Calvin M 1971 *Photochem. Photobiol.* 14, 95.

[39] Lupan O, Guerin V. M, Ghimpu L, Tiginyanu I. M , Pauporte T 2012 *Chem. Phys Lett*. 550, 125.

[40] Ajuria J, Etxebarria I, Cambarau W, Mu~necas U, Tena Zaera R, Jimeno J. C , Pacios R 2011 Energy Environ. Sci. 4, 453.

[41] Kramer I. J , Sargent E. H 2011 ACS Nano 5, 8506.

[42] Mishra Y. K, Adelung R, Rohl C, Shukla D, Spors F , Tiwari V 2011 *Antiviral Res.* 92, 305.

[43] Park S., Lee K. R, Jung C. H, Kim S. J , Shin H. C 1996 *J. Appl. Phys.* 35, 996

[44] Damonte L. C, Zelis L. A. M, Soucase B. M , Fenollosa M. A. H 2004 *Powder Technol.* 148, 15.

[45] Radoi R, Fernandez P, Piqueras J, Wiggins M. S , Solis, J 2003 *Nanotechnology* 14, 794

[46] Zhao X, Zheng , Li C 1998 *Powder Technol.* 100, 20

[47] Lee J. S, Park K, Nahm S, Kang M. IL, Park I. L, Kim S. W, Cho W. K, Han H. S, Kim S 2003 *J. Cryst. Growth* 254, 423.

[48] Fujita S, Kim S.W, Ueda M , Fujita S 2004 *J. Cryst. Growth* 272, 138.

[49] Z hou H , Li Z 2005 *Mater. Chem. Phys.* 89, 326.

[50] Zeng D. W, Xie C. S, Dong M, Jiang R, Chen X, Wang A. H, Wang J. B , Shi J 2004

Appl. Phys. A 79, 1865.

[51] Zhang J, Sun L.D, Jiang X.C, Lian C.S , Yan H C 2004 *Cryst. Growth Des*. 4, 309

[52] Zhang H, Yang D, Ma X, Ji Y, Xu J , Que D 2004 *Nanotechnology* 15, 622

[53] Gao P. X , Wang Z. L 2004 *J. Phys. Chem. B* 108, 7534.

[54] Leung Y. H, Djurišić A. B, Gao J, Xie M. H, Wei Z. F, Xu S. J , Chan W. K 2004 *Chem. Phys. Lett.* 394, 452.

[55] Cao P. J, Zhang H. R, Li J. Q , Gao H. J 2004 *Nanotechnology* 15, 949.

[56] Hu P.A, Liu Y.Q, Fu L, Wang X.B, Zhu D.B 2004 *Appl. Phys. A* 78, 15.

[57] Tian Z. R, Voigt J. A, Liu J, Mckenzie B , Mcdermott M. 2003 *J Nat. Mater.* 2, 821.

[58] Neetu Singh, Mehra R.M, Kapoo A, Soga T 2012 *J. Renewable Sustainable Energy* 4 013110.

[59] Song R, Liu Y , He L *Solid State Sci.* 10 (2008) 1563.

[60] ElenK, Elen K, Vanden H.R, Hardy A, Van Bael M.K, D'Haen J, Peerters R, Franco D , Mullens J 2009 *Nanotechnology* 20 055608.

[61] Moghamad A.B, Nazari T, Badraghi J , Kazemzadeh M 2009 *Int. J. Electrochem.* 4 247

[62] Koao L.F, Dejene F.B, Kroon R.E , Swart H.C 2014 *J. Lumin.* 147 85.

[63] McCluskey M.D , Jokela S.J 2009 *J.Appl. Phys.* 106 071101

[64] Schmide-Mende L , MacManus-Driscoll 2007*J.L Mater. Today* 10 40.

[65] Kohan A.F, Ceder G, Morgan D, Chris G. Van de Walle 2000 *Phys. Rev. B* 61 15019 F.A. Kroger, Elsevier, Amsterdam, 1948.

Chapter 2

Overview of ZnO material properties

2.1. Introduction

ZnO, known since the ancient times, occurs naturally as the mineral zincite and has been the subject of extensive investigation for many years [1]. It has been produced commercially for considerably more than a century. It was originally used as a pigment in paints and also for rubber, glass, ceramic enamels and pharmaceuticals [2]. During the last decade ZnO has once again become a focus of research activities, driven by the prospect of potential applications in optoelectronics, transparent electronics and spintronic.

2.2. Crystal structure and lattice parameters of ZnO.

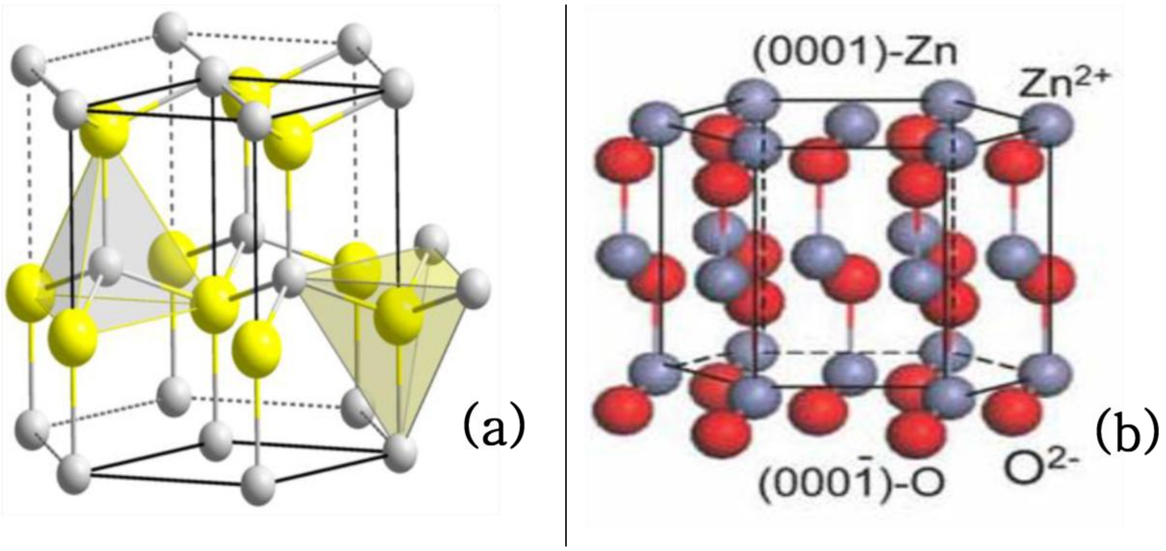

Figure 2.1 Schematic representations of wurtzite ZnO: (a) neighboring atoms showing tetrahedral coordination of Zn-O, where every atom of one kind is surrounded by four atoms of the other kind, and (b) the hexagonal lattice.

A detailed schematic arrangement of atoms in the conventional unit cell is shown in Fig. 2.1(a). This wurtzite lattice is composed of two interpenetrating hexagonal close-packed (hcp) sub-lattices, each of which consists of one type of atom displaced with respect to each other along the threefold c-axis [3-4]. From this figure it is clearly seen that every atom of one kind (e.g. Zn) is surrounded by four atoms of the other kind (O), or vice versa, which are positioned at the edges of a tetrahedron. This tetrahedral coordination is typical of sp^3 covalent bonding. The Zn-O bond length is 1.992 Å in the direction parallel to the c-axis of the hexagonal unit cell and 1.973 Å in the other three directions of the tetrahedral arrangement. In a wurtzite lattice, there are lattice parameters a, b and c, and the internal parameter u and bond angles α and $\beta = 109.47^\circ$. The internal parameter u is defined as the length of the bond parallel to the c-axis (anion–cation bond length or the nearest-neighbour distance) divided by the lattice parameter c. The lattice constants of the ZnO unit cell are a = b =3.2495 Å and c = 5.20628 Å, yielding a c/a ratio of 1.602, which is close to the ideal value of 1.633 expected for the hcp unit cell [5-7]. In addition to intrinsic material properties, the lattice parameters are affected by extrinsic properties such as the free electron concentration (via the deformation potential of the conduction band minimum), the concentration of foreign impurities with different ionic radii which can replace the host atom, substrate-induced strain and temperature [8].

Figure 2.1(b) shows the hexagonal lattice, Because of the difference in electronegativity between Zn and O, it also has a substantial ionic character [9].

In addition to the wurtzite phase, ZnO is also known to crystallize in the cubic zinc blende and rock salt (NaCl) structures, which are illustrated in Figure 2.2 [10].

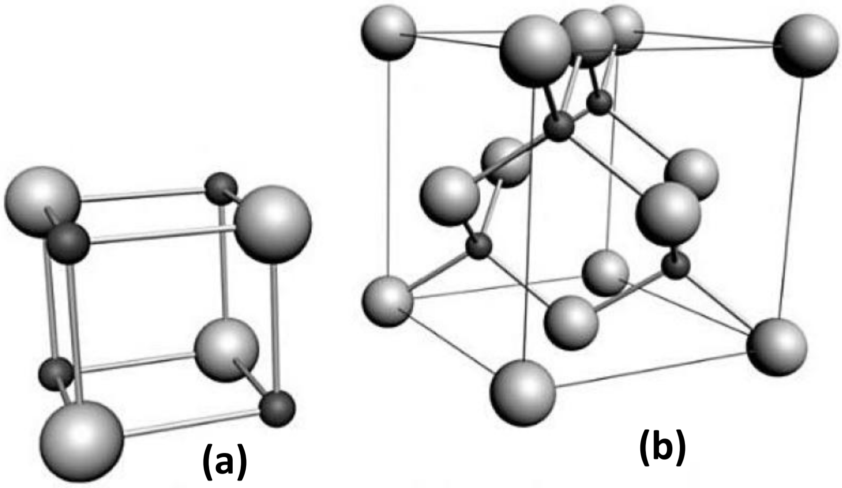

Figure 2.2 (a) The rock salt and (b) zinc blende phases of ZnO.

O atoms are shown as white spheres, Zn atom as black spheres. Only one unit cell is illustrated for clarity [Reprinted with permission from Ref. [10], Copyright 2006 by Elsevier Limited.].

2.2.1 Growth facets of ZnO nanoparticles

As described earlier, the structure of ZnO can be considered as a number of alternating planes composed of tetrahedrally coordinated O^{2-} and Zn^{2+} ions stacked alternately along the c-axis, as shown in Fig. 2.3(a) and (c). This tetrahedral structure gives rise to polar asymmetry along the hexagonal axis. The anisotropy of the ZnO crystal structure assists with the growth of 1D structure. The most common polar surface is the (0001) basal plane. In one dimensional structure (like a nanoparticles) the oppositely charged ions produced result in a normal dipole moment and spontaneous polarization, as well as a divergence in surface energy [11,12] No doubt, this kind of tetrahedral coordination in ZnO will form a noncentral symmetric structure with polar symmetry along the hexagonal axis, which not only directly induces the characteristic piezoelectricity and spontaneous polarization, but also plays a key factor in crystal growth, etching and defect generation of ZnO. The polar faces are known to possess different chemical and physical properties, and the O-terminated face possesses a slightly different electronic structure from the other three faces. Figs. 2.3(b) describe the two polar facets for 1D wurtzite ZnO.

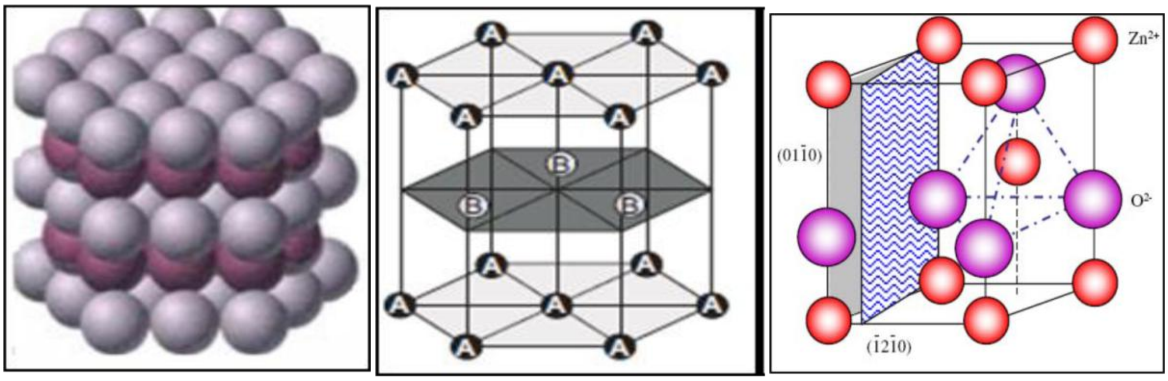

(a) (b) (c)

Figure 2.3 The wurtzite structure model of ZnO (a) The ABAB…stacking sequence of atoms in a hexagonal lattice dictates the morphology of one-dimensional ZnO nanoparticles (b) A and B stacking in the hexagonal close packed (hcp) structure. (c) Tetrahedral co-ordination of Zn-O. [Reprinted with permission from Ref. [13], Copyright 2004 by IOP Publishing Ltd.].

2.3 Electronic band structure

An accurate knowledge about the band structure of a semiconductor is quite critical for exploring its applications and even improving the performance. Considering that ZnO is a candidate semiconductor for optoelectronic device applications, a clear understanding of the band structure is of critical importance in explaining the optical and electrical properties. The most important factor responsible for a material to show a better optoelectronic property is the large exciton binding energy and this property is possessed by Zinc oxide having binding energy of 60mev which could be attended at and above room temperature due to excitonic recombination [14]. The process of optical absorption and emission have been influenced by bound excitons which are extrinsic transition related to dopants or defects thereby usually responsible for creating discrete electronic states in the band gap. Theoretically, neutral or charged donors and acceptors are the members by which exciton could be bound with and it merely depends on the band structure of semiconductor material [15, 16].

To date, several theoretical approaches of varying degrees of complexity, such as Green's functional method Local Density Approximation (LDA) [17, 18], GW approximation (GWA) [19, 20] and First-principles (FP) [21-23], have been employed to calculate the band structure of wurtzite ZnO. Besides, a number of experimental data have also been published regarding the band structure of the electronic states in wurtzite ZnO, [24-28]. For example, D. Vogel et al further improved the LDA method by incorporating atomic self interaction corrected pseudo potentials (SIC-PP), in which Zn 3*d* electrons had been accurately taken into account to calculate the electronic band structure of ZnO. The corresponding results have been shown in figure 2.4.

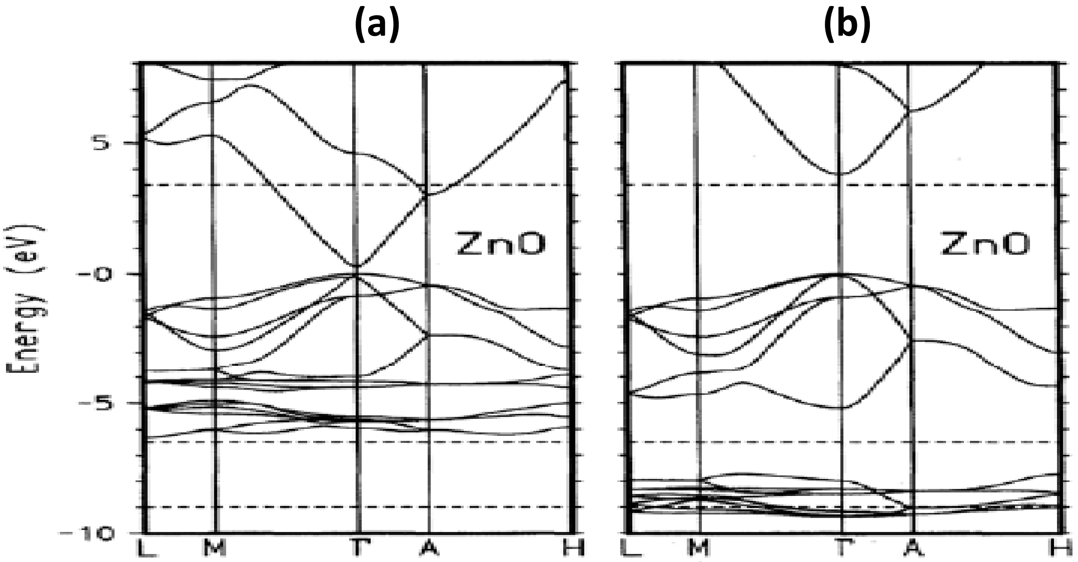

Figure 2.4(a) The LDA band structure of bulk wurtzite ZnO calculated using a standard pseudopotentials (PP) or (b) dominant atomic self-interaction-corrected pseudopotentials (SIC-PP).

The horizontal dashed lines indicate the measured gap energy and d-band width. SIC-PP is much more efficient at treating the d-bands than the standard LDA method. [Reprinted with permission from [29], Copyright 1995 by the American Physical Society].

The band gap as determined from the standard LDA calculations is only ~3 eV, as shown in Figure 2.4(a). This shrunk band gap was obtained because 3d states have been treated as core levels in order to simplify the calculations in the standard LDA method. According to the calculation results from SIC-PP method as shown in Figure 2.4(b), the bottom 10 bands (occurring around -9 eV) correspond to Zn 3*d* levels. The next 6 bands from -5 eV to 0 eV correspond to O 2*p* bonding states. The first two conduction band states are strongly Zn localized and correspond to empty Zn 3*s* levels. In contrast to the left panel, the d-bands are shifted down in energy considerably and concomitantly the gap is opened drastically. In addition, the dispersion and bandwidth of the O 2p valence bands are changed significantly. The gap energy and the d-band position are grossly improved as compared to the standard LDA results. The band gap as determined from this calculation is 3.77 eV, which correlates reasonably well with the experimental value of 3.4 eV. Therefore, we can see that the band gap energy and d-band position have been significantly improved as compared to the standard LDA results.

Since both conduction and valence bands contribute significantly to the energy range where the optical excitations fall in, it is impossible to give a detailed interpretation of optical reflectance without at least a semi quantitative band-structure calculation first. Experimental data have also been published regarding the band structure and electronic states of wurtzite ZnO.

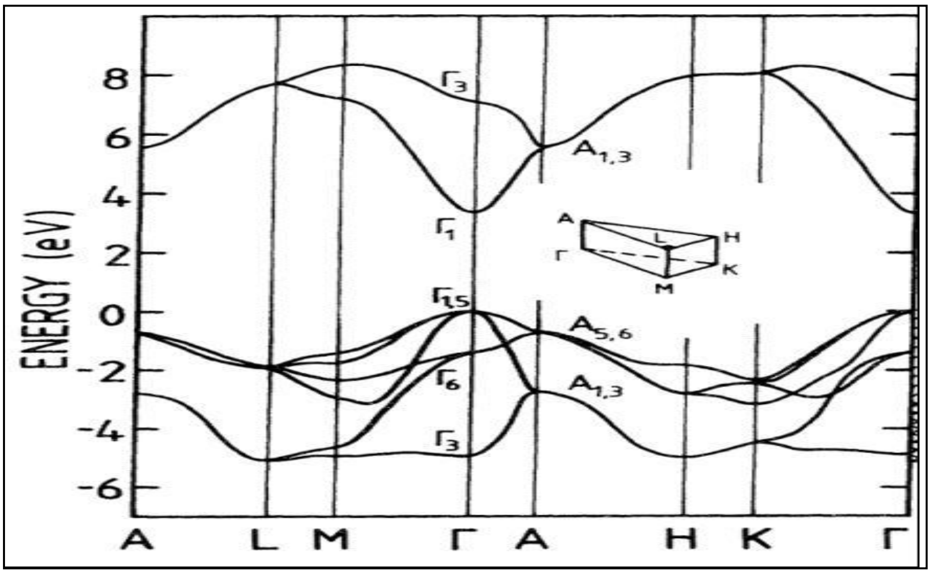

Figure 2.5 band structure of ZnO calculated using an empirical tight–binding Hamiltonian.

UV reflection/absorption or emission techniques are used to measure the electronic core levels in solids. These methods measure the energy difference between the upper valence-band states and the bottom conduction-band states. The zero energy in these graphs is taken as the upper edge of the valence band [30].

The conduction band of wurtzite ZnO is constructed from s-like states and it is symmetrical about the Γ point, while the valence band is constructed mainly from p-like states. The band structure E (k) for ZnO, calculated by Ivanov et al. [31] using an empirical tight– binding Hamiltonian, is given along the symmetry lines in the Brillouin zone in Figure 2.5 (The optical band gap between occupied and empty bands (i.e. between Γ1.5 and Γ1) in ZnO is about 3.37 eV. This energy represents the energy difference between full and empty states. The top filled states are called the valence band and the maximum energy of the valence band of states is called the VBM. The lowest band of empty states above the gap is called the conduction band with the lowest point in that band called the CBM. In this figure, the VBM (valence band minimum) and CBM coincide at k = 0, the Γpoint, indicating that ZnO is a direct band gap semiconductor. Again, six valence bands can be seen between –6 eV and 0 eV. In Figure 2.5 according to Ivanov et al, these are derived from the 2p orbitals of oxygen. For the conduction band there are two bands visible (above ~3 eV). These states are strongly localized on the Zn and correspond to unoccupied Zn 3s levels.

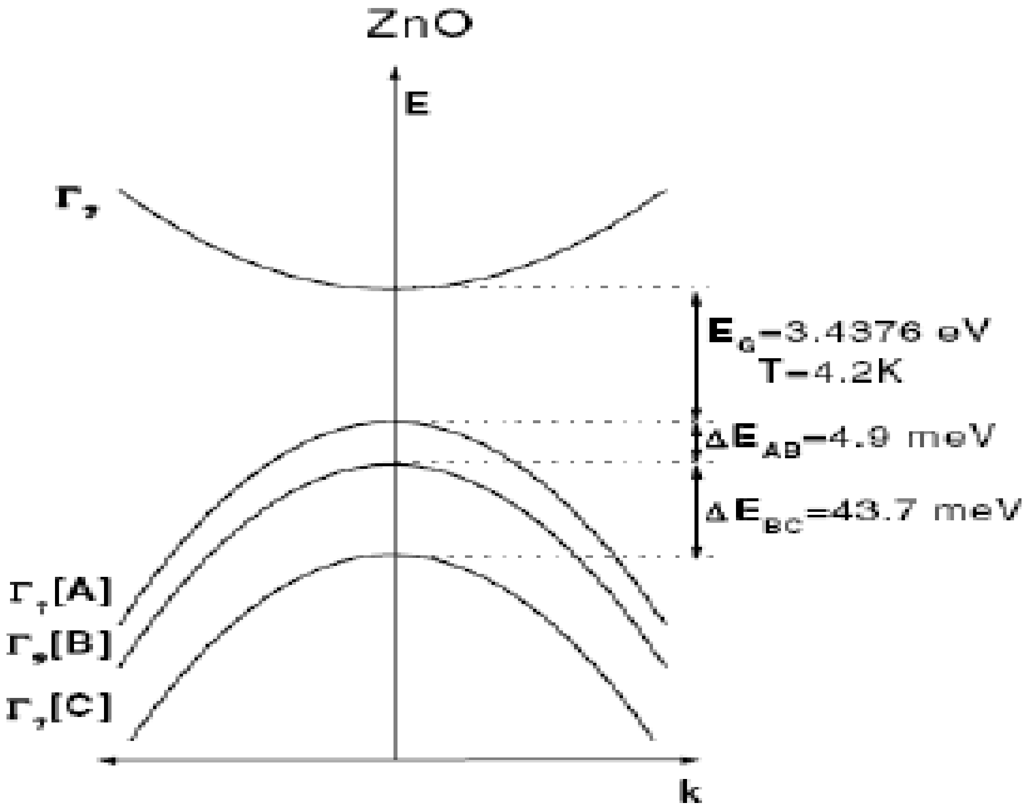

Figure 2.6 Low temperature band structure of ZnO showing valence band splitting into three (A, B, C) which is caused by crystal field and spin-orbit splitting [32**]**

In addition, it is also worth to know that the ZnO valence band is split experimentally by crystal field and spin orbit interaction into three states named A, B and C under the wurtzite symmetry. This splitting is schematically illustrated in Figure 2.6. The A and C subbands are known to possess Γ7 symmetry, whilst the middle band, B, has Γ9 symmetry. [These three bands correspond to light hole (A), heavy holes (B) and the crystal field split band (C). The band splitting values are measured at 4.2 K.

2.4 Luminescence in ZnO

Light emission through any process other than blackbody radiation is called luminescence and requires external excitation as it is a non-equilibrium process.

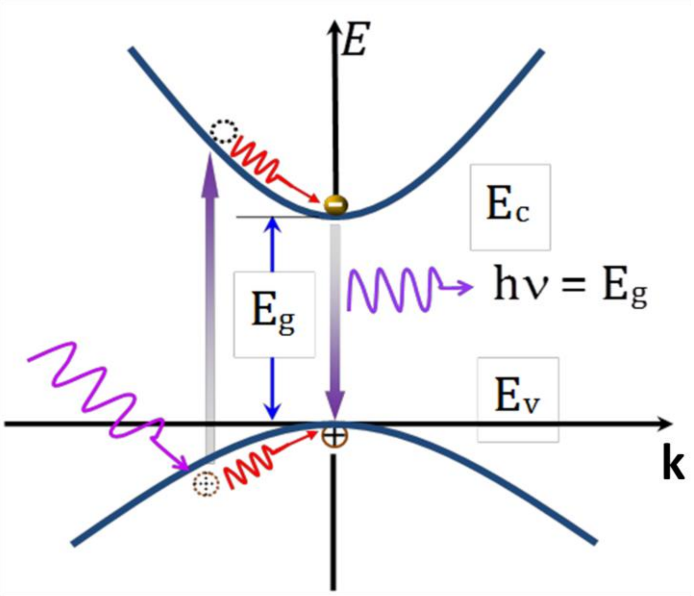

Figure 2.7 Band diagram illustration of the different processes that make up the photoluminescence spectra: (a) excitation relaxation and recombination in *k*-space

Based on the excitation source, luminescence is referred to either as photoluminescence (PL) (caused by absorption of photons), electroluminescence (EL) (caused by electric current), cathodoluminescence (CL) (caused by an electron beam), chemoluminescence (caused by chemical reactions) or thermoluminescence (caused by heat).

Basic principles of PL and the possible emission lines in ZnO are described below. Luminescence in semiconductors is the direct result of electron transitions from higher to lower energy levels. Figure 2.7 shows the simplified band structure of a semiconductor near the centre of the first Brillouin zone, where a material with band gap energy Eg is irradiated by a laser with energy hν>Eg, resulting in the excitation of an electron into the conduction band (arrow 1) and leaving a hole behind in the valence band. An electron-hole (e-h) pair is thus generated. The electrons and holes thermalize to the lowest energy state of their respective bands via phonon emission (shown by the red-wavy arrows) before recombining (arrow 2) across the fundamental band gap or the defect levels within the band gap and emitting photons of the corresponding energies in two basic mechanism.

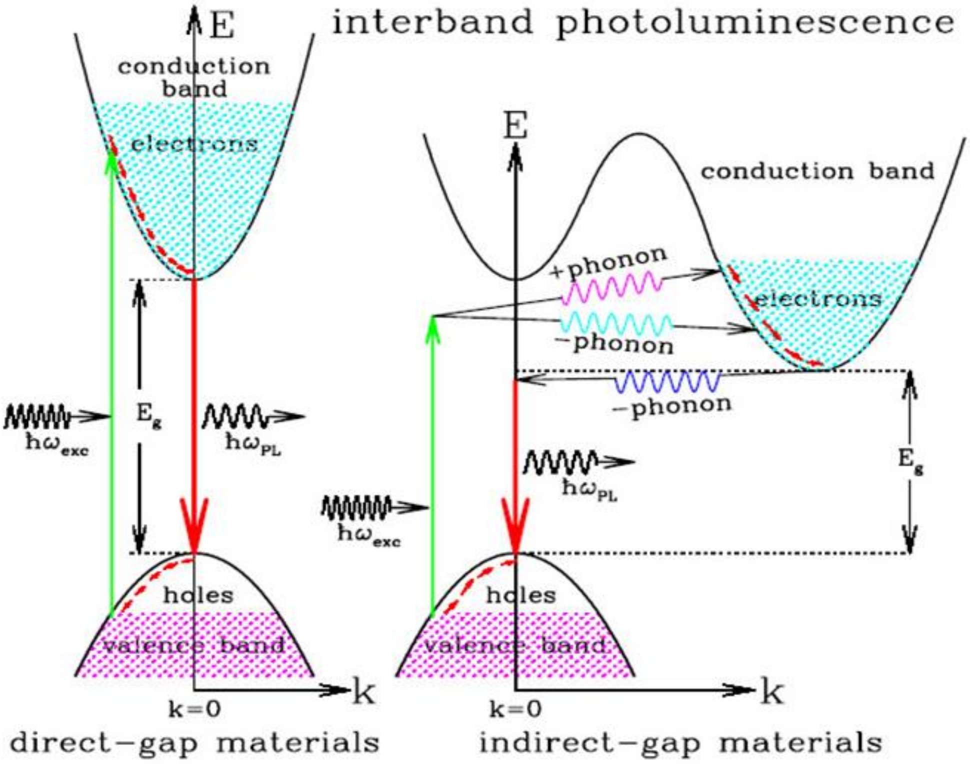

(a) **(b)**

Figure 2.8 Schematic illustration of common recombination [33] (a) Radiative recombination of an electron-hole pair accompanied by the emission of a photon with energy hv ≈ Eg. (b) non-radiative recombination events, the energy released during the electron-hole recombination is converted to phonons.

There are two basic recombination mechanisms in semiconductors, namely radiative recombination and non-radiative recombination as illustrated in Figure 2.8(a and b). In a radiative mechanism, one photon with energy equal to or near the bandgap energy of the semiconductor is emitted due to electron–hole recombination [34]. A recombination process that does not produce photons is known as nonradiative recombination during which the energy is exchanged with the lattice as heat through phonon emissions within defect states in semiconductor or its energy is transferred to other carriers. The defects in the crystal structure include impurities, native defects and dislocations. In compound semiconductors, the so called native defects include interstitials, vacancies, and antisite defects. It is quite common for such defects to form one or several energy levels within the forbidden gap of the semiconductor. These levels contribute to radiative or nonradiative recombination. Energy levels within the gap of the semiconductor are efficient recombination centers; in particular, if the energy level is close to the middle of the gap.

For all intent and purpose, the contribution from the non-radiative recombination in light-emitting devices should be as less as possible. Non-radiative recombination occurs mainly through three physical mechanisms, but cannot be detected by PL. These are Auger recombination, recombination at defects in the bulk and surface recombination. Recombination at defects in the bulk and surface regions of ZnO are expected to be the major non-radiative recombination processes.

Several radiative transitions between the conduction band and valence band can achieve luminescence in semi-conductor. They are exciton, donor and acceptor levels, as shown in Figure 2.9. Upon excitation at energy above the band gap, free electrons are created in the conduction band together with the free holes in the valance bond. These carriers will energetically relax down the band edge. Due to mutual coulomb interaction, electron-hole pair is formed. This electron-hole is usually called a free exciton (FX). Its energy is slightly smaller than the bang gap energy. This energy difference is the binding energy of the free exciton. A neutral donor (acceptor) will give rise to an attractive potential, a free exciton might be captured at the acceptor (donor). A bound exciton (DX) is formed.An electron bound to a donor can recombine directly with a free hole from a valence band. This kind of recombination is called free-to-bound transition (AX). The recombination energy for such a transition corresponds to the band gap energy reduced with the binding energy of donor. Another possibility is that a hole bound to an acceptor recombines with an electron bound to a donor in donor-acceptor pair (DAP) transition. Both the donor and the acceptor are neutral before the recombination (i.e. the donor positively and the acceptor negatively charged). Thus there is a Coulomb interaction between the donor and acceptor after the transition and extra Coulomb energy is gained in the final state added to the radiative recombination energy. The transition energy E (R) depends on the distance R between the donor and acceptor atoms.

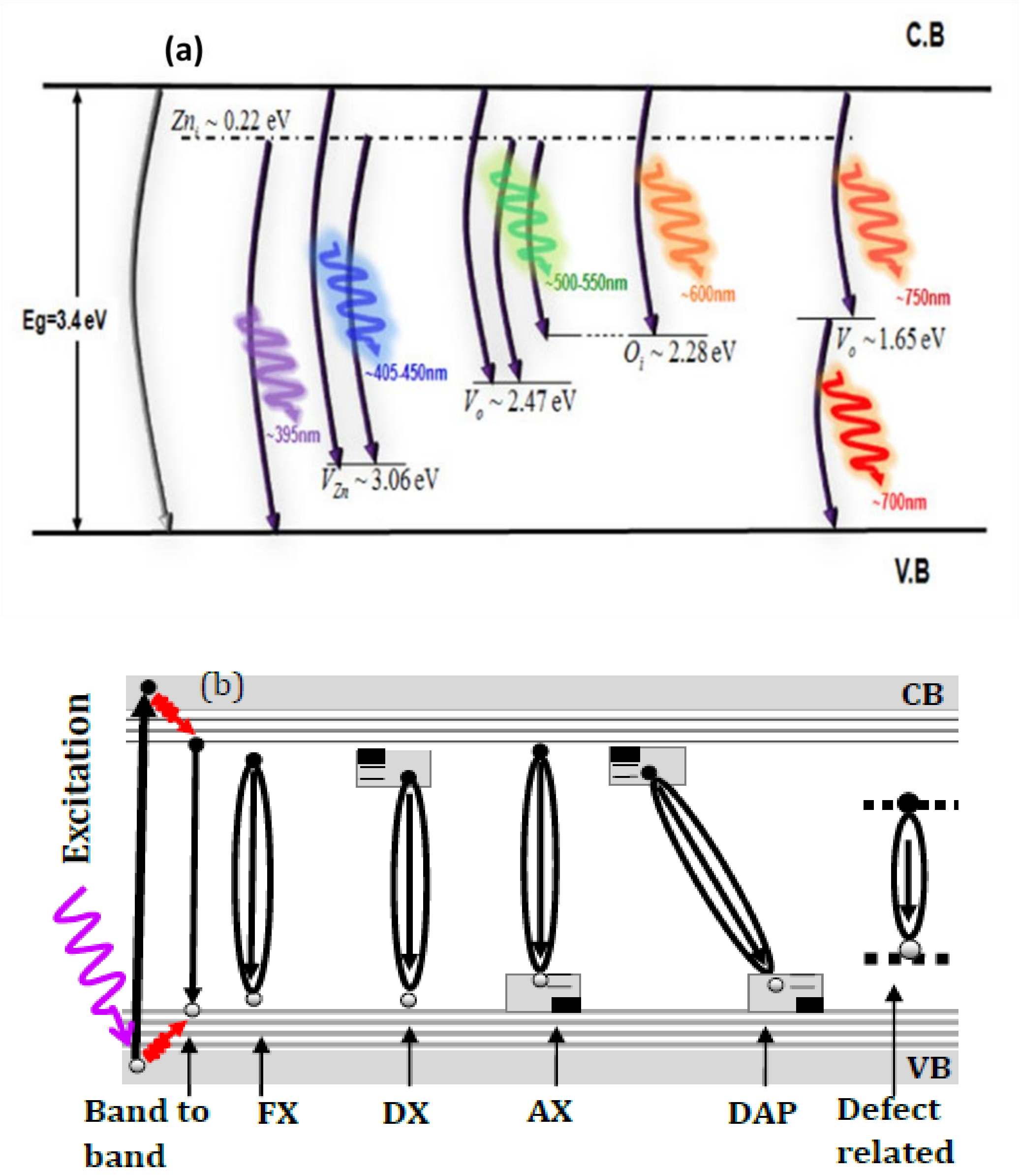

Figure 2.9 (a) and (b) Band diagram illustrations showing possible mechanisms recombination that makes up the photoluminescence spectra [35].

The optical transitions in a semiconductor can either be intrinsic or extrinsic. Intrinsic transitions deal with the transitions from conduction to valence band, including excitonic effects due to coulomb interactions while extrinsic transitions are created in the bandgap by dopants/impurities or point defects and complexes, which usually influence both optical absorption and emission processes as they create discrete energy levels inside the band gap. [36,37]. In the case of ZnO, a PL spectrum at room temperature usually contains two emission bands resulting from both effects as shown in Figure 2.10.

These emission bands can be categorized as a UV emission band and a broad emission band. The UV emission band is related to a near band-edge transition of ZnO, namely, the recombination of the free excitons and is associated with intrinsic effects. The broad emission band literally between 420 nm and 700 nm are observed nearly in all samples regardless of growth conditions is called deep level emission band (DLE) which is caused by extrinsic effects.

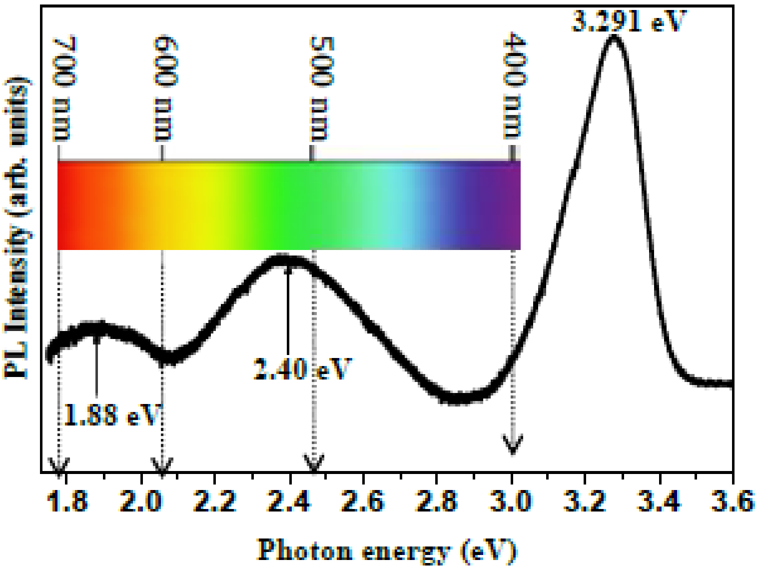

Figure 2.10 A typical PL spectrum of as grown ZnO nanoparticles with the excitation wavelength of 350 nm.

The DLE band has previously been attributed to several defects in the crystal structure such as O-vacancy (V_O) [38-40], Zn-vacancy (V_{Zn}) [41-43] O-interstitial (O_i) [44] Zn-interstitial (Z_{ni}) [45] and extrinsic impurities such as substitutional Cu [46]. Recently, this deep level emission band had been identified and at least two different defect origins (V_O and V_{Zn}) with different optical characteristics were claimed to contribute to this deep level emission band [47-49]. PL is a powerful tool to study point defects in wide-band gap semiconductors. Most of the experimental results on point defects in ZnO have been obtained from the analysis of mainly the PL data [50]. The optical properties of ZnO contain a lot of information, such as optical absorption, transmission, reflection, Photoluminescence and so on. Quantum confinement of electrons in small grains created by potential barriers at the grain boundaries are thought to be responsible for the drastic change in band gap. Sometimes also at higher doping concentration on a blue shift towards shorter wavelength has been observed and can be explained on the basis of Burstein–Moss effect. Quantum confinement occurs in nanocrystals when their size is reduced so that it approaches the size of the exciton Bohr radius (the size of an exciton in a bulk crystal). For ZnO, the exciton Bohr radius is ~ 2.34 nm. PL can be used to observe the quantum confinement effect in nanostructures. However, there are few reports on this effect in ZnO nanostructures. Experimental evidence of quantum confinement effects have been reported by Gu et. al. [51] where PL and absorption spectra from nanostructures with radii of 1.1 nm were found to be blue shifted compared to the spectra of bulk materials. Lu et al. [52] also observed quantum confinement effects in the PL spectra of quantum dots with diameter as large as 15 nm and 6 nm in height. The quantum dots studied by Lu et. al exhibited a strong free exciton adsorption at 3.41 eV at room temperature, significantly larger than that in bulk ZnO (3.37 eV), representing a 90 meV blue-shift.

2.5 Physical properties of ZnO

Table 2.1 Some physical properties of ZnO [53, 54] important physical parameters of ZnO are summarized in Table 2.1.

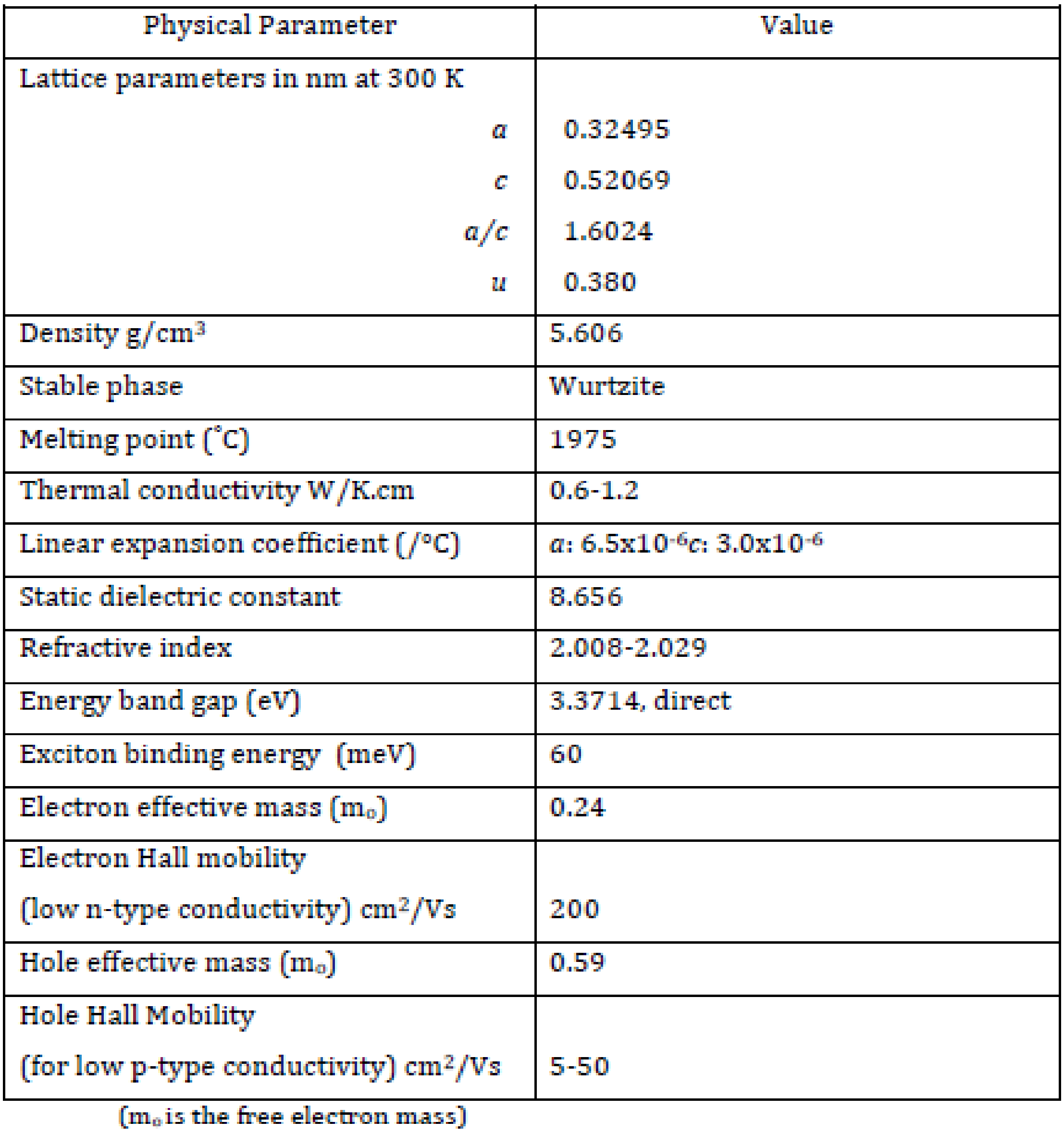

Physical Parameter	Value
Lattice parameters in nm at 300 K	
a	0.32495
c	0.52069
a/c	1.6024
u	0.380
Density g/cm^3	5.606
Stable phase	Wurtzite
Melting point (˚C)	1975
Thermal conductivity W/K.cm	0.6-1.2
Linear expansion coefficient (/°C)	a: $6.5x10^{-6}$ c: $3.0x10^{-6}$
Static dielectric constant	8.656
Refractive index	2.008-2.029
Energy band gap (eV)	3.3714, direct
Exciton binding energy (meV)	60
Electron effective mass (m_o)	0.24
Electron Hall mobility (low n-type conductivity) cm^2/Vs	200
Hole effective mass (m_o)	0.59
Hole Hall Mobility (for low p-type conductivity) cm^2/Vs	5-50

(m_o is the free electron mass)

It should be noted that there is still uncertainty in some values like hole mobility, thermal conductivity etc.

2.6 Applications of ZnO nanostructures.

Each property of ZnO has its own applications. Starting from the wide band gap of ZnO makes it able to form clusters consisting of ZnO nanocrystals and ZnO nanowires. Also due to the wide band gap, synthesis of P–N homojunctions has been reported in some literatures. Many fine optical devices can be fabricated based on the free-exciton binding energy in ZnO that is 60 meV because large exciton binding energy makes ZnO eligible to persist at room temperature and higher too. Since ZnO crystals and thin films exhibit second- and third-order non-linear optical behaviour, it can be used for non-linear optical devices. Generally, the advantage of tuning the physical property of these oxides like zinc oxide becomes the root cause for the synthesis of smart application device. The electrical, optical, magnetic, and chemical properties can be very well tuned by making permutation and combination of the two basic structural characteristics they possess as cations with mixed valence states, and anions with deficiencies (vacancies). Figure 2.11 below provides a summary of various applications of ZnO.

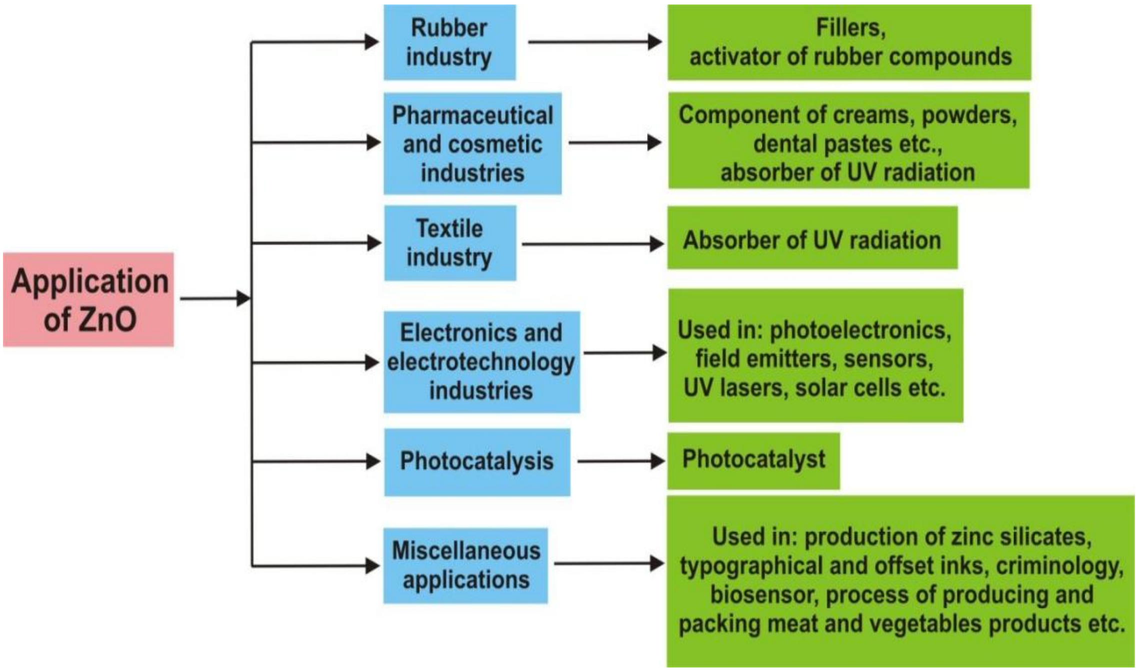

Figure 2.11 schematic representations of all the application of ZnO [55]

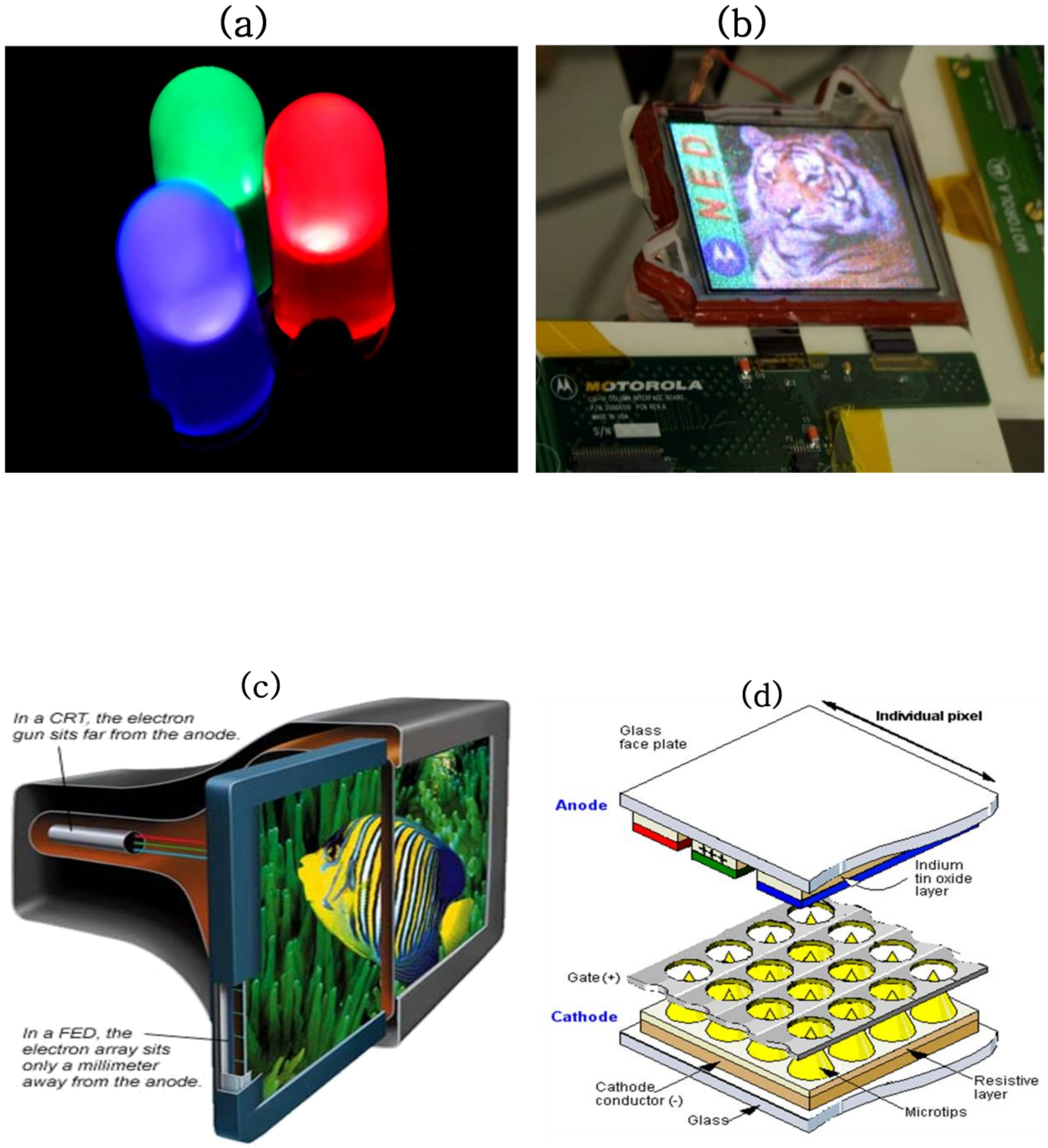

Figure 2.12 Pictorials of some applications of ZnO (a) pure green and blue LEDs (b) TV (c) Cathode Ray Tube and (d) Solar cells.

DSSCs is an optoelectronics device that converts light to electrical energy via charge separation in sensitizer dyes absorbed on a wide band gap semiconductor, which is different to conventional solar cells[56**].**

References

[1] Reynolds D. C, Litton C. W, Collins T. C 1965." Zeeman Effects in the Edge Emission and Absorption of ZnO," *Physical Review*, vol. 140 p. A1726.

[2] Moezzi A, McDonagh A. M, Cortie M. B 2012."Zinc oxide particles: Synthesis, properties and applications," *Chemical Engineering Journal*, vol. 185 186, pp.1– 22.

[3] Scopus, Document search with a key word "ZnO" accessed 03-09-2014. [Online http://www.scopus.com/results/results.url].

[4] Morkoc H , Ozgur U 2009 Zinc *Oxide: Fundamentals, Materials and Device Technology*. Germany: WILEY-VCH, Copyright ISBN: 978-3-527-40813-9

[5] Uzgur U, Alivov Ya. I, Liu C, Teke A, Reshchikov M. A, Dogan S, Avrutin V, Cho S.J, Morkoc H 2005"A comprehensive review of ZnO materials and devices," *J. Appl. Phys., vol.* 98, p. 041301

[6] Yu Z. G, Gong H, Wu P.I 2006. "Lattice dynamics and electrical properties of wurtzite ZnO determined by a density functional theory method," *J. Crysl. Growth*, vol. 287, pp. 199–203

[7] Mehrabian M, Azimirad R, Mirabbaszadeh K, Afarideh H, Davoudian M 2011"UV detecting properties of hydrothermal synthesized ZnO nanorods," *Physica E,* vol. 43, pp. 1141-1145.

[8] Huang M. H, Wu Y, Feick H, Tran N, Weber E , Yang P 2001 Catalytic growth of zinc oxide nanowires by vapor transport, *Adv. Mater.* 13 113116

[9] Wang Z. L 2004 Zinc oxide nanostructures: growth, properties and applications Phys.: *Condens. Matter* 16 R829–R858.

[10] Jagadish C, Pearton S. J 2006 Zinc oxide bulk, thin films and nanostructures:

processing, properties and applications, Publisher: *Elsevier Science*, 1 edition, pp 3

[11] Wang Z.L 2004 *J. Phys. Condensed Matter*, 16829.

[12] Hellwege K. H, Madelung O, Hellege A. M 1987 *Condensed Matter* 19 119-595.

[13] Materials 2014, *7*, 2833-2881; doi: 10.3390/ma7042833].

[14] Lee Y G, Yamamoto H, Kourogia M, Ohtsua M 2001 *Thin Solid Films*, 386117 120.

[15] Meyer B. K, Alves H, Hofmann D. M, Kriegseis W. et. al. 2004 Phys. *Stat. Sol.*,241231- 260.

[16] TingtingRen, Holly R. Baker, Kristin M. Poduska 2007 *Thin Solid Films,* 515(7976–7983.

[17] Rössler U 1969 Energy bands of hexagonal II-VI semiconductors, *Phys. Rev*. 184 733-738.

[18] Bloom S, Ortenburger I 1973 Pseudopotential band structure of ZnO, *Phys. Stat. Sol.* (b) 58561-566.

[19] Oshikir M.i, Aryasetiawan F 1999 Band gaps and quasiparticle energy calculations on ZnO, ZnS, and ZnSe in the zinc-blende structure by the GW approximation, *Phys. Rev. B*6010754-10757.

[20] Usuda M, Hamada N, Kotani T, Schilfgaarde M van 2002 All-electron GW calculation based on the LAPW method: application to wurtzite ZnO, Phys. Rev.B 66 125101.

[21] Xu Y. N , Ching W. Y 1993 Electronic, optical, and structural properties of some wurtzite crystals, *Phys. Rev. B* 484335 -4351

[22] Schröer P, Krüger P , Pollmann J, 1993 First-principles calculation of the electronic structure of the wurtzite semiconductors ZnO and ZnS, *Phys. Rev. B* 476971-6980.

[23] Schleife A, Fuchs F, Furthmüller J , Bechstedt F 2006 First-principles study of ground- and excited-state properties of MgO, ZnO, and CdO polymorphs, *Phys. Rev. B* 73 245212.

[24] Langer D.W , Vesely C.1970 *J Electronic Core Levels of Zinc Chalcogenides*, *Phys. Rev. B*, 2 4885-4892.

[25] Ley L, Pollak R. A, McFeely F. R, Kowalczyk S. P , Shirley D. A 1974 Total valence-band densities of states of III-V and II-VI compounds from x-ray photoemission spectroscopy, *Phys. Rev. B* 9 600-621.

[26] Dong C. L, Persson C, Vayssieres L, Augustsson A, Schmitt T, Mattesini M, Ahuja R, Chang C. L , Guo J.-H 2004 Electronic structure of nanostructured ZnO from x-ray absorption and em ission spectroscopy and the local density approximation, *Phys. Rev. B*70 195325.

[27] Preston A. R. H, Ruck B. J, Piper L. F. J, DeMasi A, Smith K. E, Schleife A, Fuchs F, Bechstedt F, Chai J , Durbin S. M 2008 Band structure of ZnO from resonant x-ray emission spectroscopy, *Phys. Rev. B* 78 155114.

[28] King P. D. C, Veal T. D, Schleife A, Zuñiga-Perez J, Martel B, Jefferson P. H, Fuchs F, Muñoz-Sanjose V, Bechstedt F, McConville C. F 2009 Valence-band electronic structure of CdO, ZnO, and MgO from X-ray photoemission spectroscopy and quasi-particle-corrected density-functional theory calculations , *Phys. Rev. B* 79 205205.

[29] Vogel D, Krüger P , Pollmann J 1995 Ab initio eletronic-structure calculations for II-I semiconductors using self-interaction-corrected pseudopotentials, *Phys. Rev. B* 52 R14316-R14319.

[30] Meyer B. K, Alves H, Hofmann D. M, Kriegseis W, Forster D, Bertram F, Christen J,

Hoffmann A, Straßburg M, Dworzak M. A, Haboeck U, Rodina A. V 2004 "Bound exciton and donor– acceptor pair recombinations in ZnO," *phys. stat. sol. (b),* vol. 241, pp. 231 – 260.

[31] Ivanov I, Pollmann J 1981 "Electronic structure of ideal and relaxed surfaces of ZnO: A prototype ionic wurtzite semiconductro and its surface properties," *Phys. Rev. B*, vol. 24, p. 7275.

[32] Preston A. R. H, Ruck B. J, Piper L. F. J, DeMasi A, Smith K. E, Schleife A, Fuchs F, Bechstedt F, Chai J, Durbin S.M 2008 "Band structure of ZnO from resonant x-ray emission 158 spectroscopy," *Phys. Rev. B*, vol. 78, p. 155114.

[33] Yang L.L "Synthesis and Characterization of ZnO Nanostructures," Linkoping University.

[34] Fred Schubert E 2006 Light-emitting Diodes, second edition, *Cambridge UniversityPress* pp27-47.

[35] http://www.scribd.com/doc/21053651/Electronic-spectroscopy-UV-Visible.

[36] Özgür Ü, Alivov Ya. I, Liu C, Teke A, Reshchikov M. A, Doğan S, Avrutin V, Cho S. J and Morkoç H.A 2005 comprehensive review of ZnO materials and devices, *J. Appl. Phys.* 98 041301.

[37] Jagadish C , Pearton S (Editors) 2006 Zinc oxide bulk, thin films and nanostructures, *Elsevier Limited* pp175.

[38] Kasai P. H 1963 Electron spin resonance studies of donors and acceptors in ZnO, *Phys. Rev.*130 989-995.

[39] Vanheusden K, Warren W. L, Seager C. H, Tallant D. R, Voigt J. A , Gnade B .E 1996 Mechanisms behind green photoluminescence in ZnO phosphor powders, *J. Appl. Phys.*797983-7990.

[40] Yamauchi S, Goto Y , Hariu T 2004 Photolum inescence studies of undoped and nitrogen-doped ZnO layers grown by plasma-assisted epitaxy, *J. Cryst. Growth* 260 1- 6.

[41] Liu M, Kitai A. H , Mascher P1992 Point defects and luminescence centres in zinc oxide and zinc oxide doped with manganese, *J. Lumin.* 54 35-42.

[42] Bylander E.G 1978 Surface effects on the low-energy cathodoluminescence of zinc oxide, *J. Appl. Phys.* 49 1188-1195.

[43] Yang X, Du G, Wang X, Wang J, Liu B, Zhang Y, Liu D, Liu D, Ong H. C , Yang S2003 Effect of post-thermal annealing on properties of ZnO thin film grown on c-Al2O by metal-organic chemical vapor deposition, J. Cryst. Growth 252 275-278. 3

[44] Zhong J, Kitai A. H, Mascher P , Puff W 1993 The Influence of Processing Conditions on Point Defects and Luminescence Centers in ZnO, J. Electrochem. Soc. 140 3644 3649.

[45] Johnston K, Henry M. O, Cabe D. M, Agne T , Wichert T 2004 Proceedings of the Second Workshop on "*SOXESS European Network on ZnO*, 27-30 October, Caernarfon, Wales, UK.

[46] Dingle R 2008 Luminescent transitions associated with divalent copper impurities and the green emission from semiconducting zinc oxide, Phys. Rev. Lett. 23 (1969) 579 581 Communication 145 321-326.

[47] Zhao Q. X, Klason P, Willander M, Zhon H. M, Lu W and Yang J. H 2005 Deep-level emissions influenced by O and Zn implantations in ZnO, *Appl. Phys. Lett*. 87 211912-1.

[48] Moe Børseth T, Svensson B. G, Kuznetsov A.Yu, Klason P, Zhao Q.X , Willander M 2006 Identification of oxygen and zinc vacancy optical signals in ZnO,*Appl. Phys. Lett.* 89 262112-1-3.

[49] Klason P, Børseth T. M, Zhao Q. X, Svensson B. G, Kuznetsov A. Y, Bergman P. J,

Willander M Temperature dependence and decay times of zinc and oxygen vacancy related photoluminescence bands in zinc oxide, Solid State.

[50] PijusKanti Samanta , Partha Roy Chaudhuri,Scienceb of Advanced Mater.,3(2011)107112. 35

[51] Gu Y, Kuskovsky I. L, Yin M, O’Brien S, Neumark G. F 2004 "Quantum confinement in ZnO nanorods," *Appl.Phys.Lett., vol. 85*, p. 3833.

[52] Jagadish C , Pearton S. J 2006 “Zinc Oxide Bulk, Thin Films and Nanostructures Processing, Properties and Application” Elsevier.G. Blasse, B.C. Grabmailer, Springe Verlag, 1994.

[53] Lu J. G, Ye Z. Z, Huang J. Y, Zhu L. P, Zhao B. H, Wang Z. L, Fujita Sz 2006"ZnO quantum dots synthesized by a vapor phase transport process,"*Appl.Phys.Lett., vol. 88*, p.063110.

[54] Dangbegnon J.K "Photoluminescence study of ZnO doped with nitrogen and arsenic," Nelson Mandela Metropolitan University, PhD thesis 2010.

[55] Haynes J. R "Experimental proof of the existence of a new electronic complex in silicon,"

Chapter 3

Experimental methods and characterization techniques

A detailed description of the experimental methods and procedures used in growing the nanoparticles by sol-gel method and characterization techniques used to analyze the nanoparticles are introduced in this chapter.

3.1 Precursors

The chemicals used in this work were purchased from Sigma Aldrich and used as-received (i.e. no further purification was attempted). Zinc acetate dihydrate ($Zn(CH_3COO)_2 \cdot 2H_2O$), was used as zinc precursors having purity of 99%. Sodium hydroxide (NaOH) was used as the hydroxide sources. Ethanol (98%) and water were used as solvents. Ethanol and sodium hydroxide take care for the homogeneity and PH value of the solution and helps to make a stoichiometric solution to get zinc oxide nanoparticles [1]

3.2 Synthesis of ZnO nanoparticles

Materials in its nano form is known to be more demandable than in its bulk form because in nano level the material undergoes a drastic change in its property and has versatile application. The properties of zinc oxide makes the material capable of exiesting in various shapes in the form of nanostructures such as tubes, wires, rods, belts, rings, cages and springs exhibiting varieties of properties like piezoelectricity, optical transparency, conductivity, solar cell, UV and visible photoluminescence, optical nonlinearity and many more. ZnO nanoparticles were grown using a combination of zinc acetate dihydrate as a zinc precursor and sodium hydroxide as a source of hydroxyl groups. These two precursors were dissolved separately in deionised water or ethanol or water-ethanol mixture at room temperature. The zinc precursor was placed in a flask while being stirred. When the temperature of the solution reached the desired growth temperature, the hydroxide precursor was added drop-by drop using a burette. The solutions were mixed for approximately 1 hour at constant temperature under continual stirring.

Mixing conditions: The solution in three necked Reflux bottle was preheated to the desired growth temperature. When the zinc solution reached the required temperature (varied from 25 – 80 °C), the hydroxide precursor was added drop by drop.

Growth temperature: This was varied from room temperature – 75 °C, for all the solvents used.

Drying process: The samples were rinsed several times in deionised water and gently different structures of ZnO nanoparticles were grown by varying growth temperature, solvent volume ratios, the type of dopants and annealing temperature on the properties of the nanoparticles are presented in chapter 4.

Annealing: Post-growth thermal treatment was carried out at 600 ℃ in air. Annealing was performed for different solvent volume ratios and various growth temperatures and the effects on the optical and structural properties were investigated.

A wide variety of nanostructures have been demonstrated and fabricated by different research groups using different techniques. Methods which are related to the synthesis of various shapes of zinc oxide nanostructures are chemical and thermal vapour deposition laser ablation, vacuum arc deposition, electrochemical, and hydrothermal process. But all these methods reportedly possess many complex steps; require sophisticated equipment and rigorous experimental conditions [4]. Sol-gel technique is simple, economical, and environmentally friendly and provides a method for a large-scale fabrication of ZnO nanoparticles at low cost, but also open a way to the size-controlled fabrication of other materials. Therefore, the aim of this study is to optimize growth of ZnO nanoparticles using a simple sol-gel technique.

The growth of ZnO from zinc acetate dihydrate precursor using sol–gel process generally undergoes four stages, such as solvation, hydrolysis, polymerization and transformation into ZnO. The zinc acetate dihydrate precursor was first solvated in ethanol, and then hydrolyzed, regarded as removal of the intercalated acetate ions and results in a colloidal–gel of zinc hydroxide (Eq. (5), size and activity of solvent have obvious influence on the reacting progress and product. Ethanol has smaller size and a more active –OH. Ethanol can react more easily to form a polymer precursor with a higher polymerization degree, which is required to convert sol into gel [2]. These zinc hydroxide splits into Zn^{2+} cation and OH− anion according to reactions (Eq. (3.4)) and followed by polymerization of hydroxyl complex to form "Zn–O–Zn" bridges and finally transformed into ZnO (Eq. (3.5)) [3]

$$[CH_3\text{-}CO\ (H_2O)\text{-}O\text{-}Zn\text{-}O\text{-}CO\ (H_2O)\text{-}CH_3\ ]+ [N\ (CH_2\text{-}CH_2\text{-}OH)_3\ ] \qquad (3.1)$$

$$[CH_3\text{-}CO\ (H_2O)\text{-}O\text{-}Zn\text{-}O\text{-}CO\ (H_2O)\text{-}CH_3] \longrightarrow (CH_3\text{-}CO\text{-}O\text{-}Zn)^{+} + [O\text{-}CO\text{-}CH_3{}^{-} +$$

$$2H^{+} + 2OH^{-} \qquad (3.2)$$

$$(CH_3\text{-}CO\text{-}O\text{-}Zn)^{+} + [N\ (CH_2\text{-}CH_2\text{-}OH)_3] \longrightarrow (CH_3\text{-}CO\text{-}O\text{-}Zn)\ N\ (CH_2\text{-}CH_2\text{-}OH)_2 +$$

$$(CH_2\text{-}CH_2\text{-}OH)^{-} \qquad (3.3)$$

$$Zn\ (OAc)_2 \longrightarrow 2Zn2^{+} + 2(OAc)^{-} \qquad (3.4)$$

$$Zn^{2+} + 2OH^{-} \longrightarrow Zn\ (OH)_2 \longrightarrow ZnO + H_2O \qquad (3.5)$$

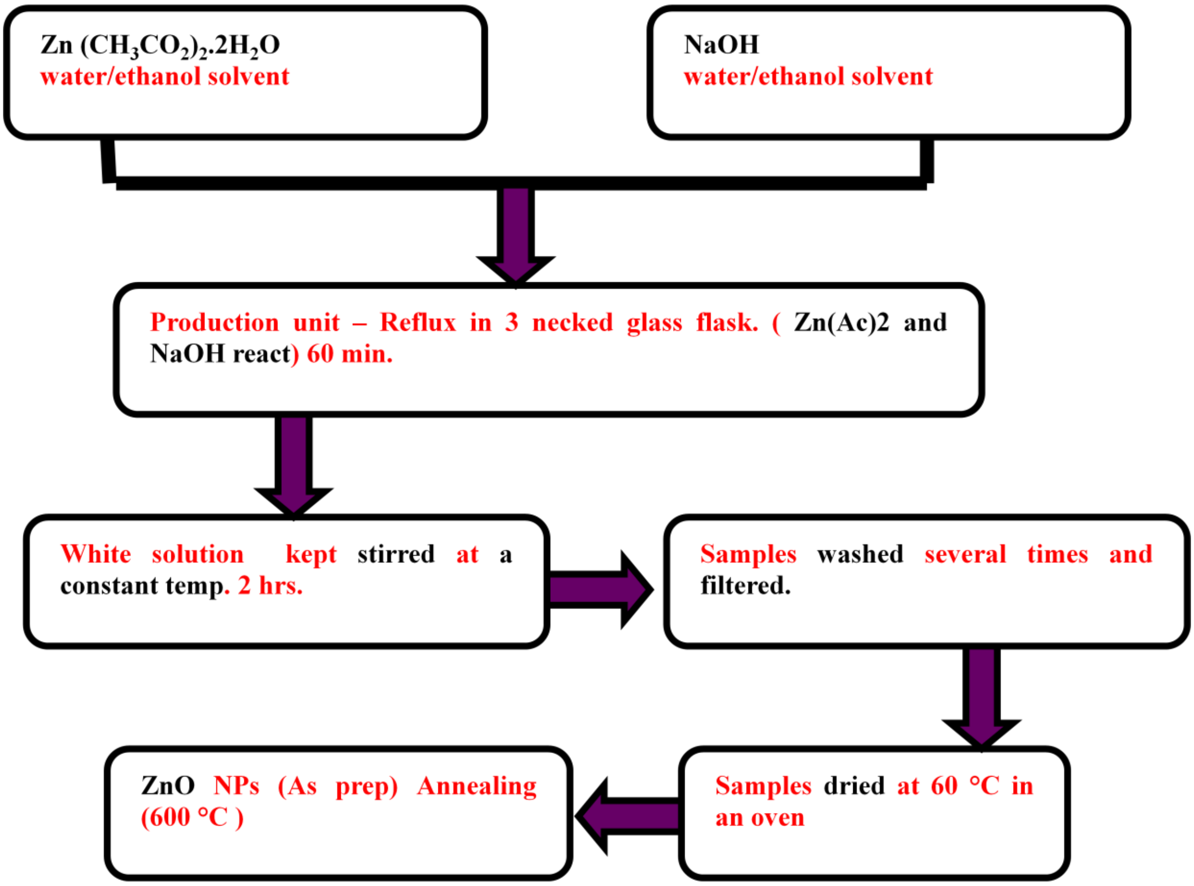

Figure 3.1 Flow diagram of sol-gel process used in the synthesis of ZnO nanoparticles in this project.

3.3 Characterization techniques

3.3.1 X-ray diffraction (XRD)

XRD is the science of determining the arrangement of the atoms within a crystal from the manner in which a beam of X-rays is scattered from the electrons within the crystal. Up to 1895 the study of matter at the atomic level was a difficult task but the discovery of electromagnetic radiation with 1 Å (10^{-10} m) wavelength, appearing at the region between gamma-rays and ultraviolet, makes it possible. As the atomic distance in matter is comparable with the wavelength of X-ray, the phenomenon of diffraction find its way through it and gives many profitable results related to the crystalline structure. X-ray diffraction (XRD) is a versatile, non-destructive technique used for qualitative and quantitative analysis of a crystalline materials. This experimental technique has been used to determine the overall structure of bulk solids, including lattice constants, identification of unknown materials, orientation of single crystals, orientation of polycrystalline, stress, strain, texture, films thickness etc. XRD analysis can provide the crystalline quality and dominant crystallographic planes of the given material. In addition, the diffraction spectrum also provides information regarding the types of phases present in the material and can be used to calculate the approximate average grain size using Scherrer's equation [3.9].

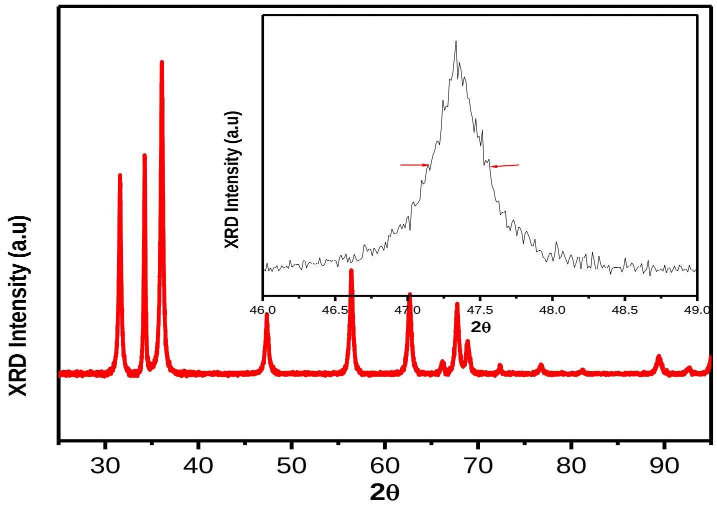

Figure.3.2 Typical XRD spectrum of ZnO nanoparticles.

In this study, D8 Bruker Advanced AXS GmbH X-ray powder diffraction system shown in Figure 3.4 with a resolution of 0.02 ° for 2θ and a Cu-Kα x-ray tube (λ=1.54056^{o}A) was used.

X-ray scans were performed between 2θ values of 30° and 80° using a step size of 0.05.In almost all samples, peaks related to the (101) plane were observed to dominate the spectrum. The relative intensity of this diffraction plane with respect to other dominant planes, (001) and (202) were used as a measure of the alignment of the nanoparticles.

X-rays are short-wavelength, high energy electromagnetic radiation, having the properties of both waves and particles. They can be described in terms of both photon energy (E) or wavelength, λ (lambda – the distance between peaks) and frequency *v* (nu – the number of peaks passing a point in a unit of time).The relation between energy, frequency or wavelength in the case of photon is:

$$E = hv = \frac{hc}{\lambda} \tag{3.6}$$

Substituting the values of the constants above in equation yield the following relationship

$$\lambda = \frac{12.4}{E}(KeV) \tag{3.7}$$

X-rays are produced whenever high energy electrons strike with metal target. All x-ray tubes contain two electrodes- an anode (the metal target) usually maintained, at ground potential, and a cathode maintained, at negative potential, normally of order of 30KV to 50KV for the diffraction work. Interaction that occur between the beam (i.e. electrons) and target will result in a loss of energy. A continuous spectrum is formed when the high energy electrons are slowed down rapidly by multiple collisions with the anode material, which give rise to white radiation, or Bremsstrahlung. But not every electron decelerates in the same way, some stop in one impact and release all their energy at once, while others deflect this way and that way when they encounter atoms of the target, successively losing fractions of their total kinetic energy until is all spent. Those electrons which are stopped in one impact produce photons of maximum energy (wavelength) equal to the energy loss [6]

Bragg’s Law

The atoms in crystals interact with X-rays in such a way as to produce interference. The interaction can be thought of as if the atoms in a crystal structure reflect the waves. But, because a crystal structure consists of an orderly arrangement of atoms, the reflections occur from the atomic planes. Consider a beam of monochromatic X-rays entering a crystal with one of its planes oriented at an angle of θ to the incoming beam. Figure 3.3 shows two such X-rays, where the spacing between the atomic planes occurs over the distance, d.

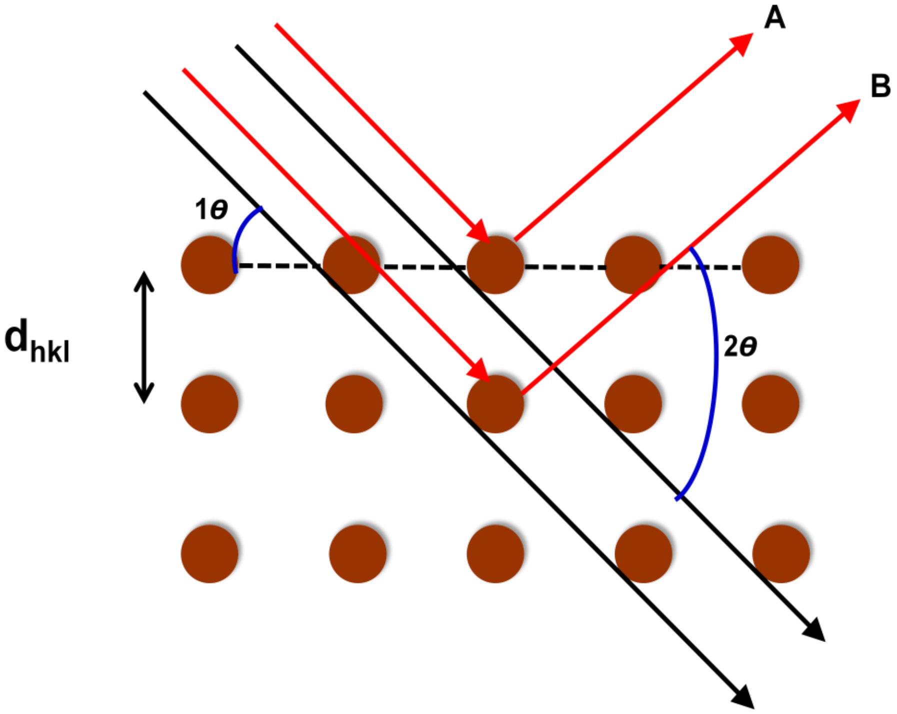

Figure 3.3 Monochromatic X-rays entering a crystal [6].

Ray A reflects off of the upper atomic plane at an angle θ equal to its angle of incidence. Similarly, Ray B reflects off the lower atomic plane at the same angle θ. While Ray B is in the crystal, however, it travels a distance of 2a farther than Ray A. If this distance 2a is equal to an integral number of wavelengths (nλ), then Rays A and B will be in phase on their exit from the crystal and constructive interference will occur. If the distance 2a is not an integral number of wavelengths, then destructive interference will occur and the waves will not be as strong as when they entered the crystal. Thus, the condition for constructive interference to occur is

$$n\lambda = 2a.$$

But, from trigonometry, we can figure out what the distance 2a is in terms of the spacing, d, between the atomic planes.

$$a = d \sin \theta, \qquad \text{or}$$

$$2a = 2\, d \sin \theta, \qquad \text{thus}$$

$$\mathbf{n\lambda = 2d \sin \theta} \tag{3.8}$$

This is known as **Bragg's Law** for X-ray diffraction.

What it says is that if we know the wavelength ,λ , of the X-rays going in to the crystal, and we can measure the angle θ of the diffracted X-rays coming out of the crystal, then we know the spacing (referred to as ***d-spacing***) between the atomic planes.

Figure 3.4 D8 Bruker Advanced AXS GmbH X-ray diffractometer at the University of the Free State

Crystallite size measurement

The diffraction peaks positions and relative intensities can be changed by the presence of various types of defects such as small number of dislocations in crystals with dimensions of millimeters. Small size of grain size can be considered as another kind of defect and can change diffraction peak widths. Very small crystals cause peak broadening. The crystallite size is easily calculated as a function of peak width (specified as the full-width at half maximum peak intensity (FWHM)), peak position and wavelength.

The curve of diffracted intensity vs. 2θ has the form of Figure 3.5(a) illustrating the hypothetical case of diffraction occurring only at the exact Bragg angle.

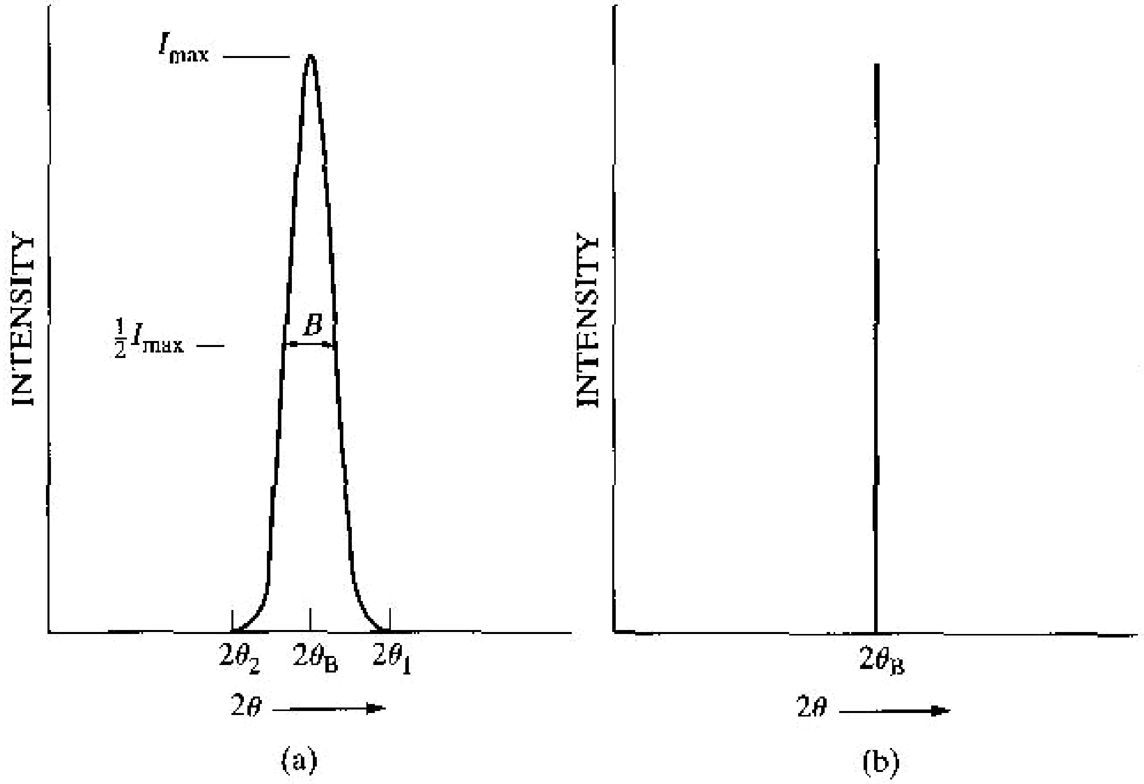

Figure 3.5 Effect of fine crystallite size on diffraction curves [1].

The width of the diffraction curve of Figure 3.5(a) increases as a thickness of the crystal decreases, because the angular range ($2\theta_1$ - $2\theta_2$) increases as m decreases. The width β is usually measured, in radians, at intensity equal to half the maximum intensity (FWHM).

Therefore

$$\beta = \frac{1}{2}(2\theta 1 - 2\theta 2) = \theta 1 - \theta 2$$

The path-difference equations for these two angles are similar, but related to the entire thickness of the crystal rather than to the distance between adjacent planes:

$$2\delta \sin\theta 1 = \frac{(m+1)}{\lambda} \qquad\qquad 2\delta \sin\theta 2 = \frac{(m-1)}{\lambda},$$

Where (m + 1) planes in this set, crystal has a thickness δ measured in a direction perpendicular to a particular set of Bragg planes

By subtraction,

$$2\delta Cos\frac{(\theta 1+\theta 2)}{2} Sin\frac{(\theta 1-\theta 2)}{2} = \lambda$$

But $\theta 1$ and $\theta 2$ are both very nearly equal to $\theta\beta$, so that $\theta 1 + \theta 2 = 2\theta\beta$ (approx.)

and $$Sin\frac{(\theta 1-\theta 2)}{2} = \frac{(\theta 1-\theta 2)}{2}$$ (approx.)

Therefore; $$2\delta\frac{(\theta 1-\theta 2)}{2} Cos\theta\beta = \lambda$$ or, $$\delta = \frac{\lambda}{\beta 1/2} Cos\theta\beta$$

A more exact treatment of the problem gives:

$$\delta = \frac{0.9\lambda}{\beta 1/2} Cos\theta\beta \tag{3.9}$$

This is known as Scherrer's formula. It is used to estimate the size of very small crystals from measured width of their diffraction curves. Note that whether a value of 0.9 or 1 is used depends on shapes of the crystallites assumed to be sample.

Determination of lattice parameters

For the wurtzite structure the interplanar distance of {hkl} plane is related to the lattice parameters *a* and *c* via the Miller indices *hkl*:

$$\frac{1}{dhkl} = \frac{4}{3}(\frac{h2+k2+hk}{a2}) + \frac{l2}{c2} \tag{3.10}$$

For the lattice parameters determination for a c-plane oriented sample includes a measurement of d_{001} in order to determine the *c* lattice parameter, and for the determination of a lattice from a second measurement of d_{hkl} with either *h* or *k* different from zero [7] For the wurtzite structure the interplanar distance of the (hkl) plane is related to the lattice parameters a and c via the miller indices hkl.

3.3.2 Scanning electron microscope (SEM)

The shape and morphology of particles are studied by Scanning Electron Microscope (SEM). SEM uses a focused beam of high-energy electrons to generate a variety of signals at the surface of solid specimens. The signals that derive from electron reveal information about the sample including external morphology (texture), chemical composition, and crystalline structure and orientation of materials making up the sample. The beam of electrons is produced and accelerated from an electron source and passed through a series of condenser and objective lenses, which focus the electron beam. A scanning coil moves the beam across the specimen surface. Accelerated electrons carry significant amounts of kinetic energy, and this energy is dissipated as a variety of signals produced by electron-sample interactions when the incident electrons are decelerated in the solid sample.

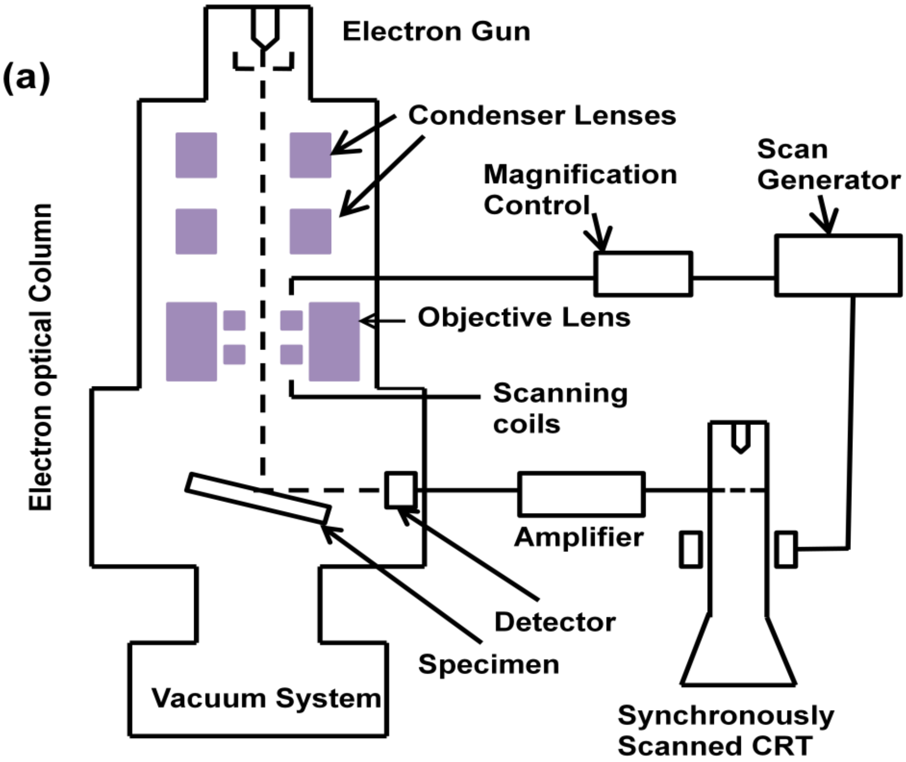

Figure 3.6 Schematic Diagram of SEM.

These signals include secondary electrons (that produce SEM images), backscattered electrons (BSE), diffracted backscattered electrons (EBSD that are used to determine crystal structures and orientations of minerals), photons (characteristic X-rays that are used for elemental analysis and continuum X-rays), visible light (cathodoluminescence-CL), and Secondary electrons and backscattered electrons are commonly used for imaging samples: secondary electrons are most valuable for showing morphology and topography on samples and backscattered electrons are most valuable for illustrating contrasts in composition in multiphase samples [8].

Depending on the specimen and the equipment setup, the contrast in the final image provides information on the specimen composition, topography and morphology. In this study, a SHIMADZU SSX-550 Superscan SEM Model with EDS was used. In most applications, data are collected over a selected area of the surface of the sample, and a 2-dimensional image is generated that displays spatial variations in these properties. Areas ranging from approximately 1 cm to 5 microns in width can be imaged in a scanning mode using conventional SEM techniques (magnification ranging from 20X to approximately 30,000X, spatial resolution of 50 to 100 nm) [9]. The SEM is routinely used to generate high-resolution images of shapes of objects (SEI) and to show spatial variations in chemical compositions: 1) acquiring elemental maps or spot chemical analyses using EDS, 2) discrimination of phases based on mean atomic number (commonly related to relative density) using BSE, and 3) compositional maps based on differences in trace element "activitors" (typically transition metal and Rare Earth elements) using CL [10] It is also widely used to identify phases based on qualitative chemical analysis and/or crystalline structure. Precise measurement of very small features and objects down to 50 nm in size is also accomplished using the SEM.

3.3.3 Energy Dispersive x-ray Spectroscopy (EDS)

The surface chemical or elemental composition of the synthesized powders grown in this research study was determined by EDS spectroscopy. (EDS or EDX) is a chemical microanalysis technique used in conjunction with scanning electron microscopy (SEM). The EDS technique detects X-rays emitted from the sample during bombardment by an electron beam to characterize the elemental composition of the analyzed volume. Features or phases as small as 1 µm or less can be analyzed [11].

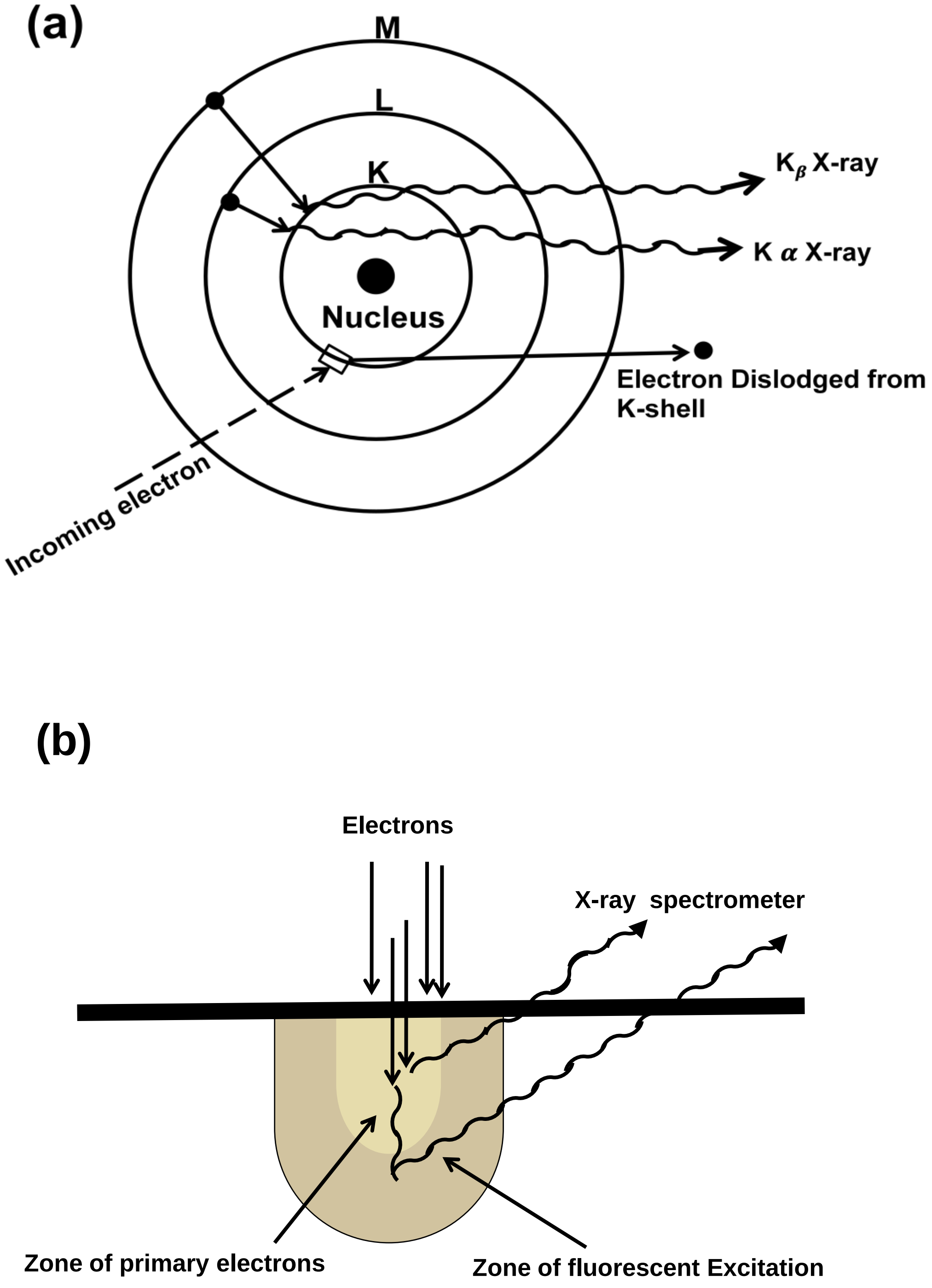

Figure 3.7 (a) and (b) Characteristic x-ray radiation [12]

Information about the chemical composition of the sample is obtained by measuring the intensity distribution and energy of the signal generated by a focussed electron beam impinging on the sample. The source of the electron is the electron gun of a scanning electron microscope. The incident beam of electrons interacts with core electrons of the sample's atoms transferring sufficient energy to it, thereby ejecting it from the target atom. This results in the creation of a hole within the atom's electronic structure. An electron from an outer, higher energy shell then occupies the hole releasing excess energy in the form of an X-ray photon. As a result of electronic transitions which occur between the outer and inner core levels a characteristic X-ray is emitted when the ionized atom 'relaxes' to a lower energy state by the transition of an outer-shell electron to the vacancy in the core shell which provide a quantitative and qualitative elemental composition of the sample [13]. Due to a well-defined nature of the various atomic energy levels, it is clear that the energies and associated wavelengths of the set of x-rays will have characteristic values for each of the atomic species present in a sample [13] as shown in Figure 3.7(a) and (b).

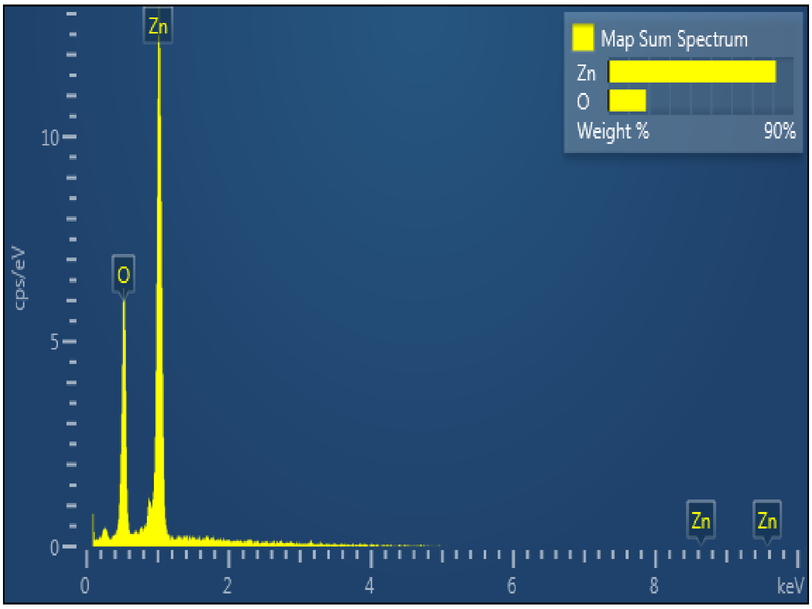

Figure 3.8 Example of an EDS spectrum of ZnO.

A characteristic X-ray is usually emitted when the ionized atom 'relaxes' to a lower energy state by the transition of an outer-shell electron to the vacancy in the core shell. The X-ray is called characteristic because its energy equals the energy difference between the two levels involved in the transition and this difference is characteristic of the material.

From the output of an EDS analysis we obtain an EDS spectrum, see Figure 3.8. The EDS spectrum shows the frequency in counts of X-rays received for each energy level. The spectrum normally plots the peaks corresponding to the energy levels for which the most X-rays have been received. Each of these peaks corresponds to a specific atom, and therefore characteristic of a specific element. The intensity of a peak in the spectrum correlates with the concentration of the element in the sample [14]

3.3.3 Photoluminescence (PL) Spectroscopy

Photoluminescence (PL) is a process in which a substance absorbs photons (electromagnetic radiation) and then re-radiates photons. Quantum mechanically, this can be described as an excitation to a higher energy state and then a return to a lower energy state accompanied by the emission of photon [14]**.** PL is a powerful and a relatively simple method, extensively used as characterization technique of semiconductor physics for a number of reasons [15, 16].

It is non-destructive because it is based on pure optical processes, no sample preparation is required and it is highly sensitive. Different types of samples (powder, liquid or bulk semiconducting material) can be characterized. PL is a convenient technique requiring a suitable source of optical excitation, a monochromator and a suitable detector for the emitted light. PL measurements are performed under continuous beam excitation conditions commonly known as continuous wave (CW) or steady state PL [17]. The sample is optically excited with laser energy greater than its band gap, Figure 3.9. The incident photons are absorbed under creation of electron-hole pairs in the sample. After a short time the electrons eventually recombine with the holes, to emit photons, and light or luminescence will emerge from the sample. The energy of the emitted photons reflects the energy carrier in the sample. The emitted luminescence is collected, and intensity is recorded as a function of the emitted photon energy or wavelength, to produce a PL spectrum.

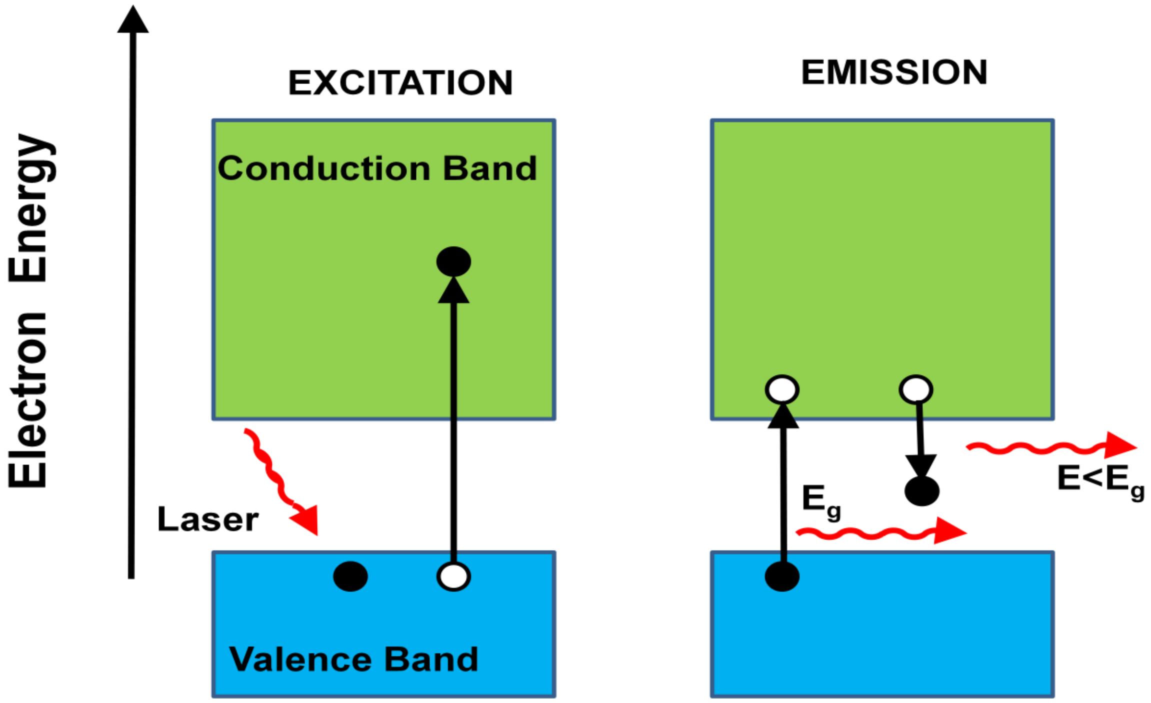

Figure 3.9 Excitation and Emission processes

The excitation energy is kept fixed, while the detection energy of PL is scanned. Luminescence measurements provide information both about the host semiconductor, through intrinsic optical processes; and about the wide variety of impurities or defects which are endemic in all real semiconductor materials, through extrinsic optical processes. It is particularly suited for the detection of shallow-level impurities, but can also be applied to certain deep-level impurities/defects, provided that their recombination is radiative [18].

Detailed information on electronic structure in the semiconductor that can be deduced from PL study includes the size of the band gap, impurity levels, interface, and surface properties as well as density of states and excitonic states. PL technique is particularly helpful in the analysis of discrete defect and impurity states. To gain more knowledge about the electronic structure, magnetic and electric fields can be applied in a controlled manner. Moreover external forces can be used in PL investigations, e.g. the strain by exposing the material to mechanical pressure. Since PL relies on radiative recombination, so it is very difficult for the investigation of non-radiative processes needs indirect methods, and the material having poor quality are hard to characterize through PL.

In a PL system the sample is excited with a monochromatized lamp or a higher laser beam, which is followed by the excitation during electron transition to higher energy levels and emission of photons during transition to the ground state [19].

The PL data was collected using the Cary Eclipse Spectrophotometer (Figure 3.10). The Cary Eclipse Spectrophotometer uses a Xenon flash lamp (60-75W) for superior sensitivity, high signal-to-noise and fast kinetics. It measures the Emission of light from samples in four modes. Using Xenon Lamp technology, it captures a data point in every 12.5 ms and scans at 24 000 nm/min without peak shifts. The Cary Eclipse is the only spectrophotometer with room light immunity.

Figure 3.10 the Cary Eclipse Fluorescence Spectrophotometer at the University of the Free State, Physics Dpt.

3.3.4 UV-Visible Spectroscopy

An instrument used in the ultraviolet-visible spectroscopy is called UV/Vis spectrophotometer. The wavelength of UV is shorter than the visible light. It ranges from 100 to 400 nm. In a standard UV-V is spectrophotometer, a beam of light is split; one half of the beam (the sample beam) is directed through a transparent cell containing a solution of the compound being analysed, and one half (the reference beam) is directed through an identical cell that does not contain the compound but contains the solvent. The instrument is designed so that it can make a comparison of the intensities of the two beams as it scans over the desired region of the wavelengths. If the compound absorbs light at a particular wavelength, the intensity of the sample beam (IS*)* will be less than that of the reference beam [20]. Absorption of radiation by a sample is measured at various wavelengths and plotted by a recorder to give the spectrum which is a plot of the wavelength of the entire region versus the absorption (A) of light at each wavelength**.** And the band gap of the sample can be obtained by plotting the graph between (αhν vs hν) and extrapolating it along x-axis**.** Ultraviolet and visible spectrometry is almost entirely used for quantitative analysis; that is, the estimation of the amount of a compound known to be present in the sample. The sample is usually examined in solution. The Uv-Vis system shown in Figure 3.11 was used in this research.

Figure 3.11 Perkin Elmer lamb 950 UV-VIS Spectrometer at the University of the Free State, Physics Department.

RD is the science of determining the arrangement of the atoms within a crystal from the manner in which a beam of X-rays is scattered from the electrons within the crystal. Up to 1895 the study of matter at the atomic level was a difficult task but the discovery of electromagnetic radiation with 1 Å (10^{-10} m) wavelength, appearing at the region between gamma-rays and ultraviolet, makes it possible. As the atomic distance in matter is comparable.

3.3.5 Fourier Transform Infrared Spectroscopy (FTIR)

In the region of longer wavelength or low frequency the identification of different types of chemicals is possible by this technique of infrared spectroscopy and the instrument required for its execution is FTIR spectrometer. The spectroscopy merely based on the fact that molecules absorb specific frequencies that are characteristic of their structure termed as resonant frequencies, i.e. the frequency of the absorbed radiation matches the frequency of the bond or group that vibrates. And the detection of energy is done on the basis of shape of the molecular potential energy surfaces, the masses of the atoms, and the associated vibronic coupling. Sometimes help of approximation techniques like Born–Oppenheimer and harmonic approximations are also taken. As each different material is a unique combination of atoms, no two compounds produce the exact same infrared spectrum. Therefore, infrared spectroscopy can result in a positive identification (qualitative analysis) of every different kind of material. In addition, the size of the peaks in the spectrum is a direct indication of the amount of material present. FTIR can be used to analyze a wide range of materials in bulk or thin films, liquids, solids, pastes, powders, fibers, and other forms. FTIR analysis can give not only qualitative (identification) analysis of materials, but with relevant standards, can be used for quantitative (amount) analysis. FTIR can be used to analyze samples up to ~11 millimeters in diameter, and either measure in bulk or the top ~1 micrometer layer. FTIR spectra of pure compounds are generally so unique that they are like a molecular "fingerprint". In this study we have used PerkinElmer Spectrum 100 FTIR Spectrometer shown in Figure 3.12.

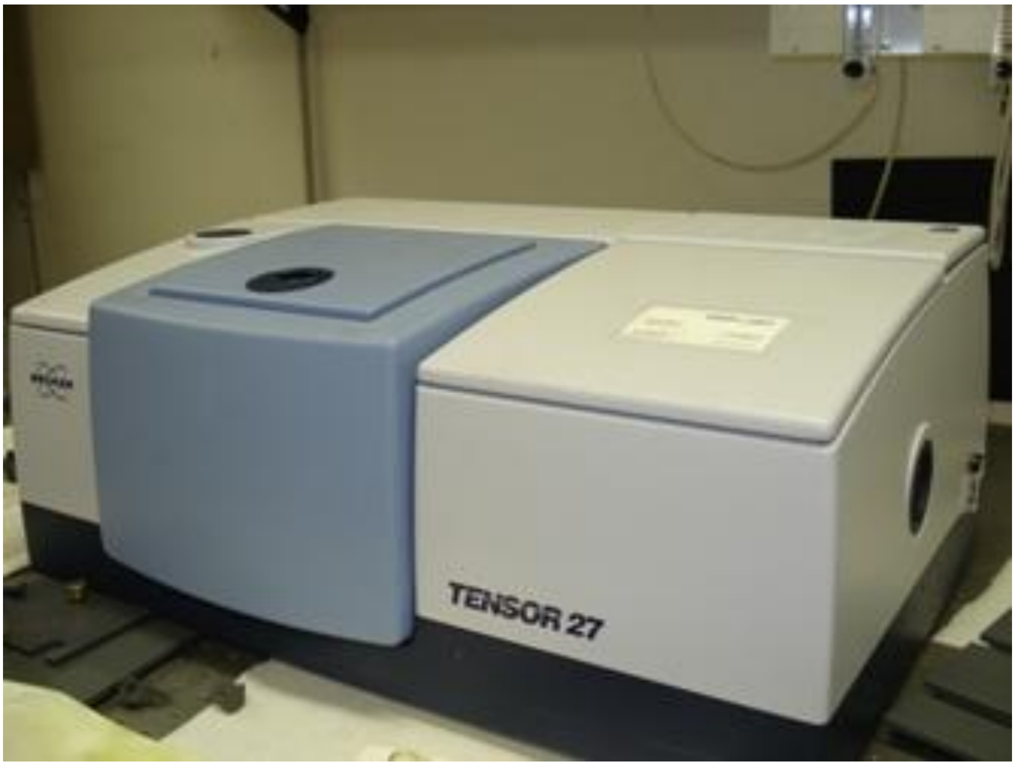

Figure 3.12 FTIR systems at UFS Chemistry Department.

3.3.6 Thermal Analysis

1. Differential scanning calorimetry (DSC)

2. Thermal gravimetric analysis (TGA)

Differential Scanning Calorimetry (DSC)

Thermal Analysis (STA) generally refers to the simultaneous application of Thermogravimetry (TGA) and Differential scanning calorimetry (DSC) to one and the same sample in a single instrument. The test conditions are perfectly identical for the TGA and DSC signals (same atmosphere, gas flow rate, vapour pressure of the sample, heating rate, thermal contact to the sample crucible and sensor, radiation effect, etc.).Thus, Thermal analysis (TA) is a group of techniques in which changes of physical or chemical properties of the sample are monitored against time or temperature, while the temperature of the sample is programmed which may involve heating or cooling at a fixed rate, holding the temperature constant (isothermal), or any sequence of these.

Working of DSC

The sample and reference chambers are heated equally into a temperature regime in which a transformation takes place within the sample. As the sample temperature deviates from the reference temperature, the device detects it and reduces the heat input to one cell while adding heat to the other, so as to maintain a zero temperature difference between the sample and reference. The quantity of electrical energy per unit time which must be supplied to the heating element in order to maintain null balance is assumed to be proportional to the heat released per unit time by the sample.

Working of TGA

Measurements of changes in sample mass with temperature can be made using a thermo balance. This is a combination of a suitable electronic microbalance with a furnace and associated temperature programmer. The balance should be in an enclosed system so that the atmosphere can be controlled. Y axis is % mass loss; X axis is temp (or time, since usually a linear heating rate). As the specimen changes weight, its tendency to rise or fall is detected by LVDT. A current through the coil on the counterbalance side exerts a force on the magnetic core which acts to return the balance pan to a null position. The current required to maintain this position is considered proportional to the mass change of the specimen. PerkinElmer STA 6000 Simultaneous Thermal Analyzer was used in this research.

References

[1] Seema R ,Poonam Si, Shishodia P.K , Mehra R.M 2008 *J. Mater. Sci.* 921639–1645.

[2] Mohanta S. K, Kim D. C, Kong B. H, Cho H. K, Liu W, Tripathy S 2010 *Sci. Adv. Mater.*,2 64.

[3] Yongfa Zhu, Zhang L.I, Chong Gao, Lili 2000 *J. Mater. Sci.*, 354049–4054.

[4] Rizwan Wahab, Ansari S.G, Young-Soon Kim, Hyung-Kee Seo, Hyung-Shik Shin 2007 *Appl.Surf. Sci.*, 253 622–7626.

[5] Cullity B.D. , Stock S.R "Element of x-ray diffraction" *3rd edition, Practice-Hall Inc. New Jersy.*

[6] X-Ray Diffraction, [online]. Available from, http://www.doitpoms.ac.uk/tlplib/index.php [Accessed 10 January 2015].

[7] Vanya Darakchieva "Strain-related structural and vibrational properties of group-III Nitride.

[8] Hawkes P. W , Spence J. C. H 2007 Science of Microscopy *New York, USA: Springer*, vol. 1.

[9] http://en.wikipedia.org/wiki/Scanning_electron_microscope.

[10] Berman P.R 1997 "advanced in atomic, molecular and optical physics"*Academic press, Amsterdam,* Vol.45.

[11] Description of EDS Technique http://mee-inc.com/index.html [Accessed 03/10/2011].

[12] Energy Dispersive X-ray Spectroscopy (EDS/EDX), [online]. Available from http://www.thermo.com/com/cda/technology/detail/1,,12700,00.html [Accessed 1 May 2011].

[13] B. G. Yacobi, D. B. Holt, and L.L. Kazmerski Microanalysis of Solids, New York, Plenum Press, 1994.

[14] EDS online].Available from http://ion.eas.asu.edu/descript_eds.htm [Accessed 17 May 2011].

[15] Sardela M.R Jr. 2000 'The growth, thermal stability, structural and electrical properties of doped and undoped Si-based epitaxial structures" PhD thesis Linköping university Press, Dissertation No.341.

[16] Barron A. R 2012 "Photoluminescence and Fluorescence Spectroscopy," in Physical Methods in Chemistry and Nano Science. Rice University, Houston, Texas: *C O N N EX IO N S,* p.295.

[17] Photoluminescence [0nline], Available from http://www.purdue.edu/REM/rs/sem.htm 2008.[Accessed 8 Aug. 2014].

[18] Nguyen Q, 2004 Thin "optically detected magnetic resonance studies of intrinsic defects in dilute" PhD thesis linköping university Dissertation No.901.

[19] Patterson A. L 1939"The Scherrer Formula for I-Ray Particle Size Determination," *J. Phys. ev. B,* vol. 56, p. 978.

[20] Mbule P.S, Msc Thesis, University of the Free State, Republic of South Africa, 2009.

Chapter 4

Effect of growth temperature on structural and luminescence properties of ZnO nanoparticles

4.1. Introduction

Zinc oxide (ZnO), a wide band gap (3.4 eV) II-VI compound semiconductor, has a stable wurtzite structure with lattice spacing a = 0.325 nm and c = 0.521 nm. It has attracted intensive research effort for its unique properties and versatile applications in transparent electronics, ultraviolet (UV) light emitters, piezoelectric devices, chemical sensors and spin electronics [1-5]. It is well documented that the shape and size of the material strongly affect the properties and the applications of the materials. Hence much effort is dedicated on controlling the size and shape of the particles by varying different growth parameters such as time, temperature, concentration, precursors, capping molecule, solvents, and others [6]. Growth temperature is a key factor in controlling the morphology, optical and electrical properties of nanostructures. Guo *et al* [7] discussed how the effect of growth temperature and concentration can be explained in terms of collision theory. When two chemicals react, the molecules have to collide with each other with sufficient energy to cause reaction. Optimization of growth temperature is therefore a key procedure to obtain high quality ZnO nanostructures. In view of this, in the present work we have undertaken the synthesis of the ZnO nanoparticles by sol gel method and carried out a systematic analysis of the effects of growth temperature on the structural and luminescence properties of the nanoparticles.

4.2. Experimental Procedure

ZnO nanostructures were prepared from aqueous solutions of zinc acetate dehydrate (Zn(CH3COO)2·2H2O) and sodium hydroxide (NaOH). In the three-neck glass flask, zinc acetate dehydrate was dissolved in ethanol to a concentration of 0.2 M and the resulting solution was heated, under constant stirring, to different growth temperatures (room temperature (RT), 35, 45, 55, 65 and 75 °C). After achieving a desired temperature of growth, a solution of NaOH was added slowly (dripped for 60 minutes) into the three-neck glass flask containing the (Zn(CH3COO)2·2H2O), aqueous solution under continual stirring. In this procedure the desired reaction temperature was constantly maintained. The suspension formed with the dropping of 0.8 M alkaline aqueous solution to zinc acetate dehydrate solution was kept stirred for two hours at the same growth temperature and allowed to stand for some time till gel like solution was formed. The material was then filtered and washed several times with deionized water. The washed sample was dried at 60 °C in oven for one hour and one portion of it annealed at 600 °C for 1 hour. The yield of the ZnO nanostructures by this method is about 95%.The crystallite size, morphology, structural and luminescent properties of the as-synthesized particles were examined by means of scanning electron microscopy (SEM), X-ray diffraction (XRD), UV-Vis spectroscopy, photoluminescence spectroscopy (PL), thermo gravimetric analyzer (TGA) and fourier transformed infrared spectroscopy (FTIR).

4.3 Results and Discussion

4.3.1 Structural and Compositional analysis

The results of X-ray diffraction for increasing growth temperatures are shown in Figure 4.1(a).

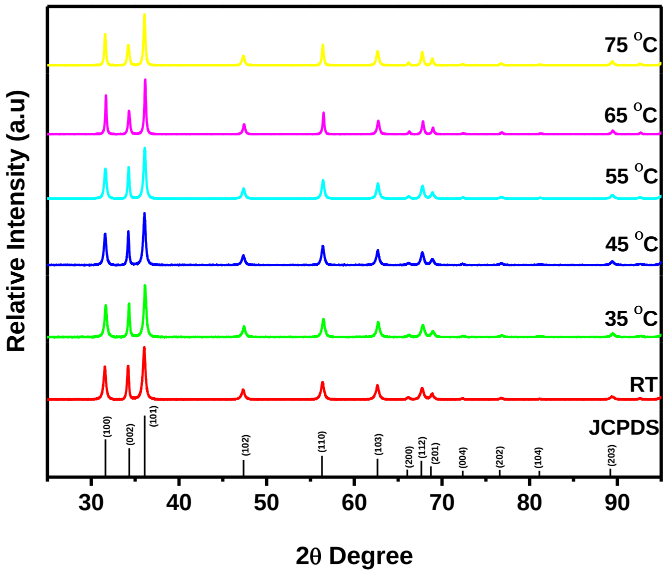

Figure 4.1(a) X- ray powder diffraction pattern for ZnO nanoparticles prepared at different growth temperature.

The XRD spectra shows typical hexagonal wurtzite structure of ZnO with respect to standard card (JCPDS No. 79-0208). The crystallite sizes of ZnO were calculated using the Scherer's formula [8].

$$D = \frac{0.9\,\lambda}{\beta\ \cos\theta_B} \qquad (1)$$

where λ, θ and β are the X-ray wavelength (1.54056 Å), Bragg's diffraction angle and line width at half maximum of the ZnO (101) diffraction peak, respectively.

The crystallite size of the ZnO nanoparticles increased from 27.6 to 34.2 nm with an increase in growth temperature from 35 to 75 °C. It was observed that the XRD peak broadening decreases while the intensity increases confirming an improved crystal quality with increased growth temperature [9]. Expansion of the lattice due to increased growth temperature is responsible for increase in lattice parameters ‘a’ and ‘c’ determined [10]. The lattice parameter *'a'* and crystallite size as a function of temperature are shown in Figure 4.1(b). P. Singh *et al* [12] also observed that there is a continuous increase in lattice parameter and particle size with temperature.

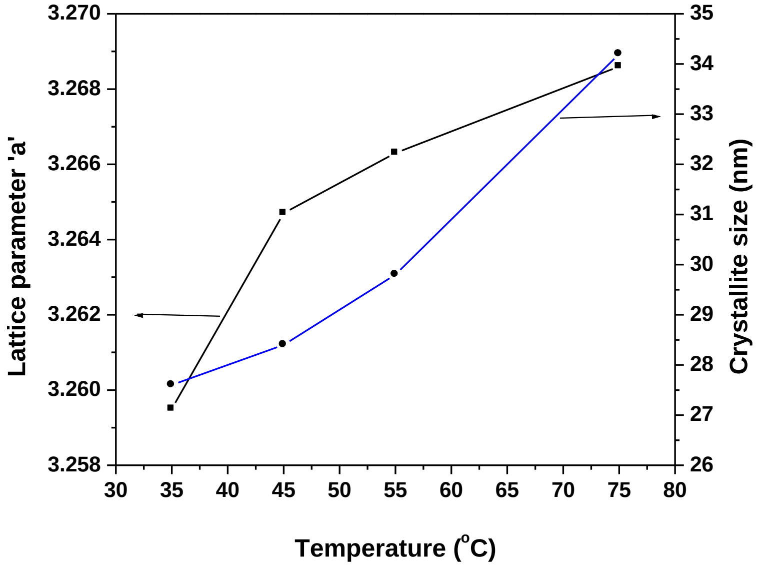

Figure 4.1(b) lattice parameter 'a' and particle size as a function of temperature.

Table 4.1 Different measured properties of ZnO nanoparticles.

Temperature (°C)	Crystallite size (nm)	Lattice Constants			Positional parameter, *u*	Zn-O Bond length, *L*
		a (Å)	*c* (Å)	Ratio, *c/a*		
35	27.6	3.2595	5.2283	1.60402	0.37955	1.9844
45	28.4	3.2655	5.2379	1.60401	0.37956	1.9880
55	29.8	3.2663	5.2319	1.60178	0.37992	1.9879
75	34.2	3.2686	5.2343	1.60138	0.37998	1.9889

Table 4.1 shows how crystallite sizes, lattice parameters, ratios of lattice constant *c/a*, positional parameters *u* and Zn-O bond lengths (L) vary with changes in growth temperature. The increase of the lattice parameter of ZnO nanoparticles with increase in temperature was calculated using the relation below, in the case of ZnO hexagonal structure [12].

$$\frac{1}{d^2_{(hkl)}} = \frac{4}{3}\left(\frac{h^2 + hk + k^2}{a^2}\right) + \frac{l^2}{C^2} \qquad (2)$$

Where d is the spacing between planes of Miller indices h, k, and l, a and c are the lattice parameters.

The lattice constants a for $\langle 100 \rangle$ plane is calculated by

$$a = \frac{\lambda}{\sqrt{3}\sin\theta} \qquad (3)$$

For the $\langle 101 \rangle$ plane, the lattice constant c is calculated by substituting the value of a in equation (2) to obtain,

$$sin^2\theta = \frac{\lambda^2}{4}\left[\frac{4}{3}\left(\frac{h^2+hk+k^2}{a^2}\right) + \frac{l^2}{c^2}\right] \qquad (4)$$

Since, from the Bragg's law:

$$n\lambda = 2d\,\mathrm{Sin}\theta \qquad (5)$$

and with the first-order approximation $n = 1$.

Thus, Zn-O bond length L can be calculated using the equation that follows [13].

$$\mathrm{L} = \sqrt{\left(\frac{a^2}{3} + \left(\frac{1}{2} - u\right)^2 c^2\right)} \qquad (6)$$

Where u is the positional parameter in the wurtzite structure and is a measure of the amount by which each atom is displaced respect to the next along the *'c'* axis. *'u'* is given by

$$u = \frac{a^2}{3c^2} + 0.25 \qquad (7)$$

The Zn-O bond lengths calculated for various growth temperatures are summarized in Table 4.1. Continuous increases in bond lengths with increase in growth temperatures are observed. The average calculated bond length is 1.9873 which is just slightly greater than the reported Zn-O bond length in the unit cell of ZnO and neighboring atoms of 1.9767 Å [14]. The calculated bond length agrees with the Zn-O bond length in the unit cell.

The c/a ratio is observed to decreases with the increase in *u* in such a way that the four tetrahedral distances of Zno remain nearly constant through a distortion of tetrahedral angles [15]. The average ratio of lattice parameters *c/a* is approximately 1.603 which is slightly less than that of pure ZnO (1.604). The interplanar spacing has been increased due to small shift in 2θ due to increase in growth temperature.

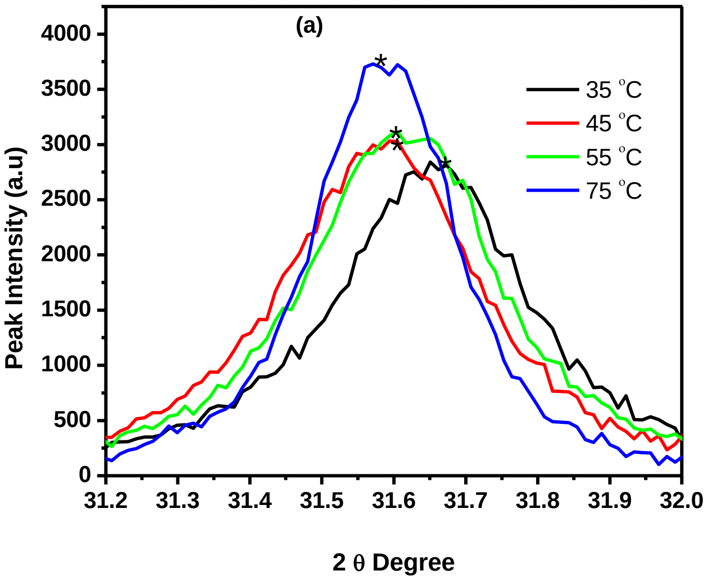

Figure 4.1(c) Comparison of changes in peak (100) intensity and positions for various growth temperatures.

Figure 4.1(c) shows how the peak intensity of the particles increased continuously with the increase in growth temperature and as width of the peaks gets narrower. Maximum emission intensity was observed for growth temperature of 75 °C while maximum peak width at 35 °C. As the particle becomes thicker, the crystalline quality is improved and preferred orientation of the grain enhanced. The decrease of the FWHM with increasing growth temperature could be due to the coalescences of grains at higher temperatures leading to increase in the average crystallite size. According to Ostwald ripening, the increase in the particle size is due to the merging of the smaller particles into larger ones as suggested by

Nanda *et al* [16] and is a result of potential energy difference between small and large particles and can occur through solid state diffusion.

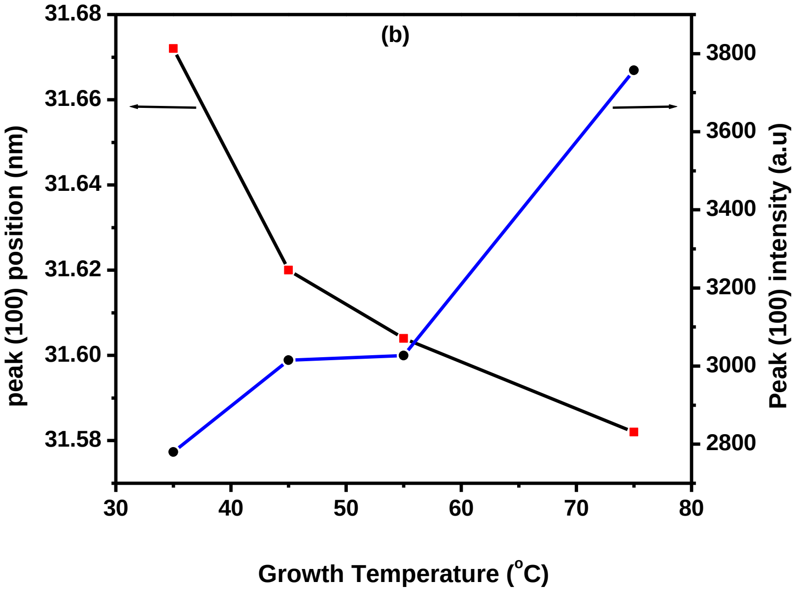

Figure 4.1(d) graph of shift in peak (100) position and relative intensity as a function of temperature.

The peak positions of the XRD spectra shift slightly to lower 2θ angle with increasing growth temperature; this is demonstrated by peak (100) position shift from 31.672 to 31.582 for growth temperatures 75 to 35 °C respectively as shown in Figure 4.1(d). This means that a small variation in the lattice parameters occurs as growth temperature is increased. The length of both lattices *a* and *c* axis expand slightly with increasing temperature which can be attributed to the change in the stress in nanoparticles.

4.3.2 Thermal Gravimetric Analysis (TGA)

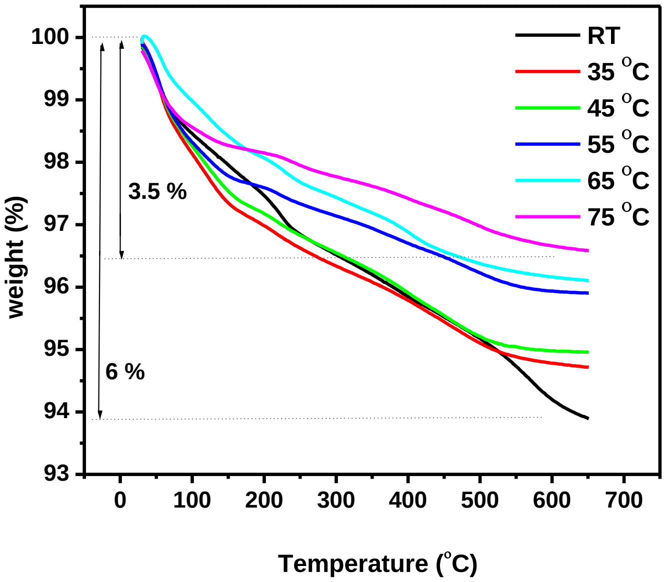

Figure 4.2 TGA curves of ZnO nanoparticles grown at different growth temperature.

The TGA graph is shown in Figure 4.2. Since the samples were prepared using ethanol solvent the materials contain traces of ethanol. Peaks observed around 57 °C represent the mass loss due to evaporation of ethanol. The decrease of mass observed at 170 °C could be due to decompositions of $Zn(OH)_2$ which liberate water molecules.

Further 5 % mass loss was observed at approximately 600 °C due to the evaporation of water of crystallization. These results were in good agreement with the literature [17]. The crystallization occurs during the removal of water molecules. There are curves each from a different temperature gradient. More sample residue was observed due to gradual drop in % weight at high temperatures (75, 65 and 55 °C) resulting to 3.5 % weight loss. However, at low temperatures (RT, 35, and 45 °C), a slightly steeper drop in % weight was observed, leading to about 6 % loss in weight.

4.3.3 Surface morphological analysis

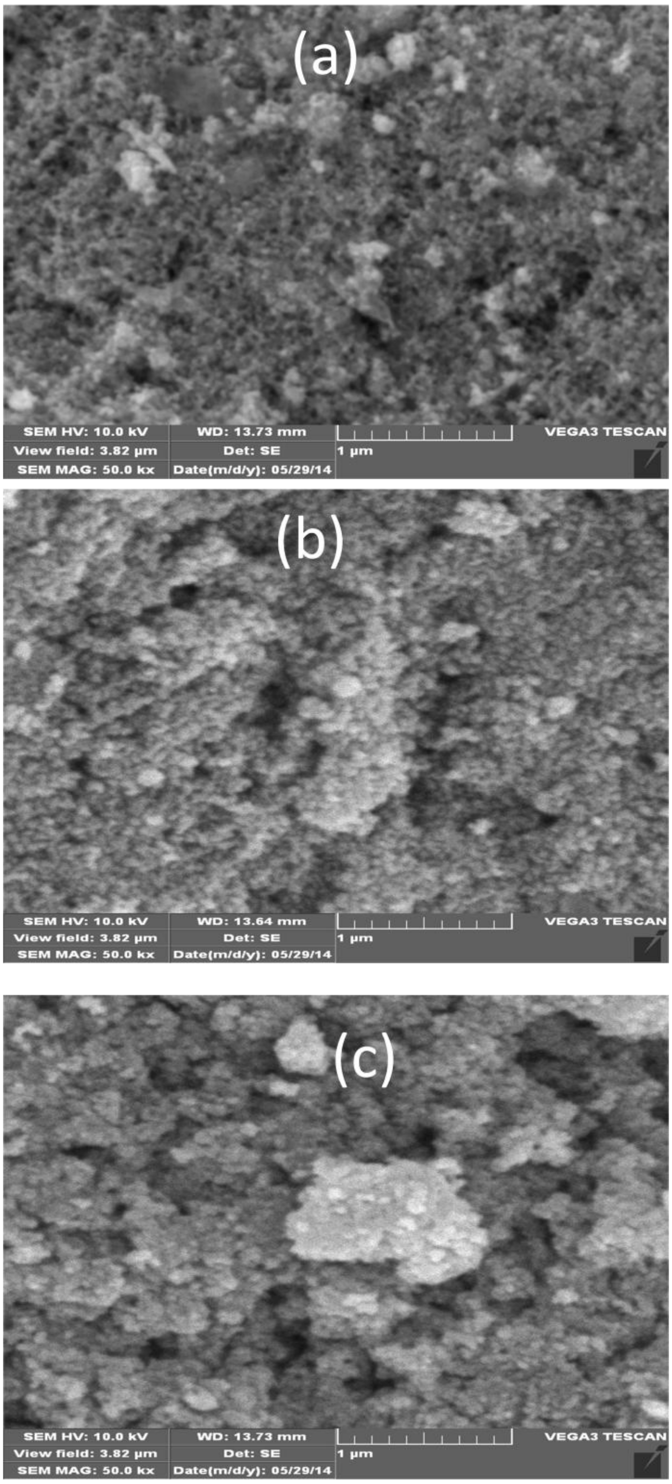

Figure 4.3 SEM micrographs of ZnO nanoparticles synthesized at (a) 35 °C, (b) 55 °C and (c) 75 °C

From Figures 4.3(a) – (c), SEM results show increased ZnO nanoparticle sizes with increase in growth temperature. The same result was also observed by other researchers. It is possible that the growth of ZnO nanostructures occurs in a diffusion –controlled regime. In this case, the diffusion of ad atoms on nanoparticle surface becomes smooth and faster with increasing temperature. Accordingly, at higher temperature, more ad atoms will be diffused to the tips, which are energetically favorable sites, instead of being remained on the side surface of nanoparticles [18]. Spherical particles are formed at higher growth temperatures (Figures 4.3b and c); while at lower temperature, Figures 4.3(a), needle like rods particles were observed.

4.3.4 Photoluminescence Analysis

Figure 4.4(a) depicts PL emission spectra for ZnO nanoparticles prepared at different growth temperatures. The spectra display emissions centered at 391and 546 nm (at excitation of 281 nm), representing UV and Visible emissions respectively, but with varied relative intensity and exact location of the emission peaks. The UV luminescence peak corresponds to the near band-edge emission and is commonly attributed to the recombination of excitons while the green emission peak is due to a deep level or trap-state emission corresponding to the singly ionized oxygen vacancy in ZnO (oxygen related defects) resulting from recombination of a photon generated hole with the single ionized charged state of this defect.

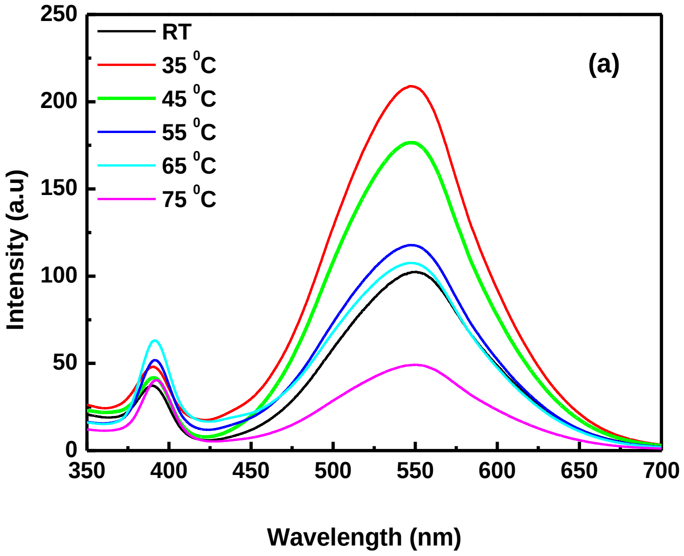

Figure 4.4(a) PL emission spectrum for ZnO nanoparticles prepared at different growth temperatures.

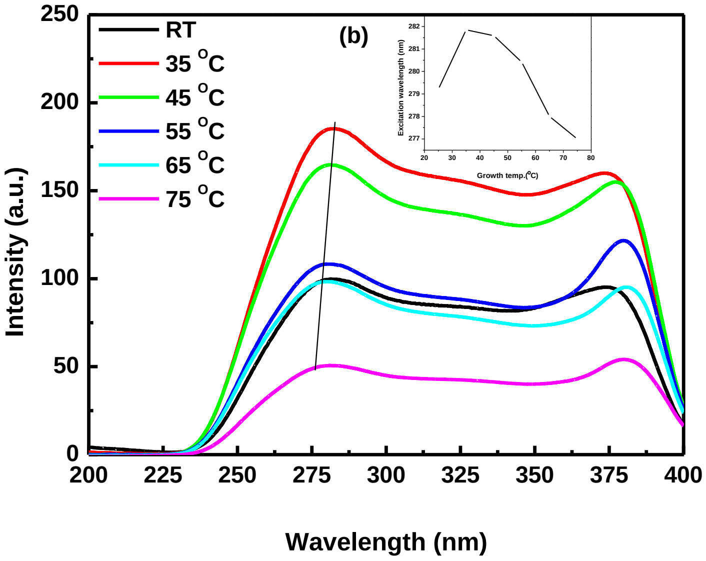

Figure 4.4(b) PL excitation spectrum for ZnO nanoparticles prepared at different growth temperatures (Inset: change in peak position of excitation wavelength with increase in growth temperatures).

Figure 4.4(b) shows PL excitation spectra. The inset depicts a shift to lower excitation wavelength of peak 281, as the growth temperature increases. However, the excitation peaks at larger wavelengths shifted from 375 to 382 nm with the increase in growth temperature.

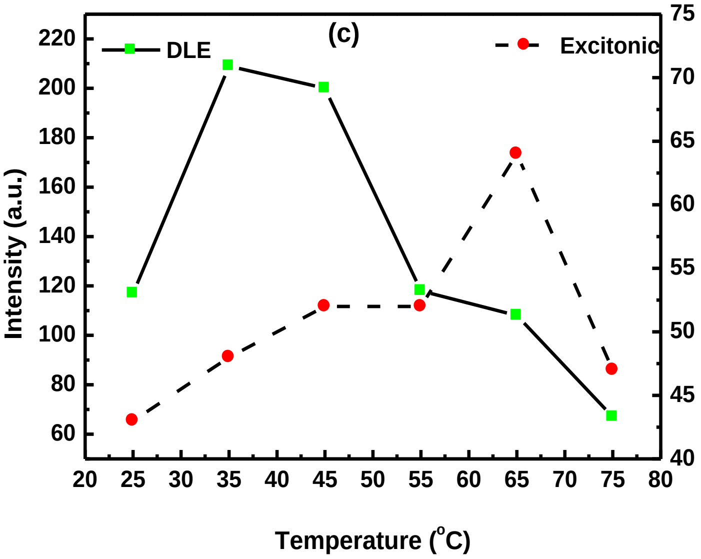

Figure 4.4(c) comparison of the intensities of deep level emission (DLE) and excitonic peak emission with respect to change in growth temperature.

Figure 4.4(c) displays clear reduction in defect density with increase in growth temperature as shown by continuous increase in excitonic peak intensity and decrease in visible emission peak intensities which also insinuates increase in crystallinity as a result of increase in temperature. This increase in luminescence intensity can be due to slightly increased crystallite sizes as the synthesis temperature rises, thus increasing non-radiative recombination. The decrease in DLE is attributed to the larger surface-to-volume ratio of thinner nanoparticles favoring a higher level of defects and surface recombination [19].

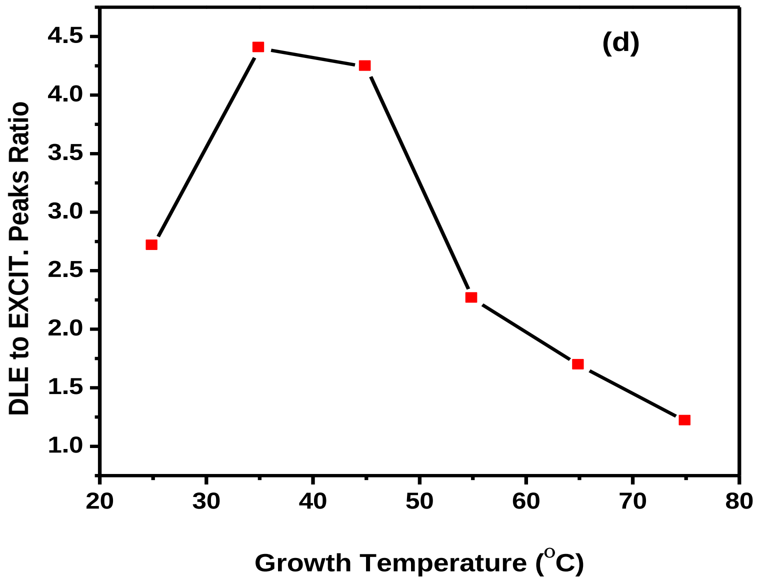

Figure 4.4(d) DLE to Excitonic peak Intensity change with growth temperature

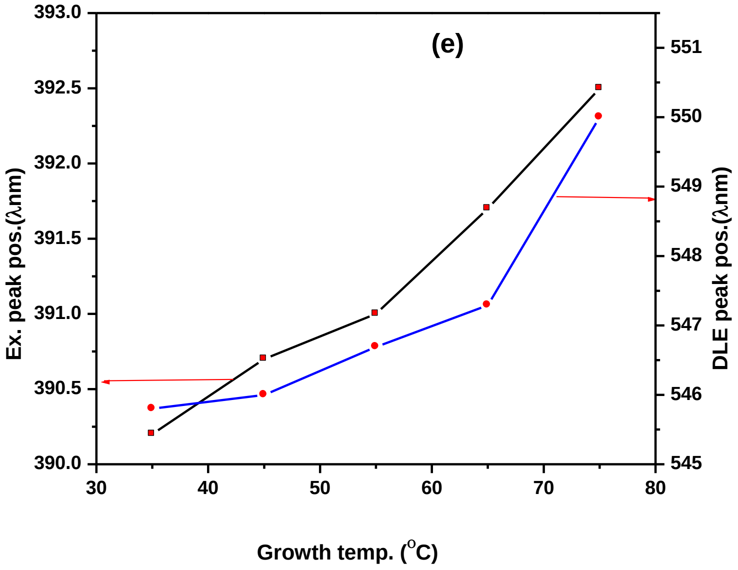

Figure 4.4(e) Excitonic and DLE peaks position dependence on temperature.

Figure 4.4(d) demonstrates how the ratio of relative intensity of the green to UV emission is reduced with the increase of growth temperature contrary to report by Kim et al (20), who indicated that the ratio increases with the growth temperatures. A detailed investigation will be carried out soon to verify the trend.

The peak positions and intensities are both affected by growth temperatures. Peaks shift somewhat to longer wavelengths (about 392/547 nm) at high growth temperature compared to that of 389/545 nm for lower temperatures as illustrated in Figure 4.4(e). The red shift in the visible emission and UV emission with increasing particle size closely follows the red shift in the band edge emission, indicating that they are related. This shift of band edge emission was believed to originate from the changes in tensile stress because of lattice distortion. Since, the lattice reorganization is related to the electron hole density and because quantum confinement enhances the density, the shift will be enhanced substantially.

4.3.5 Optical properties

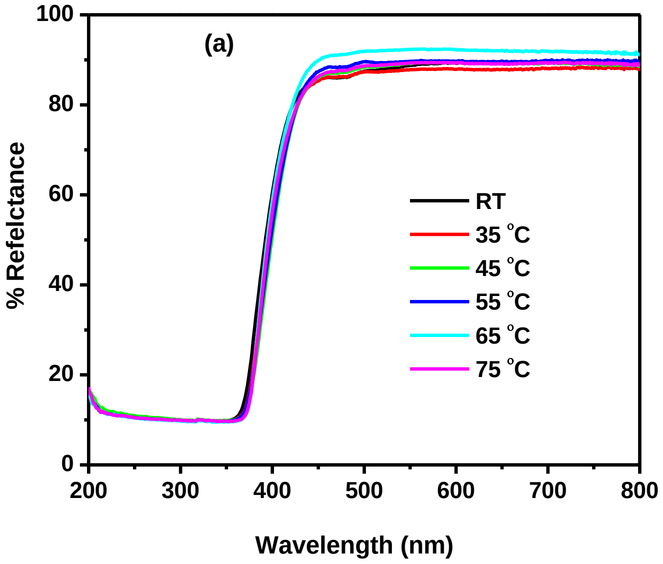

Figure 4.5(a) The reflectance spectra of ZnO nanoparticles prepared at various temperature.

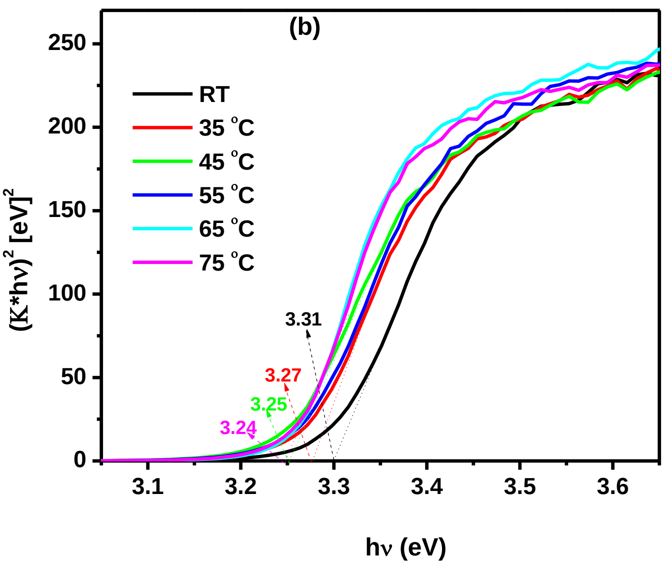

Figure 4.5(b) Plot to determine the band gap energy of ZnO nanoparticles prepared at various temperatures.

A sharp band edge is observed at approximately 385 nm. As displayed by Figure 4.5(a) which can be due to the intrinsic band gap absorption of ZnO due to the electrons transitions from the Valence Band to the Conduction Band.

The onset of band edge absorption has been found to be blue shifted with decreasing particle size confirming the size dependent absorption properties of ZnO nanoparticles. The band gap energy of ZnO was estimated using Kubelka-Munk remission function [21], for direct transitions. The estimated band gap reduced from 3.31 to 3.24 eV with the increase in the growth temperature as shown in Figure 4.5(b). Liao et al [22] reported that the band gap for ZnO decreased due to tensile strain while compressive strain results into an increase of the band gap. A compressed lattice is expected to provide a wide band gap because of the increased repulsion between oxygen 2p and Zinc 4s bands. The estimated band gap is; however, lower than that of the bulk ZnO (3.37ev). This band gap reduction may be due to surface defects density of undoped ZnO [23]. The variation in slope of different energy curve could be attributed to the non-uniformity in particle sizes as confirmed by SEM analysis.

4.3.6 Fourier Transform Infrared Spectroscopy (FTIR)

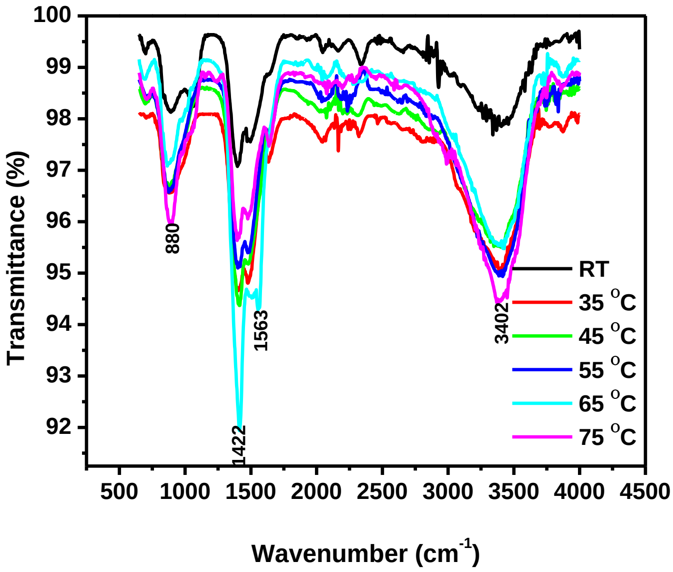

Figure 4.6(a) FTIR spectra of ZnO nanoparticles prepared at various growth temperatures.

FTIR presented in Figure 4.6(a), was performed to study the absorbance properties of ZnO nanoparticles prepared in varying growth temperatures and hence to deduce the nature of bonds present in the samples.

In the given profile on wave number axis, the absorbance peaks around 3,400 cm^{-1} are the peaks representing the hydroxyl (-OH) groups, which show incomplete removal of organic solvent. The next absorbance peak at wave number approximately 1,500 cm^{-1} is due to the absorbance of organic group carbon (carbonyl carbon -C=O). The absorbance at wave number approximately 880 cm $^{-1}$ is due to the typical bond between zinc and oxygen (Zn-O) [24-26]. The spectra show minimal % absorbance by the samples(less than 10%) which insinuate high purity as supported by XRD results. However, more organic solvent presence is observed at high growth temperature indicating existence of more impurity compared to lower growth temperature.

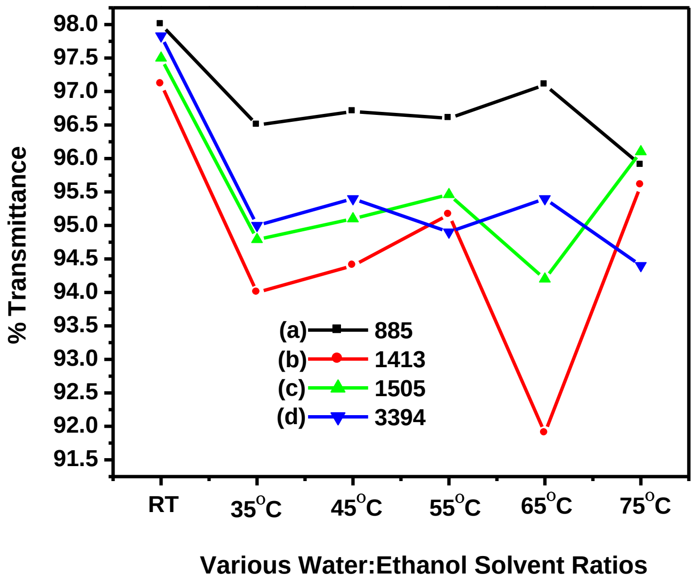

Figure 4.6(b) Graph of comparison of % Transmittance at various absorbance wave numbers (885, 1413, 1505 and 3394 cm $^{-1}$) against different growth temperatures of ZnO.

Figure 4.6(b) illustrates the highest % transmittance at all wave numbers to be at room temperature. The trend of % transmittance of ZnO nanoparticles, generally, declines with the increase in growth temperature.

Conclusion

ZnO nanoparticles with hexagonal wurtzite structure were synthesized successfully by sol-gel method. The effect of growth temperature on the structure, grain size, band gap and PL were investigated. As growth temperature increases from RT to 75 °C crystallite grain sizes increase correspondingly. SEM results show increased ZnO nanoparticle sizes with increase in growth temperature. The band gap emission from PL measurement showed an index of good crystal quality. Increased growth temperature significantly quenches the green emission and the peak positions and intensities are both affected by growth temperatures. The estimated band gap reduced from 3.31 to 3.24 eV with the increase in the growth temperature due to tensile strain while compressive strain results into an increase of the band gap. The band gap from reflectance curve; however, is lower than that of the bulk ZnO (3.37 eV). This band gap reduction may be due to surface defects density of undoped ZnO. FTIR measurement illustrates the highest % transmittance at all wave numbers to be at room temperature. The trend of % transmittance of ZnO nanoparticles, generally, declines with the increase in growth temperature.

References

[1] Nomura K, Ohta H, Ueda K, Kamiya T, Hirano M , Hosono H 2003 Science 300, 1269.

[2] Nakada T, Hirabayashi Y, Tokado T, Ohmori D , Mise T 2004 Sol. Energy 77, 739.

[3] Lee S.Y, Shim E.S, Kang H.S, Pang S , Kang J.S 2005 Thin Solid Films 437, 31.

[4] Könenkamp R, Word R.C, Schlegel C 2004 Appl. Phys. Lett. 85, 6004.

[5] Mckinstry S.T, Muralt P. 2004 J. Electroceram. 12, 7.

[6] Jun Y.W, Choi J.S, Cheon J 2006 Angewandte, Chemie-International Edition, vol.45 no. 21, 3414-3439.

[7] Guo M, Diao P, Wang X , Cai S 2005 Journal of Solid State Chemistry, vol. 178, 3210–3215.

[8] Wagner R.S , Doherty C 1996 J. Electroceram. Soc. 113 1300 3 4596.

[9] Vinod Kumar, Neetu Singh, Kapoor A, Ntwaeaborwa O M, H. C. Swart 2011 Matter. Res. Bull.48.

[10] Banerjee R, Sperling E A, Thompson G B, Fraser H L, Bose S, Ayyub P 2003 Appl. Phys. Lett. 82 4250.

[11] Singh P, Kumar A, Kaushal A, Kaur D, Pandey A, Goyal R 2008 Mater. Sci. 31 573-577.

[12] Cullity, B.D, Stock S.R 2001 Elements of X-ray diffraction, 3rd edn. Prentice Hall, New Jersey.

[13] Barret C.S, Massaski T.B 1980 Structure of Metals Pergamon Press, Oxford.

[14] Seetawan U, Jugsujinda S, Seetawan T, Ratchasin A, Euvananont C, Thanachayanont C, Chainaronk P 2011 Maters. Sci. Appls. 2, 1302-1306.

[15] Bindu P, Sabu T 2014 J Theor Appl Phys 8: 123-134.

[16] Nanda K K,, Kruis F E, Fissan H 2002 Phys. Rev. Lett. 89 256103.

[17] Ranarao G , Ranjans ahu H 2001 Proc. Indian Academ. Sci. (Chem. Sci.) 113. 497.

[18] Paiano P, Prete P, Lovergine N , Mancini A.M 2006 J. Appl. Phys. 100 094305.

[19] Yang P, Yan H, Mao, Russo S.R, Johnson J, SayKally R, Morris N, Pham J, He J , Choi R 2002 Adv. Matter 12,323.

[20] Kim H.W, Kebede M.A, Kim H.S, Srinivasa B, Kim D.Y, Park J.Y, Subkim S 2010 Current Applied Physics 10, 52-56.

[21] Shalish I, Temkin H , Narayana V , Murti 2002 Phys. Rev. B. 69, 245401.

[22] Yang H, Nie, S 2009 Mater. Chem. Phys. 114, 279–282.

[23] Jayakumar O.D, Gopalakrishnan I.K 2007 J. Cryst. Growth 307, 315–320.

[24] Kim H.I, Choi J.M, Kim D.J, So M.G 2002 J. Ceram. Proc. Res. 3(3), 146–149.

[25] Sui X.M, Shao C.L, Liu Y.C 2005 Appl. Phys. Lett. 87, 113–115.

[26] Liao Z.M, Wu H.C, Fu Q, Thu X, JXu I. , Shrets Z. Zhang, Guo W; Leprince-Wang Y; Zhao Q, Wu X, D-P and Yu 2012 Sci. Rep. 2 CONNEXIONS, p.295.

Chapter 5

Comparison of optical and luminescence properties of as prepared and annealed ZnO nanoparticles prepared using sol-gel method

5.1. Introduction

The development of new materials on the length scale of approximately 1-100 nm has become the focus of the investigations currently due to progress in all areas of industry and technology [1]. These nanomaterials have unique properties and functions that are substantially different from those of bulk materials due to their small size and large surface area [2, 3]. Parameters such as size, distribution of size and morphology may significantly alter the electrical, optical and magnetic properties, which determine the practical applications of nanomaterials [4]. Among the nanomaterials with industrial relevance stands out zinc oxide (ZnO), an n-type semiconductor that displays a hexagonal crystalline wurtzite-type structure, with space group P6 mc and lattice parameters of a = b = 0.3250 nm and c = 0.5207 nm [5]. The importance of ZnO is due to its unusual physical properties such as high conductance, chemical and thermal stability [6], wide and direct band gap of 3.37 eV [7] and a high excitation binding energy of 60 meV [8]. Moreover, it has good radiation resistance [9] and is harmless to the environment [10]. The ZnO nanostructures has great potentiality for being used in preparing solar cell, acoustic, electrical and optical devices, chemical sensors [11] catalysts, pigments, cosmetics, varistors and gas sensors [12-14]. Different techniques are employed to produce these nanostructures, such as molecular beam epitaxy, thermal decomposition, and hydrothermal method, synthesis by vapor phase [15], precipitation [16] sol-gel [17] and solochemical method [18]. Among the techniques employed, sol-gel is suitable for the preparation of ZnO nanoparticles due to its simplicity, versatility and low cost. Compared with other techniques, this method presents as advantages the production of nanoparticles in a short reaction time and in relatively low temperatures.

The particle properties such as morphology and size can be altered via sol-gel method by adjusting of parameters such as growth temperature, concentration and reaction time. The optical and electrical properties are closely related to the crystallite size and orientation, which are affected by the NPs sizes. For instance, optical band gap of nanocrystalline materials depends on the particle radius because of the quantum confinement effect [19].

The influence of the annealing temperature on the properties of ZnO has been reported by several research groups [20]. Normally, the optimum annealing temp is chosen for the best device performance. Therefore, it is very important to study the effect of annealing on structural, morphological and optical properties of ZnO nanoparticles.

5.2. Experimental Procedure

The synthesis of samples for this study followed the same procedure as that of Chapter 4. ZnO nanostructures were prepared from aqueous solutions of zinc acetate dehydrate [Zn $(CH_3COO)_2$. $2H_20$] and sodium hydroxide (NaOH). In the three-neck glass flask, zinc acetate dehydrate was dissolved in ethanol to a concentration of 0.015 M and the resulting solution was heated, under constant stirring, to different growth temperatures (RT, 35, 45, 55, 65 and 75 °C). After achieving a desired temperature of growth, a solution of NaOH was added slowly (dripped for 60 minutes) into the three-neck glass flask containing the [Zn $(CH_3COO)_2$. $2H_20$] aqueous solution under continual stirring. In this procedure the desired reaction temperature was constantly maintained. The suspension formed with the dropping of 0.06 M alkaline aqueous solution to zinc acetate dehydrate solution was kept stirred for two hours at the same growth temperature and allowed to stand for some time till gel like solution was formed. The material was then filtered and washed several times with deionized water. The washed sample was dried at 60 °C in oven for one hour and one portion of it annealed at 600 °C for 1 hour. The yield of the ZnO nanostructures by this method is about 95%.The particle size and morphology and the structural and luminescent properties of the as-synthesized particles were examined by means of scanning electron microscopy, X-ray diffraction, UV-Vis spectroscopy and photoluminescence spectroscopy.

5.3 Results and Discussion

5.3.1 Structural and Compositional analysis

Figure 5.1(a) XRD spectra shows the diffraction patterns of as prepared and annealed ZnO nanoparticles synthesized at 35, 55 and 75 ºC. The XRD pattern reveals typical hexagonal wurtzite structure of ZnO with respect to standard card (JCPDS No. 79-0208). The crystallite sizes of ZnO were calculated using the Scherer's formula [21] $\boldsymbol{D} = \mathbf{0.9}\boldsymbol{\lambda\beta}\mathbf{cos}\boldsymbol{\theta}$ Where λ, θ and $\boldsymbol{D}$ are the X-ray wavelength, Bragg's diffraction angle and crystallite size of the ZnO (101) diffraction peak, respectively.

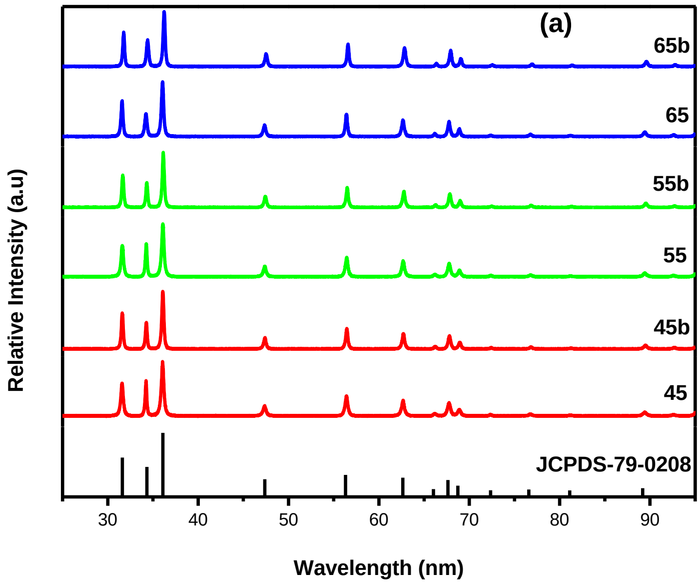

Figure 5.1(a) X- ray powder diffraction pattern for as prepared (45, 55 and 65 ^{O}C) and annealed (45b, 55b and 65b ^{O}C) ZnO nanoparticles prepared at different growth temperature.

Figure 5.1(a) XRD spectra show the typical hexagonal wurtzite structure of ZnO with respect to standard card (JCPDS No. 79-0208). The crystallinity of ZnO is improved with annealing for all growth temperatures as indicated by sharper and higher peak intensities of the annealing ZnO than those of the as prepared particles.

A closer look at the XRD spectra, Figure 5.1(a), show that the preferred (110) orientation of the ZnO nanoparticles slightly shifted to higher diffraction angle with annealing. Lupan et al [22] also observed the shift in diffraction angle to higher 2θ value with annealing of ZnO nanoparticles. Thus the diffraction peak becomes more intensified and narrower with annealing insinuating increase in crystallinity of ZnO.

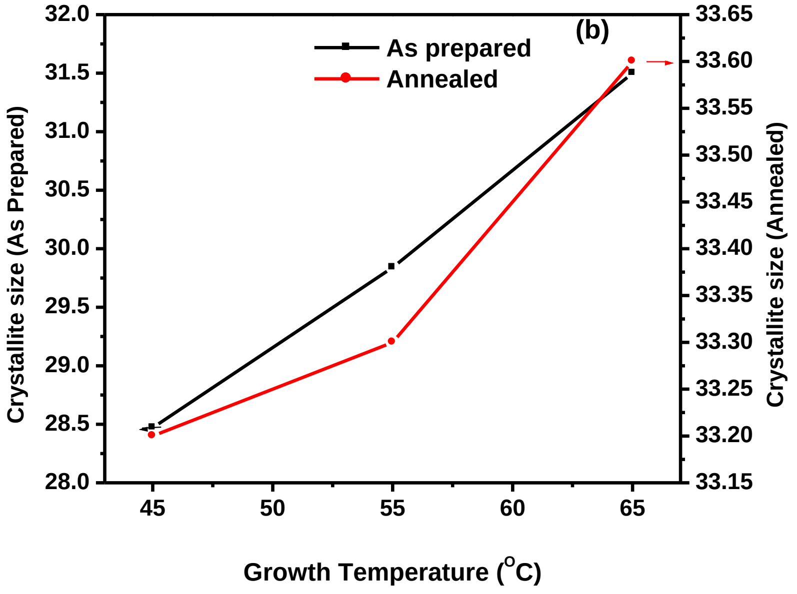

Figure 5.1(b) Variation of crystallite sizes of as prepared and annealed ZnO nanoparticles samples for 45, 55 and 65 ºC growth temperatures.

Figure 5.1(b) shows how annealing has resulted to increase in crystallite sizes of ZnO nanoparticles samples for all growth temperatures. The average crystallite size, estimated by Scherer's equation for the as prepared ZnO is 29.9 nm which is somewhat less than the average crystallite size for annealed ZnO (33.30 nm); such observation could be attributed to the difference in the number of moles of water of crystallization in each material, resulting in more shrinkage relative to the particle coarsening effect upon annealing.

The crystallite sizes of the ZnO particles increased monotonically with annealing for the selected growth temperatures, for example, from 28.47 to 33.20 nm for as prepared and annealed respectively at growth temperature of 45 ºC, indicating the tendency of large grain growth in the nanoparticles due to annealing. It is also noted that the lattice constant of the ZnO nanoparticles (NPs) decreased from 5.307 Å to 5.228 Å (closer to the equilibrium value of 5.204 Å) for as prepared and annealed samples respectively at growth temperature of 75 ºC. These observations suggest that the structural property of the NPs were improved with annealing.

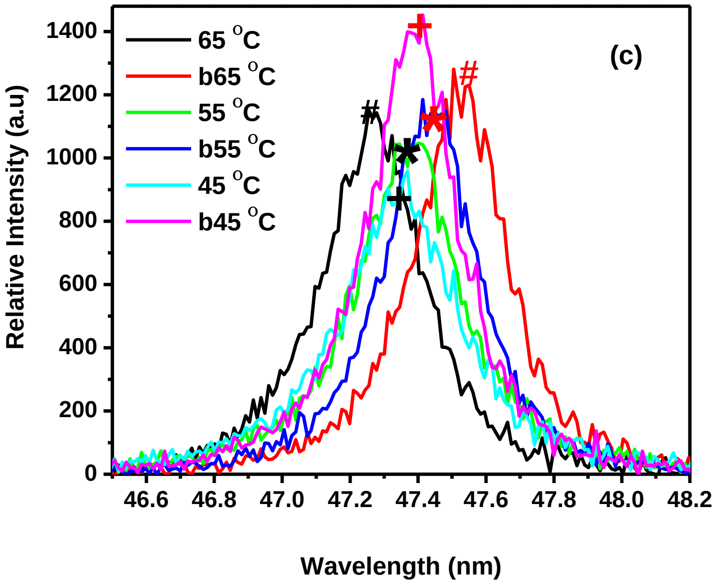

Figure 5.1(c) Comparison of changes in peak (100) intensity and positions for various growth temperatures.

The peak intensities for as prepared ZnO nanoparticles, Figure 5.1(c), increased linearly with growth temperatures but decreased for annealed sample.

However, the peak intensities were higher for samples annealed at 600 ºC due to enhanced and improved crystallization of ZnO nanoparticles.

Motloung et al [23] indicated that the minimum annealing temperature to start forming well purified metal oxide such as ZnO is 400 ^{0}C. Thus, the annealing temperature needs to be higher than 300 ^{0}C to remove all impurities and improve crystal structure of ZnO.

5.3.2 Surface morphological analysis

Figures 5.2(a) (45, 45b,65 and 65b) show that as prepared ZnO samples are made of irregularly shaped, overlapped nanoparticles and somehow, inhomogeneous and spherical particles along with some chunky particles in agreement with Kumar et al (24), who indicated that as-prepared ZnO have amorphous nature, while the annealed ZnO have a hexagonal wurtzite structure.

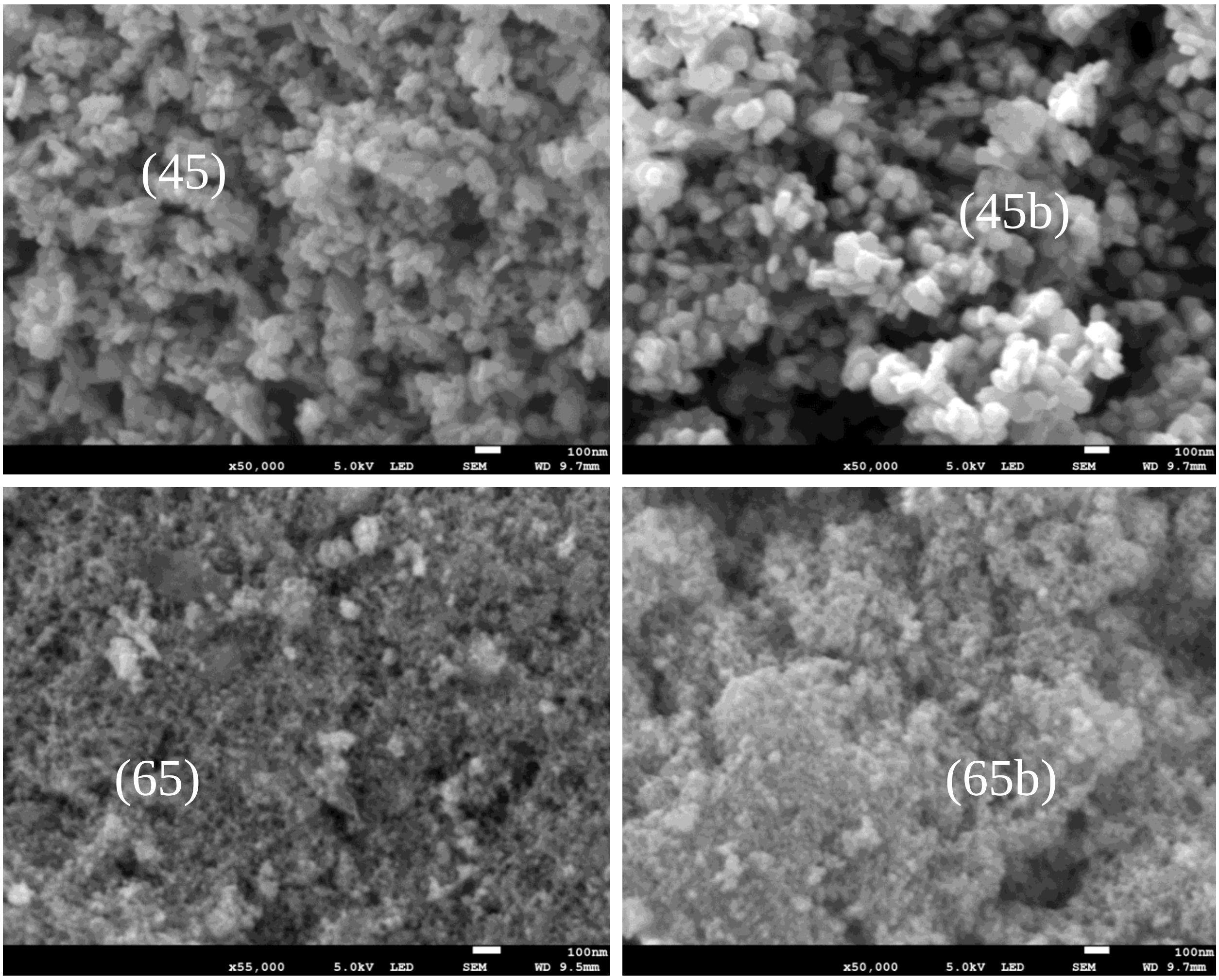

Figures 5.2 (a) SEM Micrographs of as-prepared (45 and 65 °C) and annealed (45b and 65b) ZnO naonoparticles synthesized at 45 and 65 °C growth temperatures.

Removal of lattice water upon annealing process enhanced the nanoparticles' features. Regular, polyhedral nanoparticles were observed for ZnO after annealing. Raoufi et al [25] on the study of the effect of annealing on the morphology of ZnO nanoparticles indicated that with annealing, ZnO nanoparticles aggregate and become larger in diameter due to annealing [26].

The EDS analyses, Figure 5.2(b), for as prepared and annealed samples indicate the purity of all the synthesized samples with no peaks other than Zn and O. Un- and annealed ZnO nanoparticles adopt hexagonal shape, which is consistent with the regular, polyhedral morphology observed by SEM.

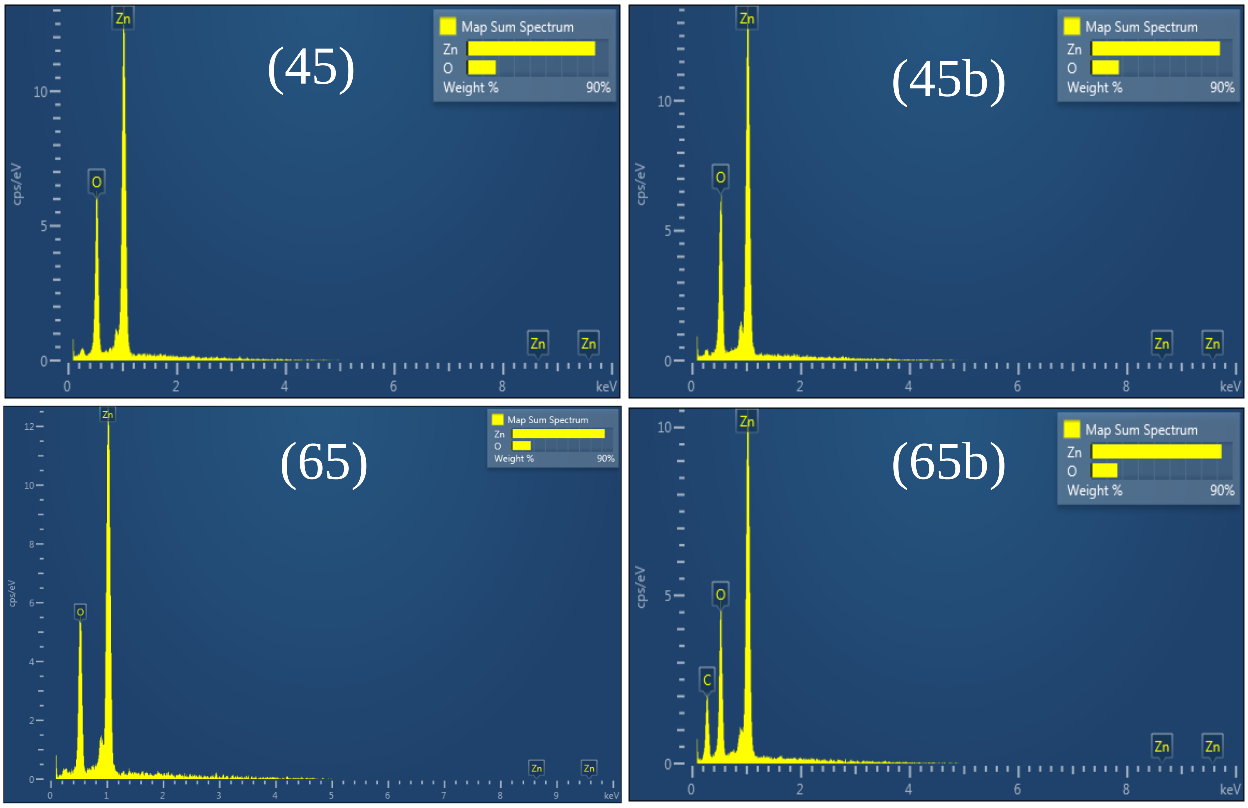

Figures 5.2(b) EDS spectra for as-prepared (45 and 65) and annealed (45b and 65b) ZnO nanoparticles synthesized at 45 °C and 65 °C growth temperatures.

5.3.3 Photoluminescence Analysis

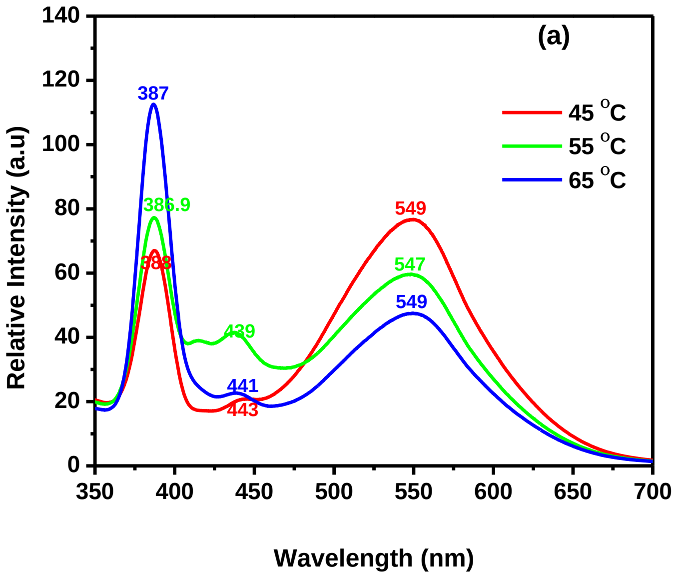

Figure 5.3(a) PL emission spectra for as prepared ZnO nanoparticles prepared at 45, 55 and 65 ºC growth temperatures.

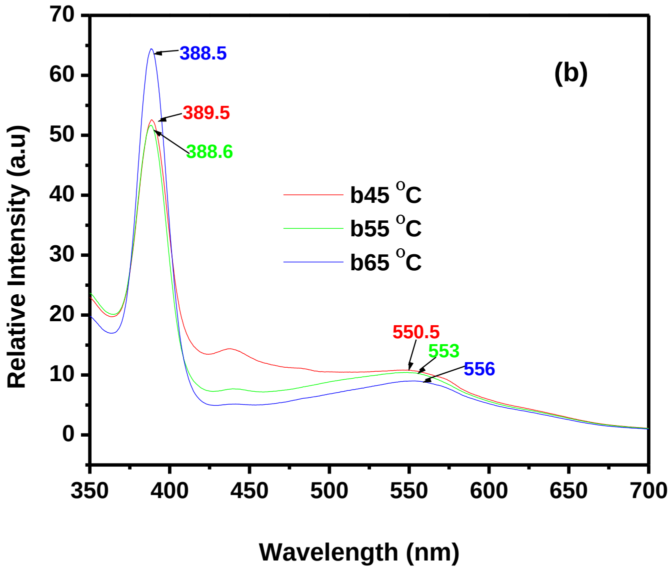

Figure 5.3 (b) PL emission spectra for annealed ZnO nanoparticles prepared at 45, 55 and 65 ºC growth temperatures.

Strong broad deep-level emission which extends from UV region to visible region is observed in Figure 5.3(a) for the as-prepared nanoparticles. Figure 5.3(b) shows the emission spectra of the annealed ZnO nanoparticles to study the influence of annealing temperature on ZnO nanoparticles. Annealing at 600 ℃ quenches the blue luminescent efficiency of the DLE and enhances excitonic peak emission. Therefore concentration of zinc vacancy and zinc interstitial related defects is drastically decreased by annealing process.

Table 5.1 Change in excitonic peak emission positions for as prepared and annealed ZnO nanoparticles prepared at growth temperatures of 45, 55 and 65 ºC

ZnO Samples	**Growth Temperature (°C)**	**UV peak**		**DLE peak**	
		Position (nm)	**Intensity (a.u)**	**Position (nm)**	**Intensity (a.u)**
Un annealed	45	387.8	66.4	549.5	76.2
	55	387.8	76.9	548.2	59.3
	65	387.8	112.5	549.5	47.0
Annealed	45	388.5	52.5	556.0	10.5
	55	388.5	51.3	552.0	10.2
	65	389.2	64.1	553.6	9.0

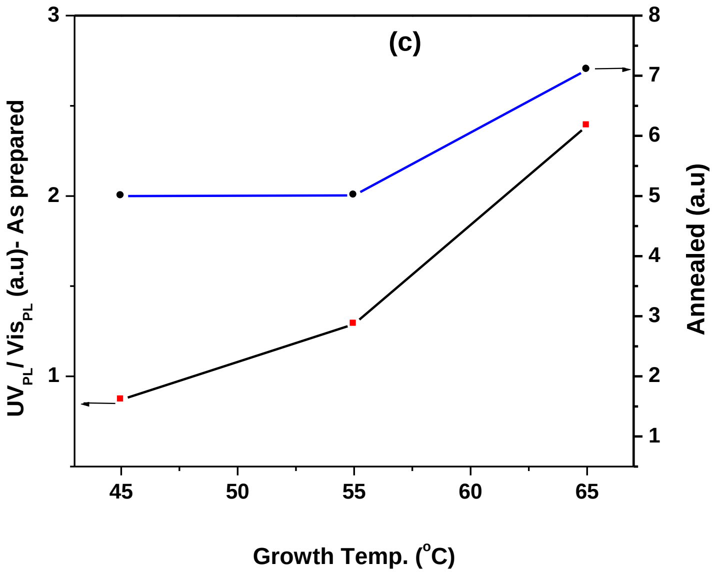

Figure 5.3(c) Graph of ratio of intensities of ultraviolet photoluminescence to that of visible photoluminescence (UV_{PL}/ Vis_{PL}) intensities.

From comparison of changes in both excitonic peaks and DLE peaks emission positions for as prepared and annealed ZnO nanoparticles detailed in table 5.1, red shift in the peak positions for all growth temperatures were observed due to annealing; the trend which agrees with the reflectance measurements. The red shift in the visible emission with increasing particle size closely follows the red shift in the band edge emission, indicating that the two are related. The observed red shift in the position of the band edge emission could be due to band gap narrowing as a result of annealing and increase in crystallite size. Other researchers also proved that the annealing treatment modify the green emission [27].

5.3.4 Optical properties

UV-Vis reflectance spectra showed, Figs. 5.4(a) and (b), undergo red shift in the absorption edge after annealing due to the size effect of nanostructures [28]. Irimpan et al. [29] also reported red shift corresponding with the variation of the crystallite sizes.

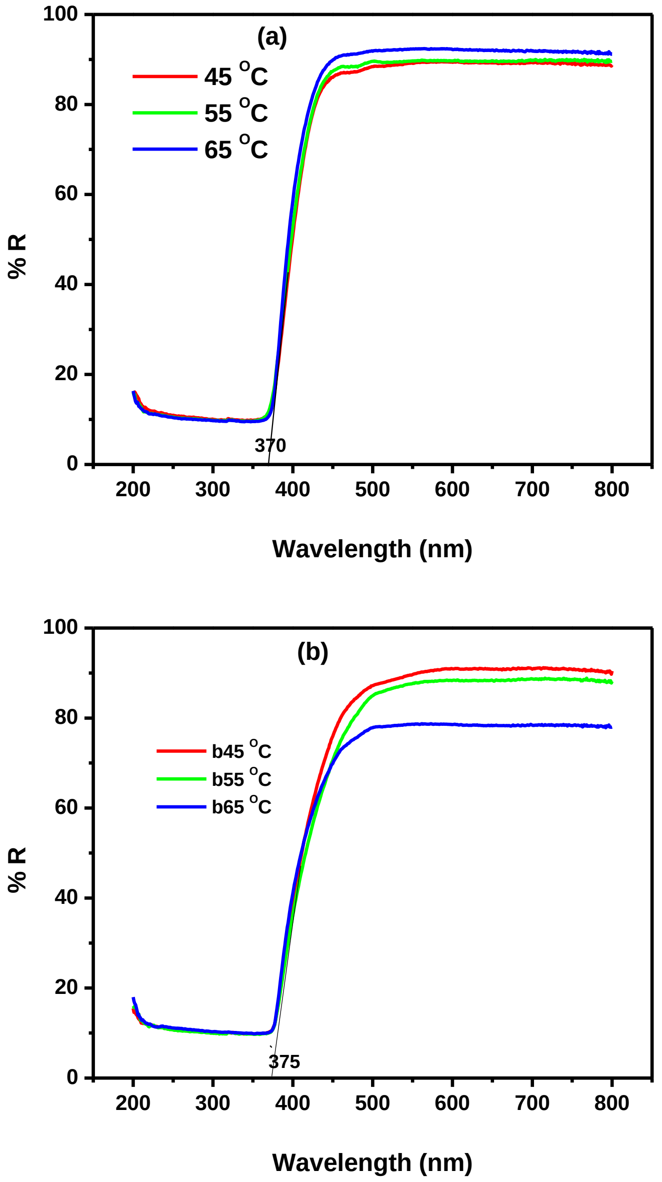

Figure 5.4(a) Reflectance Spectra of as prepared and (b) annealed ZnO nanoparticles prepared at 45, 55 and 65 ºC growth temperatures.

The band gap energy of ZnO nanoparticles was calculated using the common Kubelka Munk's equation. The energy was found, Figures 5.5(a) and (b), to reduce slightly with annealing. The average band gap is observed to vary from 3.254 to 3.232 eV with change in nanoparticle size from 29.91 to 33.30 nm as caused by annealing. The small crystallite size makes ZnO nanoparticles to be potentially used as electrode in solar cells and gas sensing applications.

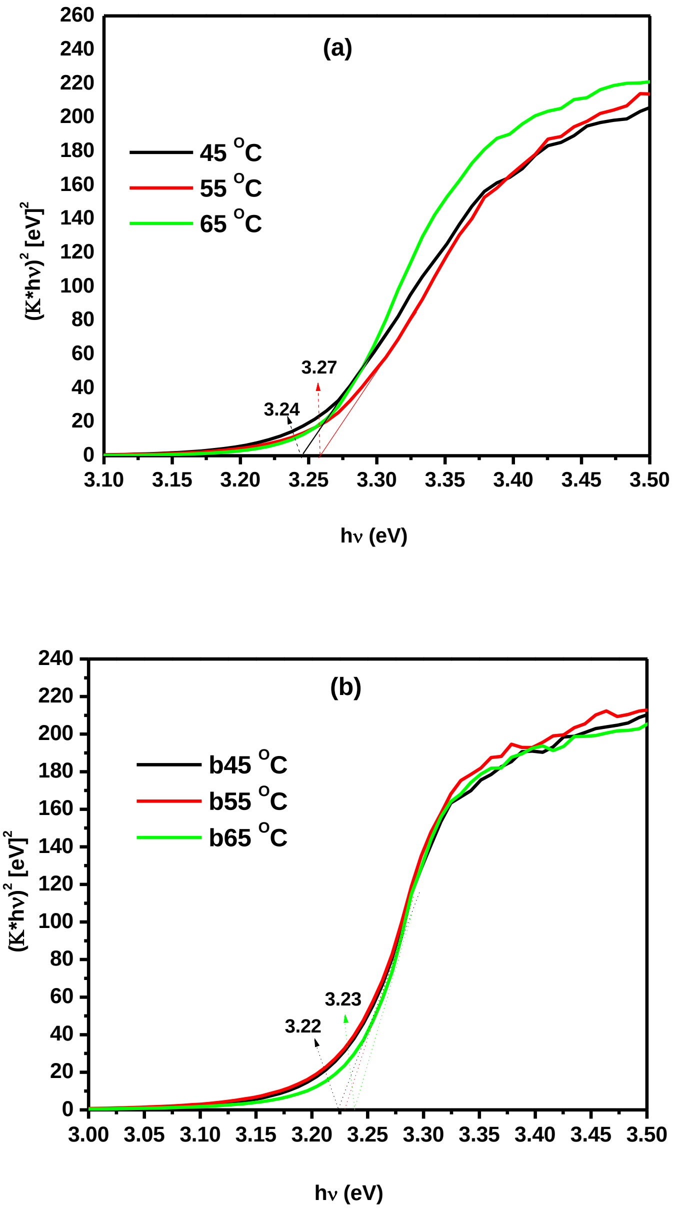

Figure 5.5(a) band gap curves of as prepared and (b) annealed ZnO nanoparticles prepared at 45, 55 and 65 ºC growth temperatures.

.

Conclusion

ZnO nanoparticles were synthesized using sol-gel method. The structural and optical properties were investigated by X-ray diffraction (XRD), scanning electron microscopy (SEM), photoluminescence (PL), UV-Vis spectroscopy and EDS. XRD analysis demonstrates that the crystallinity of ZnO is improved with annealing for all growth temperatures as indicated by sharper and higher peak intensities of the annealed ZnO compared to that of the as prepared particles. The crystallite sizes of the ZnO particles increased monotonically with annealing for the selected growth temperatures indicating the tendency of large grain growth in the nanoparticles due to annealing.

SEM micrographs showed that as prepared ZnO samples are made of irregularly shaped, overlapped nanoparticles and somehow, inhomogeneous and spherical particles while the annealed ZnO were relatively regular and polyhedral. The EDS analyses, for as prepared and annealed samples indicate the purity of all the synthesized samples with no peaks other than Zn and O. Annealing at 600 ℃ quenches the blue luminescent efficiency of the DLE and enhances excitonic peak emission. The red shift in the visible emission with increasing crystallite sizes closely follows the red shift in the band edge emission, indicating that the two are related. The observed red shift in the position of the band edge emission could be due to band gap widening as a result of annealing and increase in crystallite size.

References

[1] Gleiter H., 2000, Nanostructured materials: basic concepts and microstructure, Acta mater. 48, 1-29.

[2] Cushing B.L., Kolesnichenko V.L. and O’Connor C.J., 2004, Recent advances in the liquid-phase syntheses of inorganic nanoparticles, Chem. Rev. 104, 3893-3946.

[3] Gusati (G) Alivisatos A.P., 1996, Perspectives on the physical chemistry of semiconductor nanocrystals, J. Phys. Chem. 100, 13226-13239.

[4] Lisiecki I., 2005, Size, shape, and structural control of metallic nanocrystals, J. Phys. Chem. B 109, 12231-12244.

[5] Liu R., Vertegel A.A., Bohannan E.W., Sorenson T.A. and Switzer J.A., 2001, Epitaxial electrodeposition of zinc oxide nanopillars on single-crystal gold, Chem. Mater. 13, 508-512.

[6] Kaur R., Singh A.V., Sehrawat K., Mehra N.C. and Mehra R.M., 2006, Sol–gel derived yttrium doped ZnO nanostructures, J. Non-Cryst. Solids 352, 2565-2568.

[7] Kubota J., Haga K., Kashiwaba Y., Watanabe H., Zhang B.P. and Segawa Y., 2003, Characteristics of ZnO whiskers prepared from organic-zinc, Appl. Surf. Sci. 216,

431-435.

[8] Singh S., Thiyagarajan P., Kant K.M., Anita D., Thirupathiah S., Rama N., Tiwari B., Kottaisamy M. and Rao M.S.R., 2007, Structure, microstructure and physical properties of ZnO based materials in various forms: bulk, thin film and nano, J. Phys. D: Appl. Phys. 40, 6312-6327.

[9] Reynolds D.C., Look D.C. and Jogai B., 2001, Fine structure on the green band in ZnO, J. Appl. Phys. 89, 6189-6191.

[10] Wu C., Qiao X., Chen J., Wang H., Tan F. and Li S., 2006, A novel chemical route to prepare ZnO nanoparticles, Mater. Lett. 60, 1828-1832.

[11] Hong R., Pan T., Qian J. and Li H., 2006, Synthesis and surface modification of ZnO nanoparticles, Chem. Eng. J. 119, 71-81.

[12] Park J.-H., Oh S.-G. and Jo B.-W., 2004, Fabrication of silver nanotubes using functionalized silica rod as templates, Mater. Chem. Phys. 87, 301–310.

[14] Toby B.H., 2001, EXPGUI, a graphical user interface for GSAS, J. Appl. Cryst. 34, 210-213.

[15] Hu Y. and Chen H.J., 2008, Preparation and characterization of nanocrystalline ZnO particles from a hydrothermal process, J. Nanopart. Res. 10, 401-407.

[16] Cai K.F., He X.R. and Zhang L.C., 2008, Fabrication, properties and sintering of ZnO nanopowder, Mater. Lett. 62, 1223–1225.

[17] Moghaddam F.M. and Saeidian H., 2007, Controlled microwave-assisted synthesis of ZnO nanopowder and its catalytic activity for O-acylation of alcohol and phenol, Mater. Sci. and Eng. B 139, 265-269.

[18] Vaezi M.R. and Sadrnezhaad S.K., 2007, Nanopowder synthesis of zinc oxide via solochemical processing, Mater. Des. 28, 515-519.

[19] Lai Y, Meng M, Yu Y, Wang X and Ding T 2011 Applied Catalysis B: Environmental 105 335 – 345.

[20] Kumar Vinod, Singh N, Kapoor A, Ntwaeaborwa O.M and Swart H.C 2013 Mater. Res. Bull. 48 4596 – 4600.

[21] Vanheusden K , Seager C.H, Warren W.L, Tallant D.R. and Voigt J.A 1996 Appl. Phys. Lett. 68 403.

[22] Lupan O, Pauporte T, Chow L, Viana B, Pelle F, Ono L.K, Cuenya B.R and Heinrich H 2010 Appl. Surf. Sci. 256 1895 – 1907.

[23] Motloung S.V, Dejene B.F, Swart H.C and Ntwaeaborwa O.M 2014 J. Sol-Gel Sci. Technol. 70 422 – 427.

[24] Kumar P, Malik H.K , Ghosh A , Thangavel R , Asokan K 2013 Appl. Phys. Lett. 102 221903.

[25] Raoufi D 2013 Renewable Energy. 50 932 – 937.

[26] Liu Z, Liu C, Ya J and Lei E. 2010 Solid State Sci. 12 111 – 114.

[27] Lu H.Y, Chu S.Y and Tan S.S 2004 J.Cryst.Growth 269 385 – 391.

[28] Samanta P. K, Patra S. K , Ghosh A and Chaudhuri P.R 2009 I. J. N. N. 1 81 – 90.

[29] Pandiyarajan T, Baesso M.L and Karthikeyan B. 2014 Eur. Phys. J. D 68 28 – 36.

Chapter 6

Effect of solvent medium on the ZnO material properties synthesized by sol-gel method

6.1. Introduction

ZnO is a direct band gap (~3.37 eV) semiconductor with a large exciton binding energy (60 meV) [1]. It is a promising candidate for visible and ultra-violet (UV) light emitting diodes (LEDs) [2]. ZnO nanostructure materials find diverse applications for use in optoelectronics [3, 4], sensors [5], data storage [6], biochemical/chemical sensors [7, 8], solid state lighting sources [9] solar cells [10, 11] and transparent conducting oxides [12]. High crystallinity of zinc oxide nanoparticles is one of the most important factors in achieving a high UV emission efficiency. Good optical and luminescence properties of ZnO are very important for its application in different optoelectronic devices. In general, the photoluminescence (PL) spectrum of ZnO has two luminescence bands: one is in the UV near band edge emission around 380 nm and is attributed to the direct recombination of photo generated charge carriers; whereas the other is a defect related deep level emission (DLE) or visible emission, which depends upon the preparation methods and growth conditions. DLE is attributable to the recombination of a shallowly trapped electron with a deeply trapped hole [13, 14] and is mainly important for white-light (LEDs). Solvents play a crucial role in a reaction; they provide a means of temperature control by determining the highest temperature at which the reaction will occur. The polar characteristic of the solvent was proposed to be the main factor that affects both nucleation and growth of ZnO nanoparticles and, consequently, determines the shape, size, and aspect ratio of the products. Previous studies also show that particle growth and coarsening are strongly dependent on solvent through the viscosity, bulk solubility, and surface energy. The solvent, thus, is an important parameter in determining various reaction kinetics, and that by choice of solvent; the resulting ZnO nanoparticle properties can be tuned. In this paper water, ethanol and water-ethanol mixture are used as solvent media. Excess of Sodium hydroxide is generally known to generate an intermediate hydroxide $Zn(OH)_2$ upon reaction with the zinc salt [19]. But if there is no water in the reaction mixture, the hydrolysis process would be slow. In fact, use of ethanol-water mixture (more ethanol and less water) as solvent in the pH range 8.5-12 is believed to produce ZnO nanoparticles with good yield. Many methods have been used for synthesizing ZnO nanoparticles including sol–gel [15], co-precipitation [16], hydrothermal [17] and combustion method [18]. A well-controlled synthesis process at low temperature is needed for the economical use of ZnO in catalytic applications such as water treatment and other environmental applications.

In this study, the influence of solvent on the synthesis of ZnO nanoparticles from zinc acetate at constant temperature of 35 ^{o}C is reported. The influence of the solvent provides a means to achieve control over the ZnO nanoparticle size and size distribution, which is essential for tailoring optical, electrical, chemical, and magnetic properties of nanoparticles for specific applications. Sol-gel method is preferred because it is simple, fast, rapid and economically efficient for large production.

6.2. Experimental procedure

The first experiment involved preparation of ZnO nanoparticles in different volume ratios of water to ethanol at growth temperature of 35 ℃. The chemical reagents used in this experiment, sodium hydroxide (NaOH) and zinc acetate dihydrate ($Zn(CH_3CO_2)_2.2H_2O$), were of analytical grade and were used without further purification. Zinc acetate dihydrate was used as the Zn source while ethanol and water were used as solvents. The production unit of ZnO nanoparticles consists basically of a jacketed three-neck glass flask and a magnetic stirrer with temperature control. To prepare ZnO nanoparticles in water solvent (ZnO_w), in the three-neck glass flask, zinc acetate was dissolved in deionized water to a concentration of 0.02 mol/l and the resulting solution was heated, under constant stirring, to the temperature of 35 °C. After achieving this temperature, a solution of 0.08 mol/ l of NaOH was added slowly (dripped for 60 minutes) into the three-neck glass flask containing the zinc (II) acetate aqueous solution under continual stirring. In this procedure the reaction temperature was constantly maintained in 35 °C. The suspension that formed with the dropping of alkaline aqueous solution to the zinc acetate solution was kept stirred for two hours at the temperature of 35 °C. The sample was filtered, washed several times with deionized water, dried at 60 °C in oven for 1 hour and separated in to two portions. One portion was kept as prepared sample while the second portion was annealed at 600 ºC in air for 1 hour. The same procedure was carried out to prepare ZnO nanoparticles in ethanol (ZnO_E) and in water-ethanol mixture (ZnO_{WE}) medium instead of water. To characterize the ZnO nanoparticles, the XRD pattern was measured on a Philips model Bruker D8 Advance, Germany, X-ray diffractometer with Cu Kα irradiation (λ=1.5406 Å) graphite target and monochromatized secondary V = 40kv, A = 40mA, Ni filter in the 2θ range from 20° to 80°. The X-ray diffraction (XRD) investigation gives the information about the structure of the nanoparticles. The preferred orientation of grains, grain size, stress, strain, etc can be obtained from the analysis of the profile width and shape, intensity and position of XRD peaks. The surface morphology was studied using a Shimadzu model SSX-550 Superscan Scanning Electron Microscope. PL measurement was performed on a Cary Eclipse fluorescence spectrophotometer; model LS-55 with a built-in 150W xenon flash lamp as the excitation source and a grating to select a suitable excitation wavelength. The reflectance spectra were collected using a Perkin Elmer Lambda 950 UV-Vis photo spectrometer.

In the secod experiment, the following procedure was followed: ZnO solution was prepared at room temperature by dissolving 0.02 mol of zinc acetate in water or ethanol or both water and ethanol in specific ratio to give a total volume of 100ml. Then solution of sodium hydroxide (NaOH) was prepared by dissolving 0.08 mol of NaOH in water or ethanol or both to give a total volume of 130ml .When both water and ethanol were used to make the solvent, they were mixed in the ratio 0.25 : 0.75 (sample a) and 0.5 : 0.5 (sample b) of water to ethanol. Sample (c) was dissolved in ethanol, while sample (d) water only. The solution of NaOH prepared was placed in a burette and titrated against 100ml of zinc acetate in a beaker while stirring continuously with magnetic stirrer. Titration duration for samples (a) and (b) was about 25minutes, and 10min for samples (c) and (d), The resulting solution after titration, for samples (a) and (b) was vigorously stirred at ambient temperature for 2 hours to let the mixture mix thoroughly, then it was allowed to stand for some time till gel-like solution formed. This was rinsed with distilled water, filtered and dried at 60 ^{o}C for 1 hour. Samples(c) and (d) were stirred for 1 hour, filtered and left to dry at room temperature.

The samples prepared using this method were also characterized and the results discussed.

6.3. Results and Discussion

6.3.1 SEM and EDS Analysis

The SEM images of the samples are shown in Figure 6.1.The morphologies of ZnO nanoparticles changed with water to ethanol sample ratios. The samples prepared in water medium are nanoflakes which are turned to spheres and rods with increasing volume ratios of ethanol. ZnO_E particles (prepared in ethanol) form agglomerated tiny rods as shown in Figure 6.1(d), whereas ZnO_W (prepared in water), has irregular spherical shape.

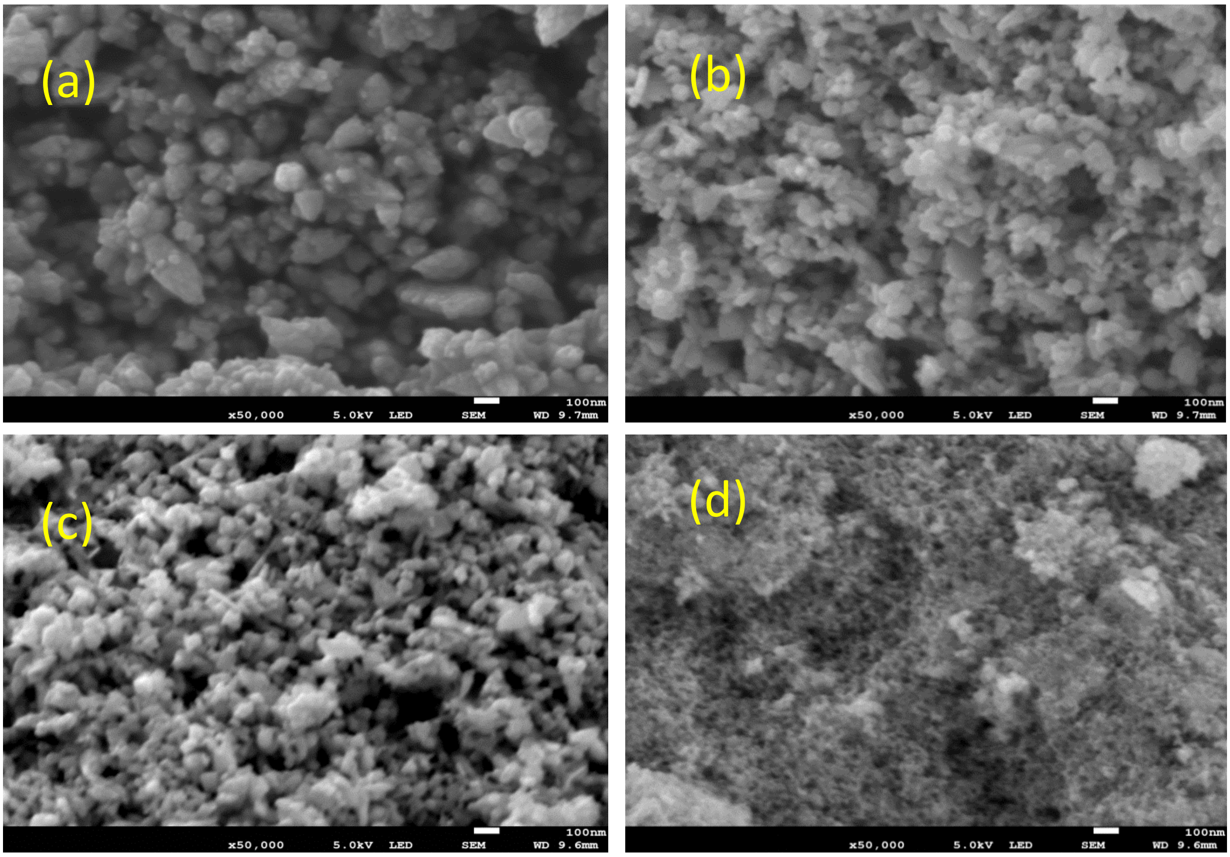

Figure 6.1 SEM images of ZnO Nanoparticles prepared at different volume ratios of water to ethanol solvent (a)ZnO_W ,(b) $ZnO_{WE(0.5:0.5)}$, (c) $ZnO_{WE(0.25:0.75)}$ and (d) ZnO_E Samples.

ZnO_E nanoparticles adopt a regular, polyhedral morphology with an average particle size of approximately 16 nm, obtained from XRD Figure 6.4 insinuating that organic solvents promote the formation of spheres and rods as has been reported [20]. However, ZnO_W

samples are inhomogeneous, spherical, irregularly shaped, chunky and overlapped with an average particle size of approximately 22 nm (Figure 6.1(a)).

The spherical shape of ZnO_W particles are believed to have much less active sites due to the lack of edges and corners. On the other hand, the more uniform polyhedral particles of ZnO_E could be attributed to the lower polarity of ethanol, compared to that of water, leading to slower ionization and deposition rate [21] and inhomogeneous nucleation that favour the polyhedral-shaped particles [22] thus, particles formed when ethanol was used as a solvent are so small, very unstable and tend to agglomerate. SEM results indicated that by increasing the solvent ratio of ethanol, the dimension of the ZnO nanoparticles reduces. The optimum solvent medium for synthesizing high crystallinity and smaller sized ZnO nanoparticles was determined to be ZnO_{WE} (water and Ethanol mixture solvent). Smaller sized ZnO nanoparticles was determined to be ZnO_{WE} (water and Ethanol mixture solvent).

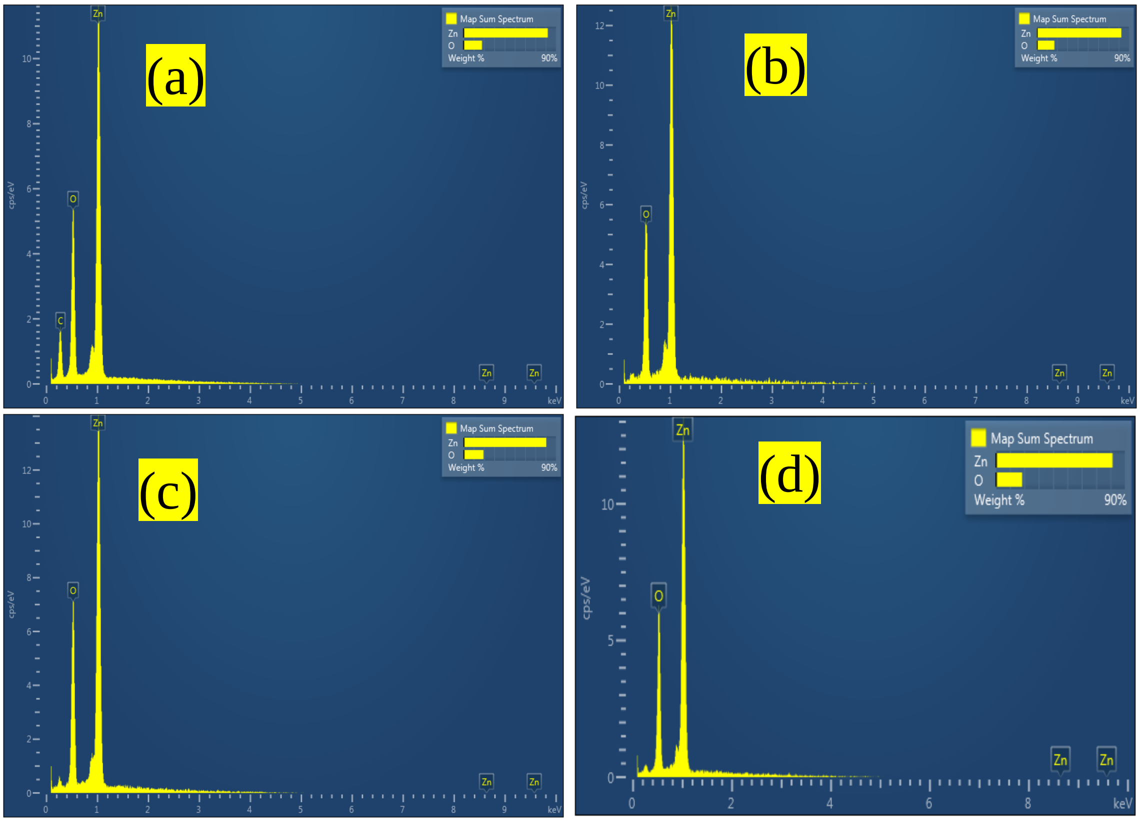

Figure 6.1.2 Energy Dispersive Spectra of Zno Nanoparticles Prepared in Varying Ratios of Water:Ethanol (a)ZnO_W ,(b) $ZnO_{WE(0.5:0.5)}$, (c) $ZnO_{WE(0.25:0.75)}$ and (d) ZnO_E Samples.

Since the images from the SEM cannot definitively prove that the obtained nanoparticles actually consist of ZnO, the elemental composition of the particles was analyzed using Jeol JSM-7800F Field Emission equipped with Oxford Aztec EDS (Energy-dispersive X-ray spectroscopy). Each element has a unique electronic structure, allowing X-rays that are characteristic of an atom structure to be identified.

The EDS spectra in Figure 6.1.2 indicate that the collected powder is composed of zinc and oxygen and the route has pure ZnO phases. This high purity of the ZnO nanoparticles was further confirmed by XRD analysis, Figure 6.2(a). However, some traces of Carbon element was found in the sample prepared using water only, Figure 6.1.2(a) ZnO_W which could be attributed to the oxidation reaction with oxygen. The results of XRD and EDS indicate that we can prepare the wurtzite phase ZnO from aqueous solution containing zinc acetate and sodium hydroxide through Sol-gel method at low temperature (30 ºC).

In the case of second experiment, when ZnO nanoaprticles were prepared at room temperature, representative SEM micrographs for ZnO nanoparticles prepared with water, ethanol and their mixtures are shown in the Figure 6.1.3 below

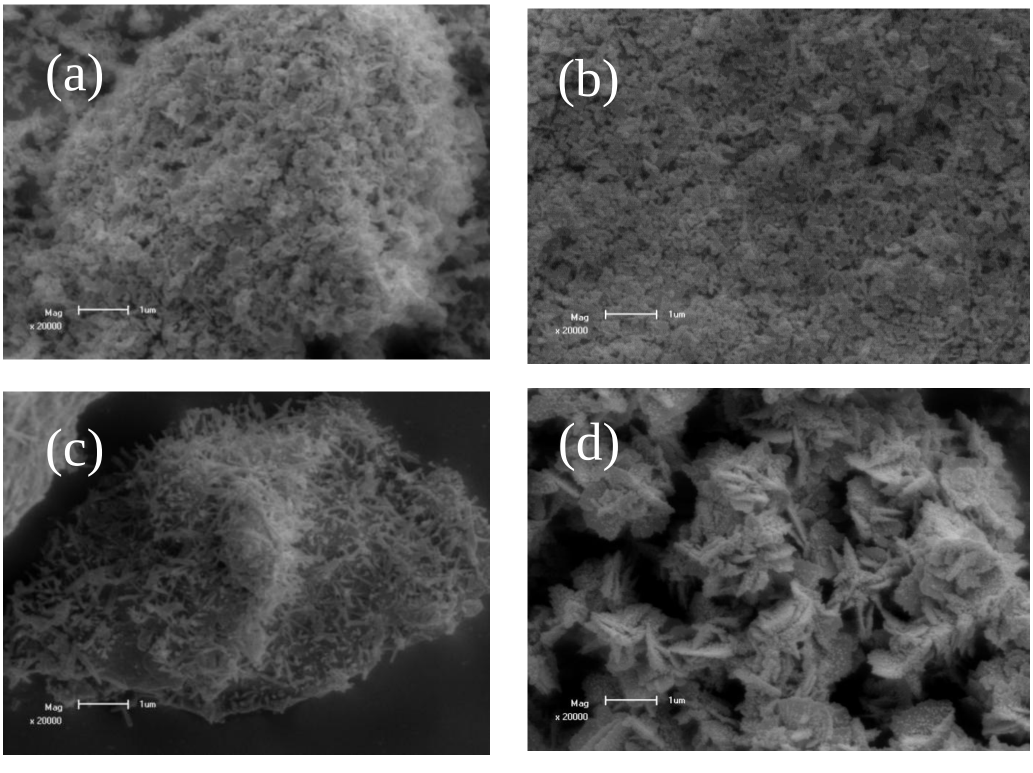

Figure 6.1.3 SEM images of ZnO nanoparticles prepared using (a) water and ethanol in the ratio 0.25: 0.75 (b) water and ethanol in the ratio 0.5: 0.5 (c) ethanol and (d) water

It can be observed that powders are in the form of agglomerates with non-uniform shapes and sizes caused by the difference in solvents used and their ratios. Figs. 6.3(a) and (b) show spherical nanoparticles. In (a) particles are larger than in (b) which can be attributed to more volume of ethanol used in (a*).* Figure 6.1.3(c) shows nanowire-like shapes, which are thin and highly agglomerated, obtained when only ethanol was used. While star-like, nanorods shapes observed when only water was used as shown in Figure 6.1.3(d). Essentially, water solvent favors growth of larger particles as depicted by SEM micrographs.

6.3.2 XRD Analysis

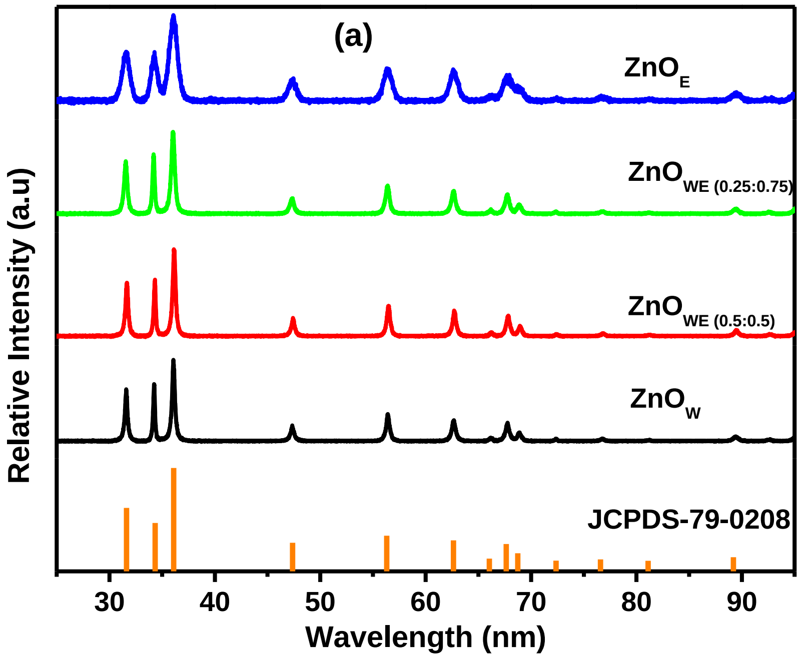

Figure 6.2(a) XRD patterns of ZnO nanoparticles prepared in different volume ratios of water to ethanol solvent (ZnO_W, ZnO_{WE} and ZnO_E samples).

Figure 6.2(a) shows the XRD diffraction patterns of ZnO nanoparticles prepared in water, ethanol and water-ethanol mixture. While Figure 6.2(b) shows the peaks relative intensities and particle sizes. The patterns consist of broad peaks, which match the common ZnO hexagonal wurtzite structure and have calculated average lattice parameters of a = 3.2714 Å, c = 5.212 Å, which are in agreement with the reported standard values (JCPDS No.79-

0208). No peaks from impurities, such as Zn, are detected in the patterns, indicating the product is of high purity. The sharp prominent diffraction peak at around 2θ = 36.1° corresponding to the reflection on (101) plane of ZnO is dominant and indicates that in the respective particles, ZnO nanoparticles are predominantly c-axis orientated [23].

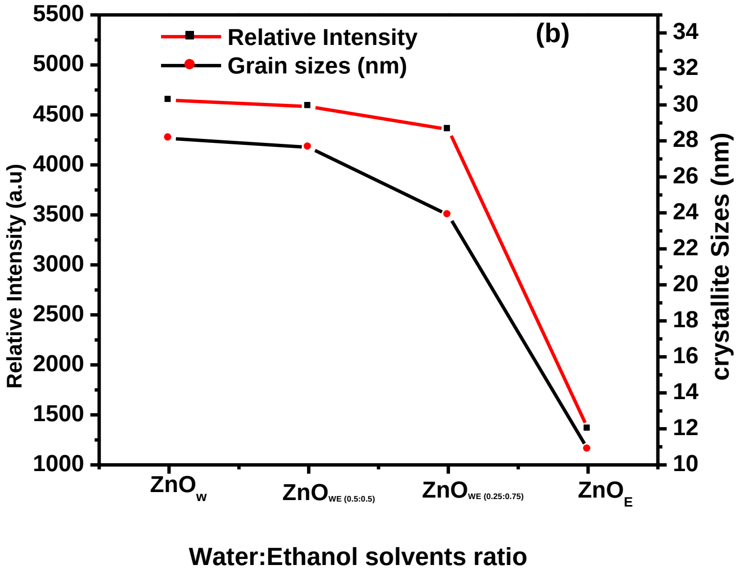

Figure 6.2(b) XRD patterns of ZnO nanoparticles peaks relative intensity and particle crystallite size.

Diffraction peaks for the ZnO_W nanoparticles become sharper and the full width at half maximum of the peaks is narrower than others, indicating the excellent crystal quality resulting from water medium as solvent. The average crystallite size of the products was estimated from XRD peaks using Debye-Scherrer's equation.

$$D = \frac{0.94\lambda}{\beta \cos\theta} \qquad (1)$$

Where, λ is the wavelength of the incident X-ray beam; θ, the Bragg's diffraction angle; and β is the full width at the half-maximum in radians. The sizes for as prepared ZnO nanoparticles were: 28.1 nm, 27.6 nm, 23.8, and 10.8 nm prepared using water: ethanol solvent ratios of 1:0, 0.5:0.5, 0.25:0.75 and 0:1 respectively, which indicates that the crystallite sizes decrease while the FWHM of the diffraction peaks increase with increasing volume ratios of ethanol solvent. Clear sharpening of peaks, increased intensity and narrowing of peaks can be observed with decreasing volume ratios of ethanol. This suggests that as the ZnO nanoparticles become bigger, the intensity of diffraction peaks increased due to the increase in the crystallinity of the nanoparticles [24, 25]. Thus in order to have smaller particles more volume ratios of ethanol solvent is preferred. However, after annealing the samples at 600ºC in air for an hour the relative intensities of peaks and grain sizes increased with the increase in volume ratios of ethanol, Figure 6.2(c), but the FWHM of the of the (101) peak decreased.

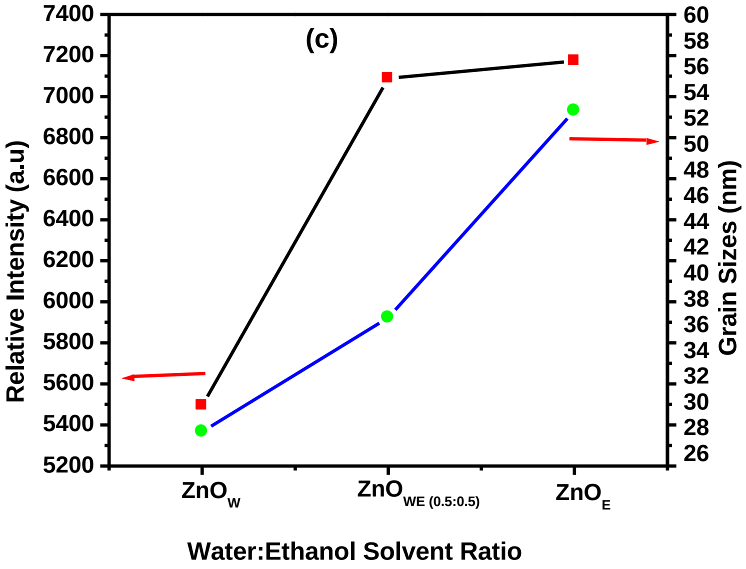

Figure 6.2(c) XRD patterns of annealed ZnO nanoparticles at varying volume ratios of solvents.

The decrease of the FWHM with increasing ethanol volume ratio during annealing could be due to the coalescences of grains at higher temperatures [26]. Interestingly, ZnO_E grain sizes were twice larger than those of ZnO_W thus reversing the trend in grain size and intensity changes. The intensities of ZnO_E significantly exceeded that of ZnO_w with annealing. Such observation could be attributed to the difference in the number of moles of water of crystallization in each material, resulting in more shrinkage relative to the particle coarsening effect upon annealing [27].

Numerical values of the lattice spacing for the ZnO nanoparticles were also calculated and tabulated in Table 6.1, from the XRD data according to the following equations [28];

$$2d_{hkl}\sin\theta = n\lambda \qquad (2)$$

Where, d_{hkl} is lattice spacing of (hkl) and θ is the Bragg angle (half of the peak position angle).

Table 6.1 Variation of lattice parameters with solvent volume ratio

	ZnO_W	$ZnO_{WE\ (0.5:0.5)}$	$ZnO_{WE\ (0.25:0.75)}$	ZnO_E	Average
a	3.2695	3.27061	3.2741	3.2714	3.2714
c	5.2270	5.2147	5.1963	5.2104	5.2121
c/a	1.5987	1.5944	1.5871	1.5927	1.5932

For the wurtzite structure the interplanar distance of the (hkl) plane is related to the lattice parameters *a* and *c* via the miller indices hkl.

$$\left(\frac{1}{d_{hkl}}\right)^2=\frac{4}{3}\left(\frac{h^2+k^2+hk}{a^2}\right)+\frac{l^2}{c^2} \qquad (3)$$

Where, a and c are the lattice constants; h,k,l are miller indices. With the first order approximation n=1, the lattice constants were calculated using the least square method [29]. The experimental average lattice constants *a* and *c* of ZnO nanoparticles were determined as 3.2714 Å and 5.2121 Å respectively. These values are slightly higher than the bulk lattice constants (a=3.2498 Å and c=5.2066 Å [30]). The deviation of the lattice parameters is caused may be due to presence of various point defects such as zinc antisites, oxygen vacancies, and extended defects such as threading dislocation. The mean ratio c/a of ZnO nanoparticles is slightly less than that of pure ZnO (1.604). Moreover, values of the lattice parameter c, table 6.1, generally decreased with an increase in volume ratios of ethanol in the solvent. This may be due to the lattice contraction resulting from the presence of dangling bonds on the surface of the ZnO nanoparticles.

The values of strain along the c-axis (hkl) was calculated using the following formula [31]

$$\varepsilon_{zz} = \frac{c-c_o}{c_o}\ 100\% \qquad (4)$$

Where c is the lattice parameter of the strained ZnO nanoparticles calculated from X-ray diffraction data and c_o (5.207) is unstrained lattice parameter of ZnO.

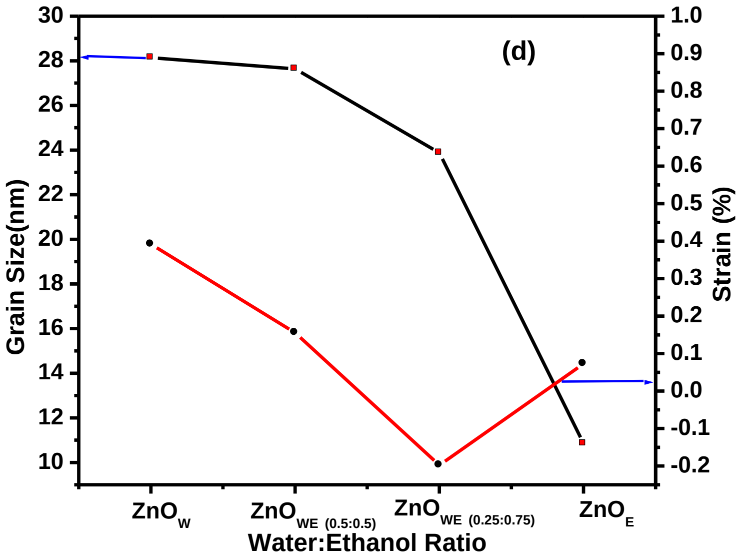

Figure 6.2(d) Variation of grain size and strain of the ZnO nanoparticles with volume ratios of water: Ethanol

The lattice parameters of ZnO nanoparticles, prepared at different volume ratios of ethanol solvent, yield an hexagonal unit cell which are very close to the parameters of a = 3.250 A° and c = 5.207 A°(JCPDS 36-1451) The difference in c-axis lattice parameter has to be attributed to the occurrence of stress in the nanoparticles. The strain can be negative (compressive) or positive (tensile). Under compression (parallel to the surface), the c-axis lattice parameter will decrease, leading to a somewhat larger interplanar distance for the (0 0 2) planes.

The XRD spectra of ZnO nanoparticles prepared at room temperature using the second experimental method is shown Figure 6.2.1 below.

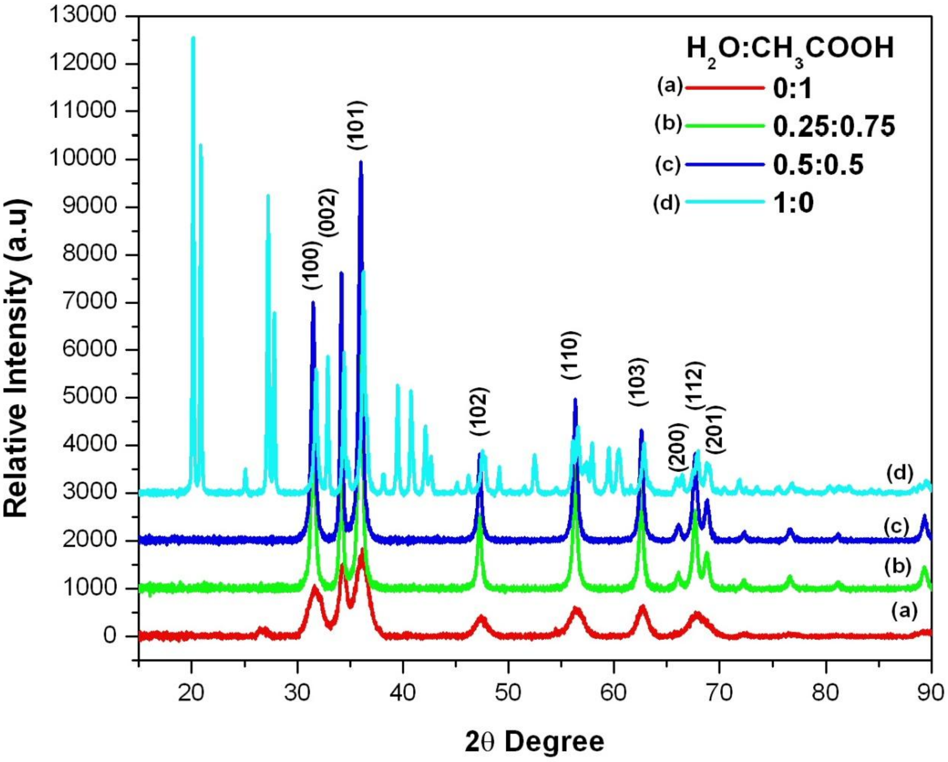

Figure 6.2.1XRD spectra of ZnO nanoparticles prepared with different volume ratios of water to ethanol (a) 0:1 (b) 0.25:0.75 (c) 0.5: 0.5 (d) 1: 0

The spectra generally show the entire peaks corresponding to various planes of wurtzite phase, indicating a single phase. The crystallite sizes calculated using the Scherrer equation obtained from 20-57 nm. The grain sizes were found to increase with an increase in the ratio of water and corresponding decrease in the ratio of ethanol in solution; indicating a decrease in grain sizes with an increase in pH. Again broadening of peak represents the increase in FWHM and reduction of particle size.

6.3.3. Photoluminescence Analysis

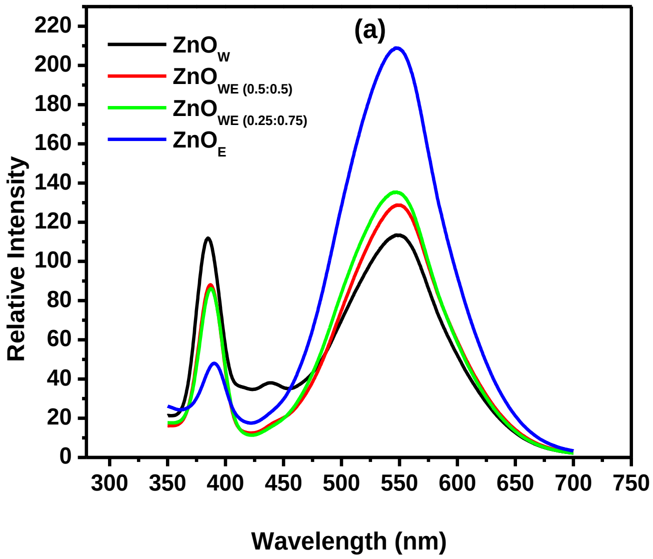

Figure 6.3(a) PL emission spectra of ZnO nanoaparticles prepared at different water: ethanol volume ratios.

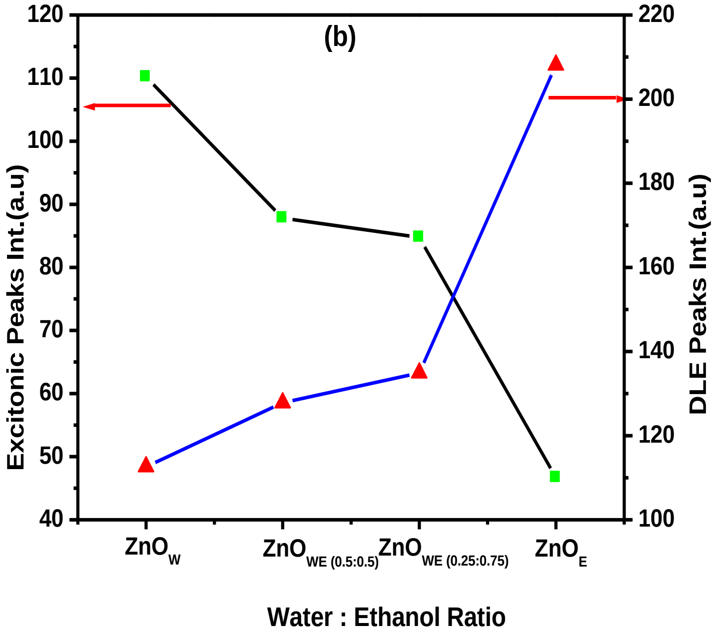

Figure 6.3(b) Comparison of Excitonic and DLE peak intensities of ZnO nanoparticles

Figure 6.3(a) shows the main features of ZnO nanoparticles emissions. The spectra were obtained with excitation wavelength of 281 nm. A sharp ultraviolet (UV) Emission peak centred at about 385 nm and a broad green-yellow emission, centred at about 550 nm, are observed. The UV emission band can be explained by the near band-edge transition of the wide band gap ZnO nanoparticles, the recombination of free excitons through an exciton-exciton collision process [32], whereas the peak at 550 nm is due to the deep-level emission (DLE) related to the defects such as oxygen vacancies and Zn interstitials [33,34].

It has been suggested that the DLE corresponds to the singly ionized oxygen vacancy in ZnO and results from the recombination of a photo-generated hole with the singly ionized charge state of this defect [35]. Figure 6.3(b) displays how DLE peak intensities increase with increasing volume of ethanol in the solvent and corresponding decrease in excitonic peak intensities. The green emission intensity was noted to increase with decreasing nanoparticles diameter for the ZnO nanoparticles. This observation is attributed to the larger surface-to-volume ratio of smaller nanoparticles favouring a higher level of defects density and surface recombination [36].

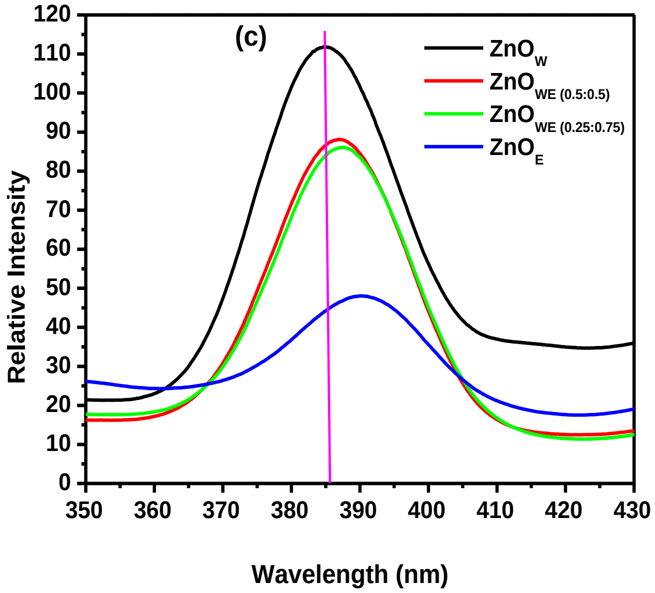

Figure 6.3(c) Curves of relative intensities vs. peak positions for excitonic peaks of ZnO nanoparticles emission spectra prepared at different water: ethanol volume ratios.

The emission spectrum of ZnO nanoparticles prepared in water has excitonic peak at 385 nm, slightly blue shifted compared to the ZnO$_E$ nanoparticles (prepared in ethanol) at 392 nm as shown in Figure 6.3(c). The blue shift is due to the particles nanosize regime exhibiting quantum confinement effect. It is shown that quantum size confinement can significantly enhance the exciton binding energy [38].

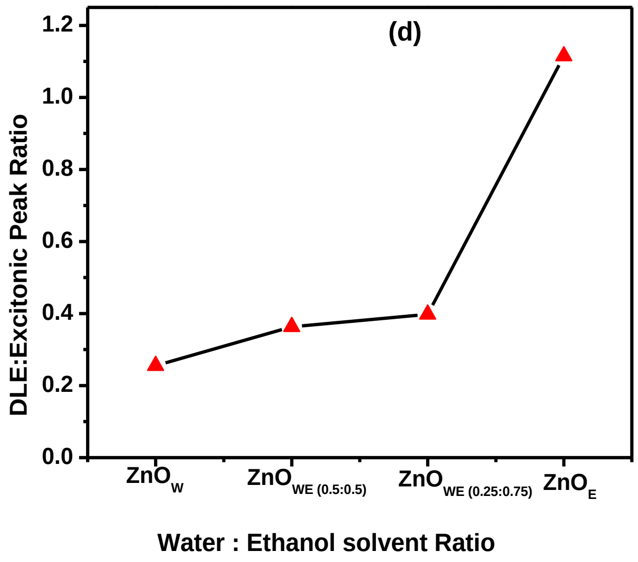

Figure 6.3(d) DLE: Excitonic peak intensities ratio for different solvent ratios.

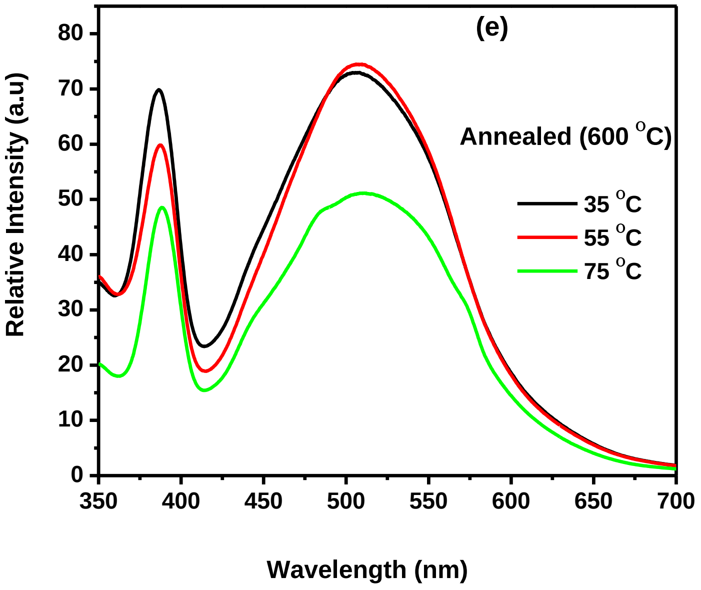

Figure 6.3(e) PL curve of annealed ZnO nanoparticles.

Figure 6.3(d) shows an increase in DLE to UV emission intensity ratio with corresponding increase in volume of ethanol solvent. ZnO_W nanoparticles, with the lowest peak intensity ratio, have better optical properties due to higher crystal quality and low oxygen vacancies and zinc interstitial defects [37]. This is supported by the increased intensity of excitonic peaks for ZnO_W nanoparticles or continuous decrease of the DLE intensity with increasing volume ratios of ethanol solvent as shown in Figure 6.6(a). XRD results (Figure 6.3b) also show that we have the highest peak intensity for ZnO_W.

The strong UV emission, Fig. 6.3(e), and a relatively weak broad deep level visible emission from annealed ZnO nanoparticles confirm that the samples possess good optical properties with less structural defects and impurities. They show a strong and dominant UV emission indicative of good crystal quality, better surface-to volume ratio and oriented ZnO nanoparticles. The nanoparticles can be used for heterojunction formation and attracts broader attention in light emitting diodes (LEDs) and other nanodevice applications.

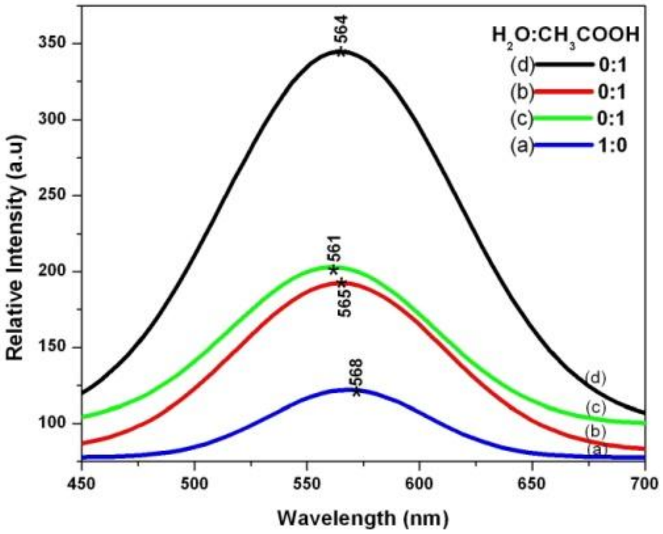

Figure 6.3.1 PL spectra of ZnO nanoparticles prepared with varying ratios of water to ethanol (a) 1 0 (b) – (d) 0: 1.

Figure 6.3.1 is the PL spectra for ZnO nanoparticles synthesized at room temperature. The PL measurements were recorded with the excitation wavelength set at 364 nm. The PL intensity and wavelength of the maximum intensity were influenced by the molar ratio of the solvents. The maximum intensity peak shifts from 568 to 564 nm as molar ratios of water to ethanol changes from 1: 0 to 0: 1 respectively. The measurement insinuates changes in defects density and the ZnO particle sizes caused by changes in crystal field effect.

6.3.4 Optical properties

The effect of different volume ratios of water: ethanol solvents on the optical properties such as reflectance and band gap of ZnO nanoparticles were investigated. The reflectance of ZnO nanoparticles was measured in the wavelength range from 200 to 800 nm.

Figure 6.4(a) depicts the UV-vis reflectance spectra for the ZnO$_W$, ZnO$_{WE}$ and the ZnO$_E$ samples. All the samples showed good reflectance higher than 75% in the visible region. Clearly, the absorption edge is seen to shift to the higher wavelengths with increasing volume of ethanol in the solvent, indicating changes in particle sizes

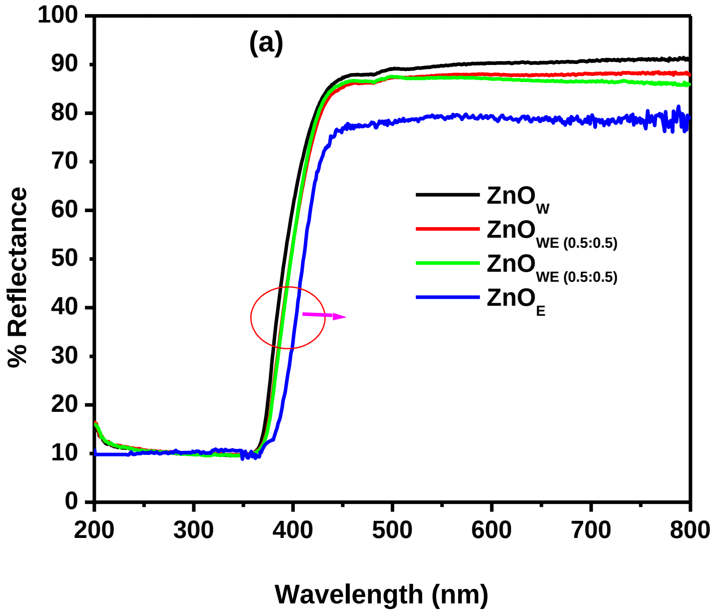

Figure 6.4 (a) Reflectance curve for ZnO$_W$, ZnO$_{WE\ (0.5:0.5)}$, ZnO$_{WE\ (0.25:0.75)}$), and ZnO$_E$ nanoparticles prepared in water, water-ethanol mixtures and ethanol solvents media respectively.

The ZnO$_E$ sample showed the least absorbance between 300 and 400 nm. The % absorbance increases with increasing volume ratios of ethanol in the solvent medium. The decrease in absorbance could be attributed to the larger particle size of ZnO nanoparticles which in turn increases its Rayleigh scattering [39].

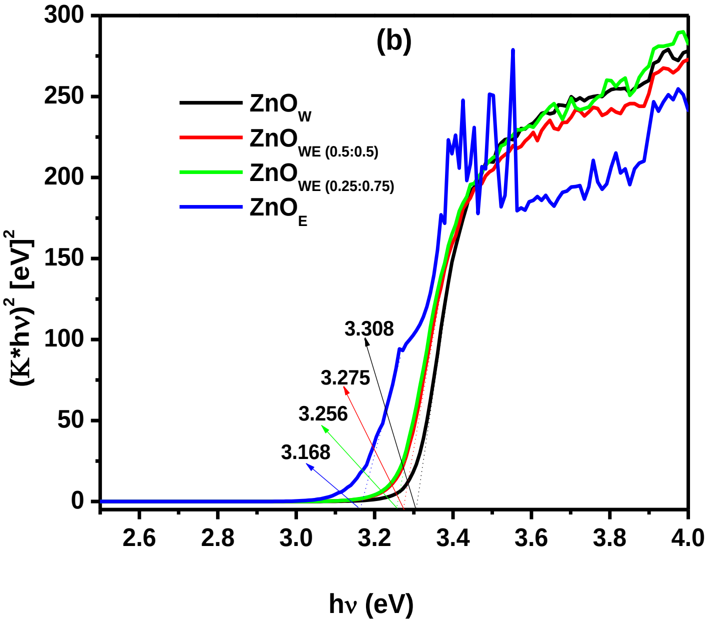

Figure 6.4(b) direct band gaps for ZnO$_W$, ZnO$_{WE (0.5:0.5)}$, ZnO$_{WE (0.25:0.75)}$, and ZnO$_E$ nanoparticles.

Figure 6.4(b) shows the optical band gap, E$_g$, of the ZnO nanoparticles as determined by extrapolation of the linear portion of $(Kh\nu)^2$ versus $h\nu$ plots using the following equation [40]:

$$(Kh\nu)^2 = A(h\nu - Eg)^2 \qquad (5)$$

Where ***K*** is reflectance transformed according to Kubelka-Munk remission function [41],

$$K = \frac{(1-R)^2}{2R} \qquad (6)$$

$h\nu$ is the photon energy, Eg the optical band-gap energy between the valence band and the conduction band at n = 2 for direct transitions and A is a constant, depending on the electron–hole mobility, having a value between 10^5 and 10^6 cm^{-1} and R is reflectance (%).

The extrapolation of the linear portion of the graph to $(Kh\nu)^2 = 0$, axis provides a convenient experimental benchmark for optical band gap. The band gap is found to be 3.168eV, 3.256eV, 3.275eV and 3.308eV with corresponding increase in volume ratio of ethanol. The values lie slightly below the band gap wavelength of 375 nm (Eg = 3.3 eV) of bulk ZnO [42]

The band gap is observed to decrease with an increase in ethanol composition in the solvent, implying that the optical properties of these materials are slightly affected by the synthesis medium. The decrease in the optical band gap with increase in volume ratios of ethanol is due to the variation in lattice defects and stress [43]. The compressed lattice is expected to provide a wide band gap because of the increased repulsion between the oxygen 2p and the zinc 4s bands. Lattice parameter a/b was observed to be smallest in the case of ZnO_W and increased with increasing volume ratio of ethanol unlike lattice parameter c from the XRD results as shown in Table 6.1.

Because of the strong quantum size effect on the absorption peak for the particles prepared in water solvent, the average particle diameter of the ZnO nanoparticles was also determined using the following equation based on the effective mass model (Kumbhakar et al. 2008):

$$d = 2\,x\,\frac{-0.3049+\sqrt{-26.23012+\frac{10240.72}{\lambda_p}}}{-6.3829+\frac{2483.2}{\lambda_p}} \tag{7}$$

Where λ_p is the optical band gap wavelength, which ranged between 385 nm to 392 nm for the samples, prepared in water and ethanol respectively. In this study, the average crystallite diameter thus calculated for ZnO_W was 9.0 nm which closely agrees with 10 nm calculated using Debye-Scherrer's equation providing confirmation of sizes as given by XRD results.

The optical properties of ZnO nanoparticles prepared at room temperature were also investigated. In this investigation the absorption of the ZnO was obtained using the UV-Visible spectra. In general, absorption spectra probe the crystallite internal molecular orbital and provide information concerning size and particle composition [12]. Figures 6.4.1(a) and (b) show the optical absorption spectra of ZnO prepared with varying ratios of water and ethanol.

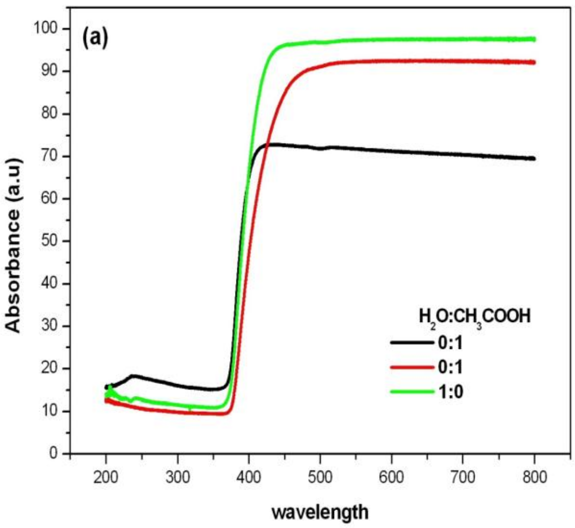

Figure 6.4.1(a) UV-Vis absorbance spectra of ZnO nanoparticle prepared using different volume ratios of water and ethanol.

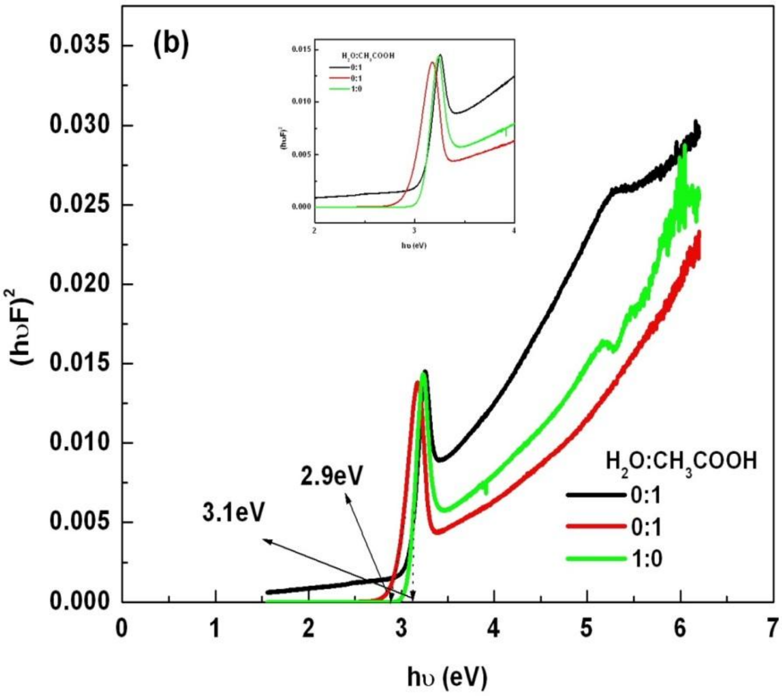

Figure 6.4.1(b) band gap energy spectra of ZnO nanoparticles prepared using different volume ratios of water and ethanol.

The UV-Vis absorbance spectra measurements depict a shift in absorption edge confirming the changes in particle sizes. The band gap energy of ZnO nanostructures prepared with varying ratios of water and ethanol was found to vary between 2.9 to 3.1 eV as depicted in figure 6.9(b). The estimated bandgap energy is lower than that of bulk ZnO (3.37 eV). This band gap reduction may be due to surface defects density of the synthesized ZnO nanostructures [44]. This is confirmed by the shift in absorption edge as shown in Figure 6.9(a).

Conclusion

The work in the first experiment shows that ZnO nanoparticles of high quality can be formed at relatively low temperatures (35 ºC) by sol-gel method by varying water to ethanol solvent ratios. It was found that the crystallinity, surface morphology and optical properties of ZnO nanoparticles depend strongly on the solvent medium. The X-ray diffraction results confirmed the synthesis process efficiency, showing only the hexagonal phase pattern, and the nanometric character of the crystallites produced. Reaction in ethanol results in the formation of rods and spheres which are of smaller sizes. Water as a solvent forms highly crystalline ZnO nanoparticles which are star shaped. The maximum deep level emission was observed for as synthesised ZnO_E nanoparticles and this was consistent with least % reflectance as seen on reflectance curve. Strong UV emission peak was observed for annealed ZnO_E, and decreased with reducing volume of ethanol in solvent in each case.

Similarly, in the second experiment, synthesis of ZnO nanoparticles with varying volume ratios of water and ethanol was reported, using the sol-gel method. PL emission spectra measured under 364 nm UV light excitations, showed different peaks with respect to the solvents ratios used and it has been observed covering the whole 400-700 nm visible region of the electromagnetic spectrum. The nanostructures of the prepared ZnO nanoparticles have been confirmed using XRD, UV-Vis absorption and SEM micrograph analysis. The density of surface states in the nanocrystals would increase with a decrease in the size of crystallites of the prepared nanocrystals, due to the increased surface-to-volume ratio having smaller crystallites. This would reduce the probability of excitonic emission via non-radiative surface recombination.

References

[1] Ozgur U, Alivov Y I, Liu C, Teke A, Reshchikov MA , Dogan S et al. 2005 *J Appl Phys*. 98: 041301-103.

[2] Klingshirn C 2007 *Phys Status Solidi B*. 244: 3027–307.

[3] Daun X, Huang Y, Cui Y, Wang J.F , Lieber C.M 2001 *Nature* 409 66.

[4] Kumar V, Singh R.G, Purohit L.P and Mehra R.M 2011 *J. Mat. Sci. Technol.* 27 481.

[5] Becker C, Ruske F, Sontheimer T, Gorka B, Bloeck U, Gall S and Rech B. 2009 *J. Appl. Phys.* 106 084506.

[6] Verbakel F , Meskers C.J , Rene A.J 2007 *J. Appl. Phys.* 102 083701.

[7] Cui Y, Wei Q, Park H , Lieber C.M 2001 *Science* 293 1289.

[8] Al-Hilli S.M, Al-Mofarji R.T, Klason P, Willander M, Gutman N, Saar A 2008 *J. Appl. Phys.* 103 014302.

[9] Mc Cluskey M.D , Jokela S.J 2009 *J. Appl. Phys.* 106 071101.

[10] Law M, Greene L.E, Johnson J.C, Saykally R , Yang P.D 2005 *Nat. Mater.* 4 455–459.

[11] Singh N, Mehra R..M, Kapoor A , Soga 2012 T *J. Renew. Sust. Energ.* 4 013110.

[12] Kind H, Yan H, Law M, Messer B , Yang P 2002 *Adv. Mater.* 14 158.

[13] Gong Y, Andelman T, Neumark G, O'Brien S , Kuskovsky 2007 *Nanoscale Res. Lett.* 2297.

[14] Vinod Kumar, Singh F, Ntwaeaborwa O.M , Swart H.C 2013 *Appl. Surf. Sci.* 279 472.

[15] Ali A.G, Dejene F.B , Swart H.C 2012 *Cent. Eur. J. Phys.* 10 478-484.

[16] Song R, Liu Y , He L 2008 *Solid State Sci.* 10 1563.

[17] Elen K, Vanden H.R, Hardy A, Van Bael M.K, D’Haen J, Peerters R, Franco D, Mullens J 2009 *Nanotechnology* 20 055608.

[18] Kumar V, Swart H.C, Ntwaeaborwa O.M, Kroon R.E, Terblans J.J, Shaat S.K.K, Yousif A, Duvenhage M.M 2013 *Matt. Lett*. 101 57-60.

[19] Koch U, Fojtik A, Weller H , Henglein A 1985 *Chem Phys. Lett.* 122 507.

[20] Cho S, Jung S. H, Lee K. H 2008 *Journal of Physical Chemistry C*, 112, 12769–12776

[21] Baruah S, Dutta *Sci Technol Adv Mater*,10013001–013017.

[22] Zhao Z.G, Liu Z.F , Miyauchi M 2010 46 3321–3323.

[23] Zhu Y, Zhou Y. 2008 *ApplPhys A* 92 275–8.

[24] Musi S, Dragcevi D, Maljkovi M , Popovic S 2002 *Mater. Chem. Phys.*77 521

[25] Li D , Haneda H 2003 *Chemosphere* 51 (2) 129

[26] Gupta Y , Mansingh A 1996 *J.Appl. Phys.* 80 1063.

[27] Wehner PS, Mercer PN , Apai G 1983 *J Catal* 84 244–247.

[28] Vinay Komari, Vinod Kumar, Malik B.P, Mehra R.M , Mohan D 2012 *Opt. Commun*. 285 2182

[29] Lupan O,Pauporte T, Chow L, Viana B, Pelle F, Ono L.K, Cuenya B. R , Heinrich H 2010 Appl. Surf. Sci, 256 1895

[30] Mathew J.P, Varghese G, Jacob Mathew 2012 *Chin. Phys. B* 21 (7) 078104

[31] Ghosh R, Basak D , Fujihara S 2004 *J. Appl. Phys.* 96 2689.

[32] KongY.C, Yu D.P, Zhang B, Fang W, Feng S.Q 2001 Appl. Phys. Lett. 78 407–409.

[33] Lin C.C, Liu K.H , Chen S.Y 2004 J. Cryst. Growth 269 425–431.

[34] Xu L.F, Guo Y, Liao Q, Zhang J.P , Xu L.S 2005 J. Phys. Chem. B 109 13519–13522.

[35] Vanheusden K, Warren W.L, Seager C.H, Tallant D.R, Voigt J.A , Gnade B.E 1996 *J. Appl. Phys.*797983–7990.

[36] Shalish I, Temkin H , Narayanamurti V 2004 *Phys. Rev. B.* 69 245401.

[37] Stikant V , Clarke D.R 1998 on the optical band gap of zinc oxide, *J.Appl. Phys.* 83 5447– 5451.

[38] Gu Y, Kuskovsky I. L, Yin M, O’Brien S , Neumark G.G 2004 *Appl. Phys. Lett.* 85 3833.

[39] Bohren C.F , Huffman D.R 1983 John Wiley & Sons Inc.

[40] J. Tauc, R. Grigorovichi, A. Vancu 1966 Phys. Status Solidi 15 627.

[41] Duran P, Capel F, Tartaj J , Moure C 2002 *Adv. Mater*. 14 137.

[42] Sakohara S, Ishida M , Anderson M.A 1998 *J. Am. Chem. B* 102 10169 112.

[43] Lin Y.C, Wang B.L, Yen W.T, Ha C.T , Peng C 2010 *Thin Solid Films* 518 4928.

[44] Lee J , Yoon 2009 *J. Phys. Chem. C*. 113 11952-11958.

Chapter 7

Effect of annealing on properties of undoped and Ce, Dy, Eu, Ni-doped ZnO

7.1. Introduction

In the last decade, ZnO has received much attention in view of optoelectronic device applications in the ultraviolet and the visible ranges due to its prominent properties, such as wide band gap (3.37 eV) and high exciton binding energy (60 meV) [1–3]. ZnO is also used in polycrystalline form for facial powder, piezoelectric devices, varistors, phosphors, and transparent conducting oxide films [3]. Besides the UV light-emitting properties, visible luminescence in a range of 400—700 nm for ZnO, was also studied widely because of the potential application in low-voltage field emissive display [4]. On the other hand, the intrinsic properties of ZnO have also been improved by controlling their preparation conditions [5–7]. Doping with selective elements offers an effective method to enhance and control the electrical and optical properties of ZnO nanostructures, which is crucial for its practical application. It is also suggested that annealing at temperatures between 500 ℃ and 700 ℃ leads to an improvement in the crystalline quality (due to the higher UV/DLE intensity ratio compared to the as grown sample). It is expected that at these temperatures, the energy supplied by annealing is sufficient to remove any surface adsorbed impurities and so it becomes energetically favorable for atoms to move into proper sites, leading to an improvement in the crystal quality [8]. In this report the effect of the annealing temperature on the particle size, morphology and photo-luminescence (PL) properties of the synthesized undoped and Ce, Dy, Eu, Ni-doped ZnO nanoparticles were investigated systematically.

7.2. Experimental procedure

Zinc acetate reacted with sodium hydroxide in a molar ratio of 0.02mol to 0.08mol where the mixture of water and ethanol were used as solvent. For the production of pure ZnO nanostructures solution of NaOH was titrated against zinc acetate dehydrate slowly and stirred vigorously for 2 hours, and then kept in a cabinet for some hours to form gel-like solution. This was rinsed using heptane and ethanol mixture, filtered and dried in oven for 1 hour. The dried sample was separated into two portions. The first portion was left to dry further at room temperature and the second portion annealed for 1 hour at 600 ℃ in a furnace (air atmosphere). For the production of doped ZnO nanoparticles, it was performed by adding acetates of Ce, Eu, Dy and Ni to Zinc acetate dehydrate. The mixture so formed was treated through the same procedure for pure ZnO to obtain both the annealed and as prepared samples of the nanoparticles. The molar ratio of dopants to zinc was kept constant at 2 %.The structure of ZnO nanoparticles was characterized by XRD on Bruker D8 X-ray diffractometer using Cu Kα radiation (λ=1.5406 Å) in the 2θ range from 20° to 80°.The surface morphology was studied with a SEM using a Shimadzu model SSX-550 superscan Scanning Electron Microscope. PL measurement was performed on a Cary Eclipse fluorescence spectrophotometer; model LS-55 with a built-in 150W xenon flash lamp as the excitation source and a grating to select a suitable excitation wavelength.

7.3 Results and discussion

7.3.1 SEM analysis

SEM micrographs for annealed and variously doped ZnO nanoparticles are shown in the Figure 7.1. Clearly the powders are in the form of agglomerates with non-uniform shapes and sizes caused by the difference in type of dopants. The SEM observation revealed nanorods and nanoparticles of ZnO depending on the dopant used. For calcinations, the particles showed increment in size, because at higher calcinations temperature the particles agglomerate to produce larger particles in size. It was also observed that the sizes of ZnO nanoparticles became bigger with annealing. In Figure 7.1 (a), Ce-doped ZnO shows relatively larger nanorods

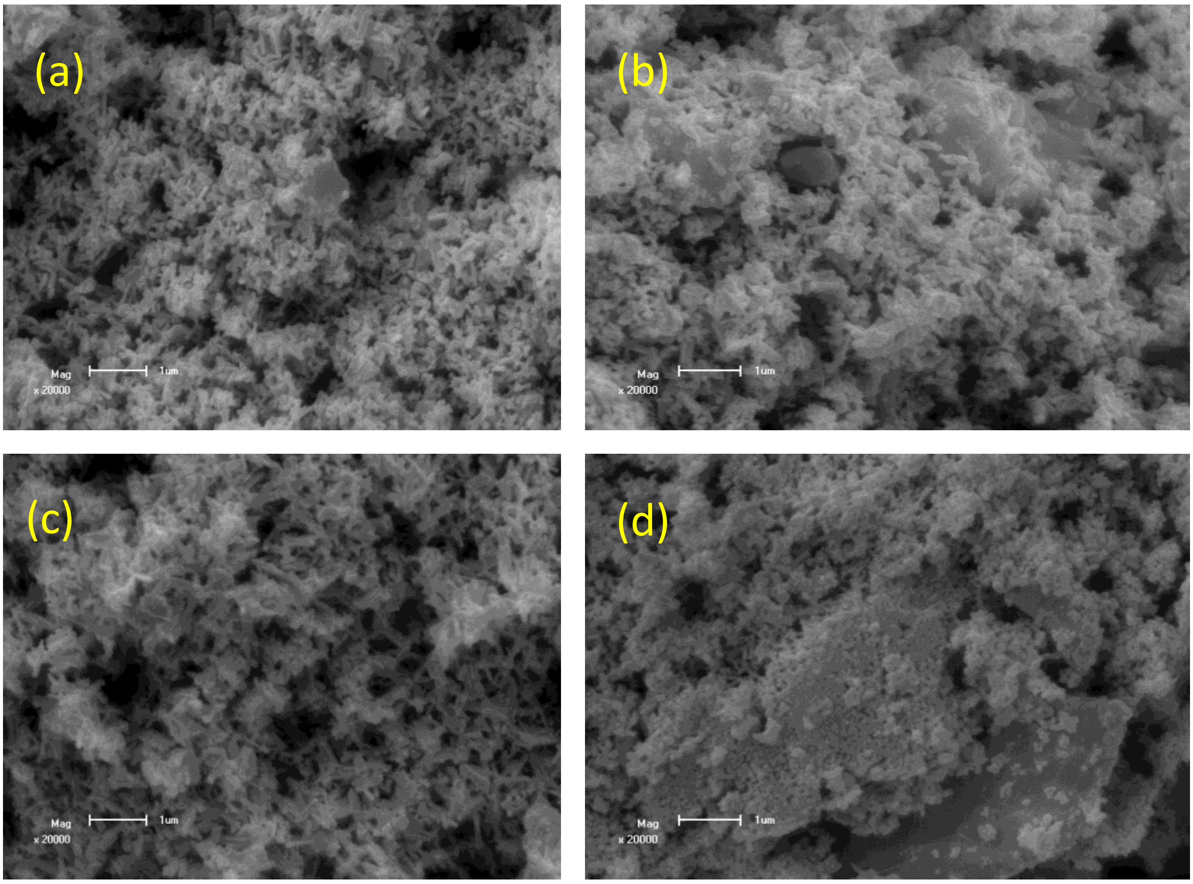

Figure 7.1 SEM images of annealed (a) Ce-doped ZnO (b) Eu-doped ZnO (c) Dy-doped ZnO (d) Ni-Doped ZnO nanostructures.

7.3.2 XRD Analysis

The information about the crystal structure and the shape of ZnO nanostructures were obtained from XRD measurements. Figures 7.2(a) and (b) show that the diverse morphologies observed by SEM and the presence of the doping species do not seem to have an influence on the crystalline phase of the different samples. As revealed by XRD analysis, all ZnO nanostructures, either undoped or doped, show the typical hexagonal wurtzite structure (with respect to the standard card-JCPDS No. 36-1451), and the sharp diffraction peaks indicate the formation of highly crystalline nanostructures. It was found that with annealing the crystallinity of the samples improved and particle sizes increase as shown by the increased intensity of peaks and narrowing of peak widths, respectively according to Figure 7.2(a), while decreased peak intensity and broadening of peak width was observed for unannealed samples as shown in Figure 7.2(b). The crystallite size of as-prepared doped ZnO nanoparticles calculated using the Debye Scherer formula are in the range of 31.3 – 38.0 nm, while that of the annealed ZnO nanoparticles are in the range 31.4 - 39.1 nm. There is no substantial increase in grain size after annealing for 1 hour at 600 °C. Apparently, the annealing time is too short to cause an appreciable increase in the grain size. The improvement of crystallinity after annealing may be due to defect healing and removal of adsorbed impurities as is stated earlier. This proves that the temperature has a slight impact on the crystalline size of ZnO nanoparticles as increase in annealing temperature enhances the kinetic energy of the reaction system, and subsequently increases the number of particle collusions. The increase in particle collusion decreases time to reach a stable size. According to aggregation theory time to reach a stable size is inversely proportional to particle size [9]. Therefore the particle size increases with annealing temperature.

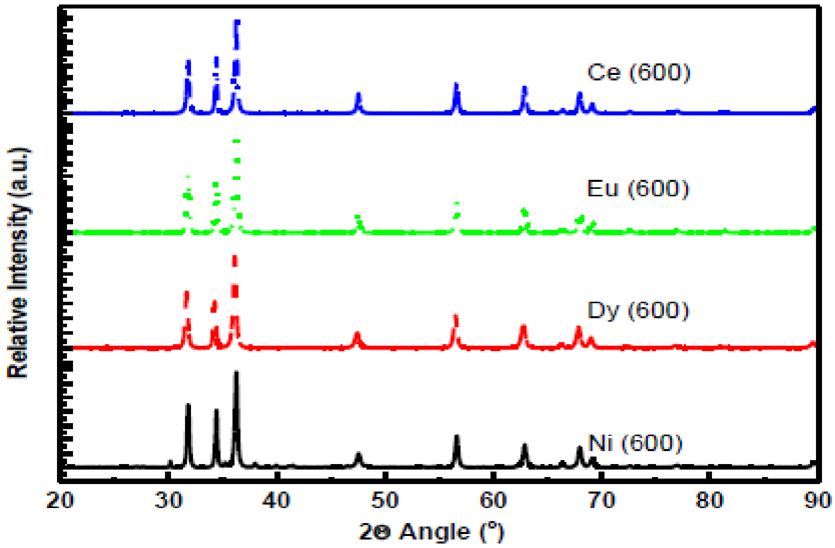

Figure 7.2 (a) XRD spectra of annealed doped ZnO nanoparticles

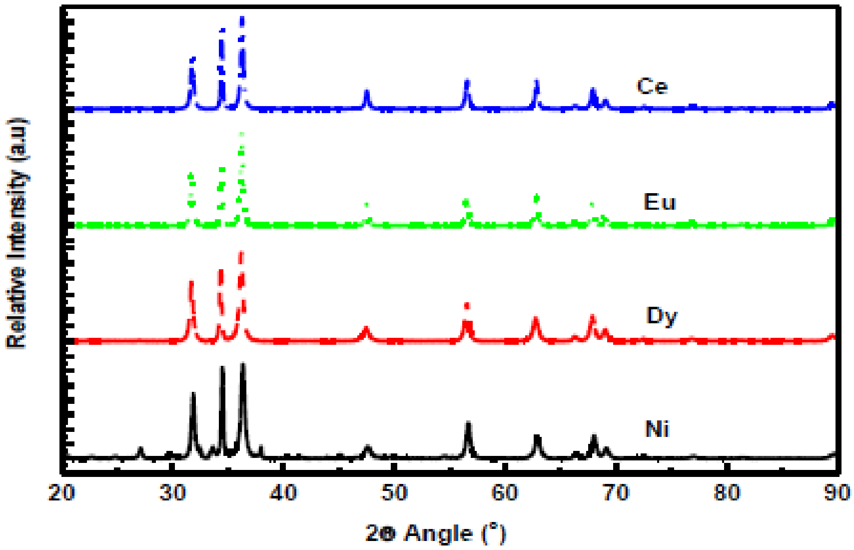

Figure 7.2 (b) XRD spectra of unannealed doped ZnO nanoparticles

7.3.3 Photoluminescence

Figure 7.3 shows the PL measurements recorded with excitation wavelength set at 364 nm. The undoped ZnO sample exhibits a weaker emission band at 380 nm and a broad intense band at around 560 nm in the UV and visible region, respectively. The near-band-edge (NBE) emission in the UV region is attributed to the recombination of free excitons, while the broad green emission is believed to be related to deep levels caused by intrinsic defects such as oxygen vacancies, Zn interstitials, or their complexes [10, 11]. The intrinsic luminescence spectrum of ZnO may vary slightly from sample to sample depending on the syntheses and processing conditions, but it always occurs in the green region of the spectrum. Emission of Eu-doped ZnO demonstrates a broad emission band at 554 nm in the visible range due Eu^{2+} as a result of the *f*-*d* transition [12]. A weaker emission appearing at ~618 nm is ascribed to the Eu^{3+} emission. The PL emission of Ce^{3+}-doped ZnO depicts broad emissions in the visible region. Two luminescence bands contribute to this two broad band with the maximum at 504 and 538 nm. It is well known that the emission from Ce^{3+} is either in the UV or visible region, consisting typically of two main luminescent centres [13] which corresponds to the transitions from the lowest ^{5}d1 crystal field component ($^2D_{3/2}$) to the two components ($^2F_{5/2}$ and $^2F_{7/2}$) of the 4f ground state. The PL emission spectra from ZnO:Ce^{3+} is very similar to that of ZnO but with slight blue shift. Evidently, the positions and intensities of the PL peaks were both affected by annealing temperature as the intensity of emission peaks of the undoped and doped-ZnO nanoparticles increase with annealing temperature. This shift of band-gap energy was believed to originate from the change of tensile stress because of lattice distortion. Similarly, the visible luminescence of ZnO nanoparticles increases with annealing. No emission bands were observed for Dy and Ni-doped ZnO samples.

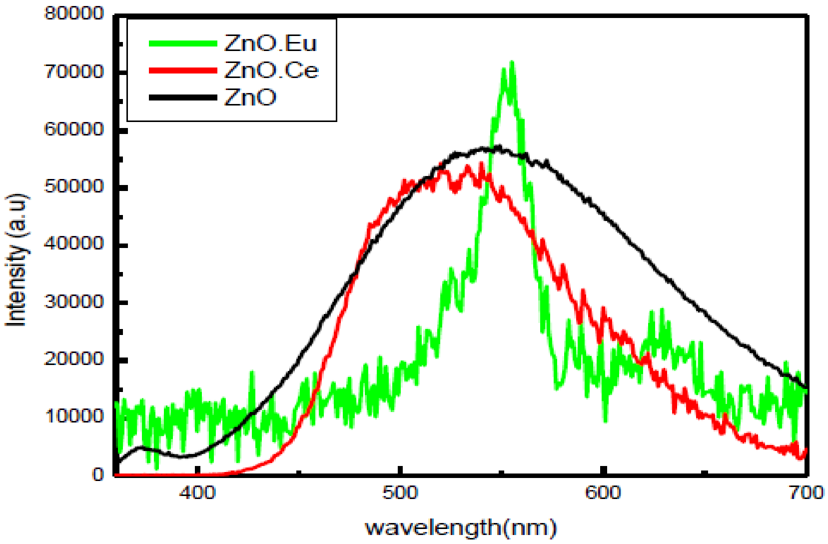

Figure 7.3 PL of undoped ZnO, Ce and Eu-doped ZnO nanoparticles

7.3.4 Optical properties

The absorption of the ZnO was obtained using the UV-Visible spectra. In general, absorption spectra probe the crystallite internal molecular orbital and provide information concerning size and particle composition [9]. Figure 7.4(a) shows the optical reflectance spectra of doped ZnO nanostructures. The UV measurements depict a slight shift in absorption edge confirming the changes in particle sizes. The energy band gap of these materials was estimated using the Kubelka-Munk function emission function [10] for direct transitions. The band gap energy of the ZnO nanostructures prepared with different types of dopant was found to vary between 2.9 and 3.1 eV as shown in Figure 7.4(b). The estimated band gap energy is lower than that of bulk ZnO (3.37 eV). This band gap reduction may be due to surface defects density of the synthesised undoped and doped ZnO nanostructures

[14]. The absorption in the visible region changed with the changes in types of dopant. Ni-doped ZnO was seen to absorb the largest percentage of excitation energy, while Eu-doped ZnO absorbs the least.

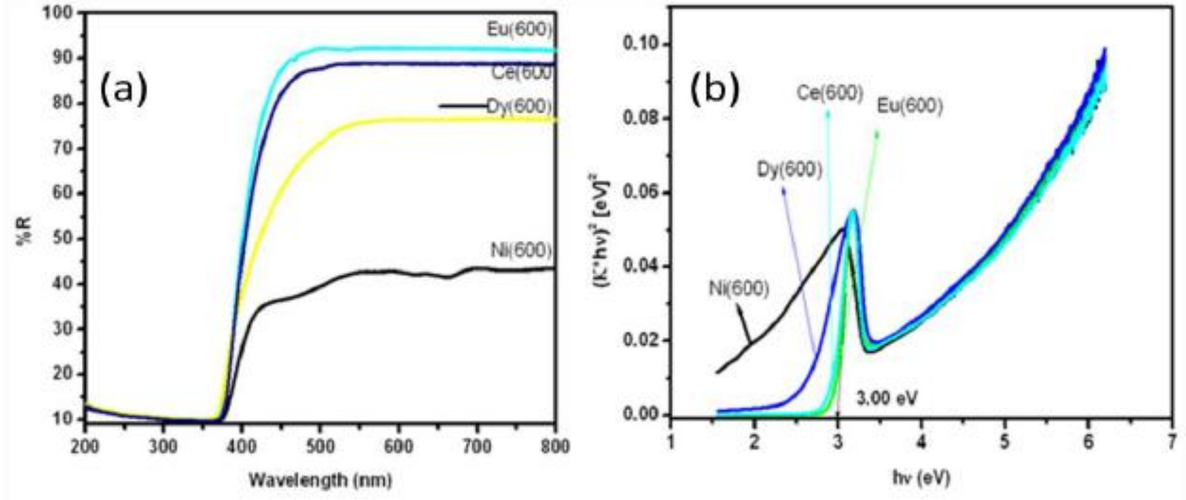

Figure 7.4 (a) UV-Vis reflectance and (b) band gap energy spectra of annealed Ce, Dy, Eu and Ni-doped ZnO nanoparticles.

Conclusion

In summary, the presented data suggest optical-structural correlations in nanosized undoped and doped ZnO materials in terms of crystallinity, defects, and quantum confinement. These properties were revealed by the XRD, SEM, UV-Vis and PL measurements. The incorporation of dopants can influence the morphology of ZnO nanostructures due to defect formation and, consequently, the intensity of the light emission. The effect of post-growth annealing on the structural properties of the nanostructures was determined to lead to an improvement in the crystalline quality. The strong UV and weak green bands emission imply a good optical quality. These results show a great promise for the application of annealed and doped ZnO nanoparticles with low expense and good quantities of electronic and optical properties.

References

[1] Liu Y, Yang J.H, Guan Q.F, Yang L.L, Zhang Y.J, Wang Y.X, Feng B, Cao J, Liu X.Y, Yang Y.T, Wei M.B, 2009 J. Alloys Compound, 486 835.

[2] Wang D.Y, Zhou J, Liu .G.Z, 2009 J. Alloys Compd., 481 802.

[3] Reynolds D.C, Look D.C, Jogai B , Morkoç H, 1997 Solid State Commun. 101 643.

[4] Leverenz V.W, An Introduction to Luminescence of Solids, Dover, New York, 1968.

[5] Xiong G, Wilkinson J, Mischuck B, Tuzemen S, Ucer K.B , Williams R.T , 202 Appl. Phys. Lett. 80 1195.

[6] Ma Y, Du G.T, Yang . S.R, Li Z.T, Zhao J, Yang X.T, Yang T.P, Zhang Y.T and Liu D, 2004 J. Appl. Phys. 95 6268.

[7] Oh M.S, Kim S.H and Seong T.Y, 2005 Appl. Phys. Lett. 87 103.

[8] Tan S.T, Sun X.W, Zhang X.H, Chua S.J, Chen B.J, Teo C.C, 2006 J. Appl. Phys. 100 033502.

[9] Chandrasekhar S,1943 Rev. Mod. Phys. 15 1.

[10] Ahn C.H, Kim Y.Y, Kim D.C, Mohanta S, K, Cho H K 2009 J. Appl. Phys. 105 013502.

[11] J. Lee, A.J. Easteal, U. Pal, D. Bhattacharyy, 2009 Current Applied Physics, 9 792–796.

[12] Bhargava R N, Chhabra V, Som T, Ekimov A, Taskar, N. Phys. 2002 Status Solidi B 229897.

[13] Koao L F, Swart H.C, Coetsee E, Biggs M.M, Dejene F.B, 2009 Physica B, 404 4499 –4503.

[14] Wang Z, Zhang H, Zhang L, Yuan J, Wang C, 2003 Nanotechnology 14 11.

Chapter 8

Thesis summary and conclusion

In this thesis, the growth of ZnO nanostructures using a cost-effective, simple and environmentally friendly synthesis technique (sol-gel) was discussed. The salient results are summarized in this chapter, followed by suggestions for future work

Nanoparticles have been successfully synthesized by sol-gel method. The influence of the nanoparticles growth parameters on the morphology, optical and electrical properties of the structures was also systematically studied. These include the growth temperature, the volume ratios of water to ethanol solvents and dopants. By varying or changing these parameters, different architectures of nanostructures, including spherical nanoparticles, nanorods, and nanoflowers were achieved. The effect of post-growth annealing on the optical quality of the nanostructures was also carefully examined.

All these samples were characterized using different techniques. The morphology of the nanoparticles was observed by a Shimadzu Superscan SSX-550 system scanning electron microscope (SEM) operated at 20kV equipped with energy dispersive X-ray spectroscopy (EDS). Optical absorption was performed on a Perkin Elmer Lamb 950 UV-Visible Spectrophotometer (UV). The X-ray Diffraction patterns were recorded to characterize the phase crystal structure of the nanoparticles using a D8 Bruker Advanced AXS GmbH X-ray diffractometer (XRD), room temperature. Photoluminescence (PL) of the samples was measured using the Cary Eclipse Spectrophotometer. A Simultaneous Differential Scanning Calorimetry/Thermogravimetric Analysis (DSC/TGA) system of STA 6000 (PerkinElmer) was used for thermo gravimetric analysis while the FTIR was measured using FTIR Spectrometer (PerkinElmer Spectrum 100)

In the preparation of ZnO nanoparticles, by varying volume ratios of water and ethanol the PL emission spectra were measured under 364 nm UV light excitations. Different peaks with respect to the solvents ratios used were observed covering the whole 400-700 nm visible region of the electromagnetic spectrum. The density of surface states in the nanoparticles increased with a decrease in the size of crystallites, due to the increased surface-to-volume ratio having smaller crystallites. This reduced the probability of excitonic emission via non-radiative surface recombination.

The crystallinity, surface morphology and optical properties of ZnO nanoparticles depended strongly on the solvent medium. Reaction in ethanol resulted in the formation of rods and spheres which were of smaller sizes. Water as solvent formed highly crystalline ZnO nanoparticles which were star shaped. The ZnO_E nanoparticles (prepared in ethanol) had a regular, polyhedra morphology while the ZnO_W (prepared in water medium) had irregular spherical morphology, mixed with some chunky particles. The maximum deep level emission was observed for as synthesized.

The effect of doping on the quality of the nanoparticles was examined, presented data suggest optical-structural correlations in nanosized undoped and doped ZnO materials in terms of crystallinity, defects, and quantum confinement. The incorporation of dopants can influence the morphology of ZnO nanostructures due to defect formation and, consequently, the intensity of the light emission.

The effect of post-growth annealing on the structural properties of the nanostructures was determined to lead to an improvement in the crystalline quality. Annealing in the temperature of 600 ℃ strongly enhanced the UV emission and suppressed the defect related deep level emission (DLE).The strong UV and weak green bands emission imply a good optical quality. These results show a great promise for the application of annealed nanoparticles with low expense and good quantities of electronic and optical properties.

The synthesis temperature was shown to have a strong influence on luminescence and optical properties of ZnO nanoparticles. As growth temperature increases from 35 °C to 65 °C crystallite grain sizes increase correspondingly. Increased growth temperature significantly quenches the green emission and the peak positions and intensities are both affected by growth temperatures. The optimum temperature to achieve pure and good crystal quality ZnO using this method was from 55 ℃ to 65 ℃ as shown by PL measurement.

Future work

Various other ZnO nanostructures such as nanorods and nano wires can be investigated. Preparation of ZnO sing a CBD method can also be looked at. The investigation might also include ways to control agglomeration of ZnO particles like the use of surfactants and compare effects of the methods used to prepare these particles. In terms of fundamental material properties, more detailed studies of the effects of annealing temperature and ambient on luminescence response, combined with detailed XPS will be invaluable to identify the species and defects responsible for the trends observed and reported in this thesis. Also worth, considering are; synthesis of ZnO nanorods on silicon substrates, precursor concentration and other growth parameters.

List of Tables

List of Figures

Publications

The following papers have been submitted for publication by the authors;

Ungula J and Dejene B.F

1. Effect of annealing on undoped and Ce, Dy, Eu, Ni-doped ZnO properties synthesized by sol-gel method. Proceedings of the SAIP 2013 (South African Institute of Physics) The 58th Annual Conference of the SA Institute of Physics hosted by University of Zululand-Richards Bay Campus. ISBN: 978-0-620-62819-8
2. Comparison of ZnO nanoparticles properties synthesised at room temperature using water and ethanol as solvents. The 5th South African Conference on Photonic Materials (SACPM 2013), May 2013, Kariega Game Reserve, South Africa.
3. Effect of growth temperature on structural and luminescence properties of ZnO nanoparticles by Sol-Gel method, The 59th Annual Conference of the SA Institute of Physics (SAIP 2014) hosted by University of Johannesburg.

Conferences

- **58th Conference of South African Institute of Physics (SAIP 2013),** University of Zululand-Richards Bay Campus,(RSA) 8th-12th July 2011, Comparison of ZnO nanoparticles properties synthesised at room temperature using water and ethanol as solvents.

- **59th Conference of South African Institute of Physics (SAIP 2014),**University of Johannesburg (RSA) 7th-11th July 2014, Effect of growth temperature on structural and luminescence properties of ZnO nanoparticles by Sol-Gel method, Ungula J and Dejene B.F

- **5th South African Conference on Photonic Materials (SACPM 2013),** Kariega Game Reserve, (RSA) 29th Apr.- 3rd May 2013, Comparison of ZnO nanoparticles properties synthesised at room temperature using water and ethanol as solvents. Ungula J and Dejene B.F